Aus dem Institut für Physiologie und Pathophysiologie

Geschäftsführender Direktor: Prof. Dr. Dominik Oliver

des Fachbereichs Medizin der Philipps-Universität Marburg

Analysis of the molecular mechanisms of prestin-mediated cochlear amplification via a cysteine accessibility study

Analyse der molekularen Mechanismen der Prestin-abhängigen cochleären Amplifikation mittels einer Cystein Zugänglichkeitsstudie

Inaugural-Dissertation zur Erlangung des Doktorgrades der Naturwissenschaften

dem Fachbereich Medizin der Philipps-Universität Marburg

vorgelegt von

Julia Hartmann

aus Groß-Umstadt

Marburg, 2021

Angenommen vom Fachbereich Medizin
der Philipps-Universität Marburg
am: 08.03.2021

Gedruckt mit Genehmigung des Fachbereichs

Dekan: Frau Prof. Dr. D. Hilfiker-Kleiner
Referent: Herr Prof. Dr. D. Oliver
1. Korreferent: Herr Prof. Dr. T. Worzfeld

Table of contents

i Figures

ii Tables

iii Abbreviations

ATP	Adenosine triphosphate
CHO	Chinese Hamster Ovary
C_{lin}	linear (passive) membrane capacitance
CLSM	Confocal Laser Scanning Microscopy
C_M	membrane capacitance
cryo-EM	cryogenic Electron Microscopy
DNA	deoxyribonucleic acid
DTT	Dithiothreitol
E. coli	Escherichia coli
H_2O_2	Hydrogen peroxide
HEK	human embryonic kidney
IHC	inner hair cell
MßCD	Methyl-ß-cyclodextrin
mRNA	messenger ribonucleic acid
MTS	Methanethiosulphonate
MTSES	Sodium (2-Sulphonatoethyl)methanethiosulphonate ($C_3H_7O_5S_3$*Na) Synonym: 2-[(Methylsulfonyl)thio]ethanesulphonic Acid Sodium Salt
MTSET	[2-(Trimethylammonium)ethyl]methanethiosulphonate Bromide ($C_3H_{16}BrNO_2S_2$) Synonym: Methanethiosulphonate Ethyltrimethylammonium Bromide
NLC	nonlinear capacitance
NCS2	nucleobase/cation symporter 2
OHC	outer hair cell
PBS	phosphate-buffered saline
PDL	Poly-D-Lysine
PCR	polymerase chain reaction
PSA	Phenolsulphonic acid
Q	charge
Q_{max}	maximum voltage-sensor charge moved through the membrane electric field
SCAM	substituted cysteine accessibility method
SLC	Solute Carrier

SEM	standard error of the mean
STAS	Sulfate Transporter and Anti-Sigma factor antagonist
SulP	Sulfate Permease
TM	transmembrane domains
$V_{1/2}$	voltage at half-maximal charge transfer
V_M	membrane potential
w/	with
w/o	without
WT	wild type
WT_△Cys	wild type with all cysteines mutated to alanines
zf	zebrafish
α	slope factor of the voltage dependence

Amino acids

A	alanine
C	cysteine
E	glutamic acid
F	phenylalanine
G	glycine
H	histidine
I	isoleucine
L	leucine
M	methionine
P	proline
R	arginine
S	serine
T	threonine
V	valine
W	tryptophan

iv Summary

Prestin is the protein being responsible for electromotility in mammals. It is a member of the SLC26 (**S**o**l**ute **C**arrier) family, which function as anion transporters. In contrast to the other members, mammalian prestin does not function as an anion transporter but produces electromotility. Non-mammalian prestin orthologues such as zebrafish prestin are anion-exchangers with a stoichiometry of 1:1, where a chloride anion is transported in exchange for a divalent anion. Based on the bacterial uracil transporter UraA, a structural homology model of prestin with a 7+7 inverted repeat architecture was predicted.

The mechanism of the SLC26-mediated transport is not fully understood. A potential role of this transport mechanism in the electromotile properties of prestin is elusive, but based on the high sequence similarity of transport-capable and electromotile prestin orthologues the idea arose that both are related and electromotility evolved from transport. This is further supported by the finding that the motor protein prestin interacts with and only undergoes conformational rearrangements in the presence of intracellular monovalent anions. Furthermore, it is not completely understood whether electromotile prestin undergoes structural dynamics that are similar to those of transport-capable members of the SLC26 family.

The aim of the present study is to elucidate whether the function of the SCL26 transporters and voltage-driven motors follows common structural principles. To achieve this aim, two members of the SLC26 family were chosen as model systems: the non-mammalian zebrafish prestin and the mammalian rat prestin. The method mainly used in this study is a cysteine accessibility study. It allows insights into structures that should change their accessibility to the aqueous medium according to their movement during a transport cycle.

The membrane-impermeable MTS reagents were either applied from the intracellular or extracellular side. In rat and zebrafish prestin positions were identified which were sensitive to MTS applications and in consequence accessible.

The presumptive anion-binding site and the anion translocation pathway are mainly located in the transmembrane domains 3 and 10. The data here presented are consistent with the structural models derived from experimental structures. Positions within transmembrane domain 10 are mainly accessibly from the intracellular side and positions within transmembrane domain 3 from the extracellular side.

Furthermore, there are central positions in zebrafish prestin, which are accessible from both sides. This indicates an alternating-access transport consistent with elevator movement of the core domain. The lack of extracellular access of the homologous positions

in rat prestin shows that the extracellular-exposed conformation is not obtained in mammalian prestin. This points towards an incomplete transport mechanism performed by mammalian prestin.

The rat prestin mutant V139C is accessible from both sides. This two-sided accessibility suggests an outward movement of the core domain within an incomplete transport transition. This mutant shows that V139 faces the translocation pathway in the inward-open as well as in the occluded conformation and thus stays rigid and does not undergo a conformational rearrangement. An alternating-access transport in elevator mode is characterised by a relatively rigid immobile gate domain, a mobile core domain, which contains the anion-binding site, and a vertical displacement of the bound substrate. The results of the scanning support this mode of transport that was also proposed for a prokaryotic SLC26 family member. While crystal structures record a protein in a certain conformation cysteine labelling provides the opportunity to study the full conformational changes.

The model derived from the scanning results present alternate conformations determined by the extracellular accessibilities of positions of the respective prestin orthologue. To what extent the core domain opens to the extracellular side can be deduced by the positions V139 within transmembrane domain 3 in rat prestin and M400 and S400 within transmembrane domain 10 in zebrafish prestin. There is an obvious difference between the alternate conformation of rat and zebrafish prestin. Zebrafish prestin undergoes a full transport cycle from an inward-open to an outward-open conformation, whereas rat prestin alternates between the inward-open and the intermediate (occluded) conformation. The results of the scanning show that the elevator mode of transport is mainly realised by zebrafish prestin. Rat prestin fails to reach the outward-open conformation, thus it performs an incomplete transport mechanism in an elevator-like manner.

Additionally, rat prestin V139C shows a combination of mechano- and redox-sensitivity. The activity of rat prestin V139C is dependent on the application of fluid-flow. This flow-dependency of activity seems to be correlated with the microenvironment of the mutant - the more inflexible the side chain the more distinct the flow-sensitivity of activity. On the basis of the presented data the applied fluid-flow does not cause membrane tension in V139C. The mechanosensitivity of V139C seems to be provoked by pure shear stress. Furthermore, it is different from the intrinsic tension-sensitivity of prestin wild type. Finally, the phenomenon of the mechano- and redoxsensitivity could not yet be clarified.

v Zusammenfassung

Prestin ist als das Protein identifiziert worden, welches für die Elektromotilität in Säugetieren verantwortlich ist. Es ist ein Mitglied der SLC26 (**S**o**l**ute **C**arrier) Familie, dessen Mitglieder als Anionentransporter fungieren. Im Gegensatz zu den anderen Mitgliedern ist das Säugetier-Prestin kein Anionentransporter und generiert stattdessen Elektromotilität. Nichtsäugetier-Prestin Orthologe wie das Prestin des Zebrabärblings sind Anionenaustauscher mit einer Stöchiometrie von 1:1, wobei ein Chloridanion im Austausch gegen ein zweiwertiges Anion transportiert wird. Basierend auf dem bakteriellen Uracil Transporter UraA wurde ein strukturelles Homologiemodell von Prestin mit einer 7+7 „inverted repeat" Architektur entworfen.

Der Mechanismus des SLC26-vermittelten Transports ist noch nicht vollständig aufgeklärt. Welche Rolle dieser Transportmechanismus für die elektromotilen Eigenschaften von Prestin spielt, ist unklar. Basierend auf der hohen Sequenzhomologie transportfähiger und elektromotiler Prestin Orthologe entstand die Idee, dass beide Mechanismen verwandt sind und Elektromotilität aus einem Transportmechanismus entstanden ist. Dies wird ebenfalls dadurch belegt, dass das Motorprotein Prestin mit intrazellulären monovalenten Anionen interagiert und Konformationsänderungen nur in Anwesenheit dieser Anionen durchführt. Dennoch ist es nicht komplett verstanden, ob elektromotiles Prestin strukturelle Dynamiken durchläuft, welche denen transportfähiger Mitglieder der SLC26 Familie ähneln.

Das Ziel der vorgelegten Studie war es aufzuklären, ob die Funktion der SCL26 Transporter und spannungsgetriebener Motorproteine gemeinsamen strukturellen Prinzipien folgt. Um dies zu erreichen, wurden zwei Mitglieder der SLC26 Familie als Modellsysteme ausgewählt: das Nichtsäugetier-Prestin des Zebrabärblings und das Säugetier-Prestin der Ratte. Die hauptsächlich angewandte Methode in dieser Studie war eine Cystein Zugänglichkeitsstudie. Dadurch können Strukturen identifiziert werden, welche ihre Zugänglichkeit zum wässrigen Medium entsprechend ihrer Bewegung während eines Transportzyklus ändern.

Die membranundurchlässigen MTS Reagenzien wurden entweder von der intrazellulären oder der extrazellulären Seite appliziert. Im Prestin der Ratte und des Zebrabärblings wurden Positionen identifiziert, welche sensitiv auf Applikationen mit MTS reagierten und folglich zugänglich sind.

Die mutmaßliche Anionenbindungsstelle und der Anionentranslokationsweg sind größtenteils in den Transmembrandomänen 3 und 10 lokalisiert. Die hier vorgestellten

Daten stimmen mit den aus experimentellen Strukturen abgeleiteten Strukturmodellen überein. Positionen innerhalb der Transmembrandomäne 10 sind hauptsächlich von der intrazellulären Seite zugänglich und Positionen innerhalb der Transmembrandomäne 3 von der extrazellulären Seite.

Darüber hinaus gibt es zentrale Positionen im Zebrabärblingprestin, die von beiden Seiten zugänglich sind. Dies deutet auf einen alternierenden Zugang während des Transports (‚alternating-access transport') mit einer Aufzugsbewegung (‚elevator movement') der Kerndomäne hin. Das Fehlen des extrazellulären Zugangs der homologen Positionen im Rattenprestin zeigt, dass die extrazellulär exponierte Konformation im Säugetierprestin nicht erreicht wird. Dies spricht für einen unvollständigen Transportmechanismus, welchen das Säugetierprestin durchläuft.

Die Mutante Rattenprestin V139C ist von beiden Membranseiten zugänglich. Diese zweiseitige Zugänglichkeit spricht für eine Bewegung der Kerndomäne nach außen innerhalb eines unvollständigen Transports. Diese Mutante demonstriert, dass V139 sowohl in der nach innen geöffneten als auch der intermediären (‚occluded') Konformation rigide zum Translokationsweg zeigt und keine konformative Umordnung widerfährt.

Ein Transport mit abwechselndem Zugang in einer Elevator Weise ist charakterisiert durch eine relative rigide immobile Tordomäne (‚gate domain'), eine mobile Kerndomäne (‚core domain'), welche die Anionenbindungsstelle beinhaltet, und eine vertikale Verschiebung des gebundenen Substrates. Das Ergebnis des Scannings unterstützt diese Weise des Transportes, welche ebenfalls für ein prokaryotisches SLC26 Familienmitglied vorgeschlagen wurde. Während Kristallstrukturen ein Protein in einer bestimmten Konformation erfassen, bietet die Cysteinmarkierung die Möglichkeit komplette Konformationsänderungen zu studieren.

Das Modell, welches aus den Scanningdaten resultiert, präsentiert alternierende Konformationen, welche durch die extrazelluläre Zugänglichkeit von Positionen des jeweiligen Prestin Orthologs ermittelt wurden. Bis zu welchem Grad sich die Kerndomäne zur extrazellulären Seite öffnet, kann durch die Zugänglichkeit der Positionen V139 innerhalb der Transmembrandomäne 3 des Rattenprestins sowie M400 und S400 innerhalb der Transmembrandomäne 10 des Zebrabärblingprestins hergeleitet werden. Es gibt einen offensichtlichen Unterschied zwischen den alternierenden Konformationen des Prestins der Ratte und des Zebrabärblings. Das Prestin des Zebrabärblings durchläuft einen kompletten Transportzyklus von der nach innen geöffneten bis zur nach außen geöffneten Konformation, wohingegen das Rattenprestin zwischen der innen geöffneten und der

intermediären (‚occluded') Konformation alterniert. Die Scanningergebnisse zeigen, dass der Elevatortransport primär vom Prestinortholog des Zebrabärblings durchgeführt wird. Das Prestin der Ratte nimmt die nach außen geöffnete Konformation nicht ein und führt dementsprechend einen unvollständigen Transportmechanismus in einer Elevator-ähnlichen Weise durch.

Zusätzlich zeigt die Mutante V139C des Rattenprestins eine Kombination aus Mechano- und Redoxsensitivität. Die Aktivität des Rattenprestins V139 ist abhängig von der Applikation eines Fluidstroms. Die Fluss- (‚flow'-) abhängkeit der Aktivität dieser Mutante scheint mit ihrer Mikroumgebung zu korrelieren – je unflexibler die Seitenkette desto ausgeprägter die Fluss-Abhängigkeit der Aktivität. Basierend auf den hier vorgestellten Daten verursacht der applizierte Fluidstrom keine Membranspannung, sondern Scherspannungen in V139C. Darüber hinaus unterscheidet sich diese Sensitivität von der intrinsischen Spannungssensitivität des Prestin Wildtyps. Letztlich konnte das Phänomen der Mechano- und Redoxsensitivität nicht aufgeklärt werden.

1 Introduction

Hearing is an invention of evolution. The sense of sound has evolved gradually and is therefore not found in every animal species. Furthermore, the ear is the vertebrate hearing organ, but it is not the only acoustic sensory organ, e.g. the tympanal organ is the hearing organ of many insects and its hearing membrane is located differently, at the front legs in crickets or at the abdomen in cicadas. This study will focus on two species as representatives of vertebrates, zebrafish (*Danio rerio*) and rat (*Rattus norvegicus*).

Principles of hearing in vertebrates and particularly the two abovementioned representatives will be explained below. While a variety of different hearing organs evolved across invertebrate phyla, the perception and conduction of acoustic signals is always connected to the inner ear in vertebrates. Accordingly, the inner ear is very similar regarding structure and function throughout vertebrates. The range of frequencies, in which perception of sound takes place, is called audible sound and varies substantially between species. A healthy person can detect sound in the frequency range of 16 Hz to 20 kHz. In rats, e.g., the hearing is most sensitive in the range of 200 Hz to 16 kHz and has its upper frequency limit at 90 kHz, which corresponds to ultrasound (Du et al., 2007). In contrast, sound detection in 'lower' vertebrates such as zebrafish is mostly best in the low frequency range. Equipped with air bladder and Weberian apparatus, their range extends up to only 4 kHz (Higgs et al., 2003; Wang et al., 2015).

Besides the anatomical differentiations that underlie the different hearing ranges, the specialisations of the ears of, e.g., mammals and fishes are likewise based on features at the molecular and cellular level, which enable the respective sound sensation. The focus of this study is the molecular mechanism of one unique and pivotal specialisation in mammals, the so-called electromotility of sensory hair cells.

1.1 The ear

The ear is the sensory organ, which receives acoustic stimuli, processes them mechanically, and finally codes them into neuronal signals. In mammalian vertebrates it consists of three parts: the outer, the middle and the inner ear. The equilibrium (vestibular) organ is also part of the inner ear and evolutionarily and functionally closely related to hearing.

On the other hand, bony fishes feature an air bladder, with which they detect sound waves and convey them to the inner ear. Zebrafishes belong to the minnow family of *Cypriniformes*, a member of the superorder of *Ostariophysi*, in which the Weberian apparatus mediates transmissions of sound from the air bladder to the inner ear (Dudel et al., 2001; Grande &

Young, 2004). Furthermore, the inner ear of zebrafishes has specialised hair cells, though there is no differentiation between inner and outer hair cells (Riley et al., 1997).

Rats represent the order of *Rodentia* of the class of *Mammalia.* In mammals, the inner ear developed into the snail-shaped cochlea with the sensory epithelium ('organ of Corti') sitting on top of the elastic basilar membrane and containing two specialised types of sensory hair cells, inner and outer hair cells.

1.2 The principles of hearing

The hearing process is coupled to multiple requirements, e.g. frequency coding and analysis (Dudel et al., 2001). The otolith organ functions as the hearing organ in fish. In contrast, the organ of Corti within the cochlea is the sensing organ for hearing in mammals. The sensory epithelium has evolved from the otolith organ in fish to the basilar papilla in reptiles and birds. The basilar papilla is strongly elongated and rolled up into a spiral in mammalian vertebrates, yielding a structure called cochlea. The human cochlea in its uncoiled form has a length of about 34 mm.

In mammals, an incoming sound wave reaches through the outer ear canal to the eardrum, which in turn starts to vibrate and thereby mobilises the three ossicles (malleus, incus and stapes) of the middle ear (Figure 1.1). The last in the chain transfers the mechanical pressure to the oval window as the entrance to the cochlea. The cochlea is fluid-filled and acoustic vibration spreads along the cochlea as a travelling wave (Robles & Ruggero, 2001; Olson et al., 2012), moving from the oval window up to the apex of the cochlea. In doing so, the wave reaches a place of maximum amplitude on the basilar membrane that is specific for the frequency of the sound (Gundersen et al., 1978) (Figure 1.2). Sound waves with high frequencies lead to maximum vibration near the oval window. With decreasing frequency, the maximum of the displacement occurs at more apical positions along the cochlea. The consequence of this vibration pattern is a mechanical spatial dispersion of sound frequencies. The subsequent assignment to a distinct sensory cell population at each cochlear position and downstream the associated nerve fibre establishes a neuronal tonotopy. Together with the basilar membrane all associated structures experience vibration. This applies in particular to the organ of Corti and the cochlear sensory hair cells.

The hair cells transduce the sound stimulus into neural signals. Mammals possess two different types of those cells, the inner hair cells and the outer hair cells (Figure 1.3). In humans about 3.500 inner hair cells form one row along the cochlea, while about 11.000 outer hair cells are arranged in three rows.

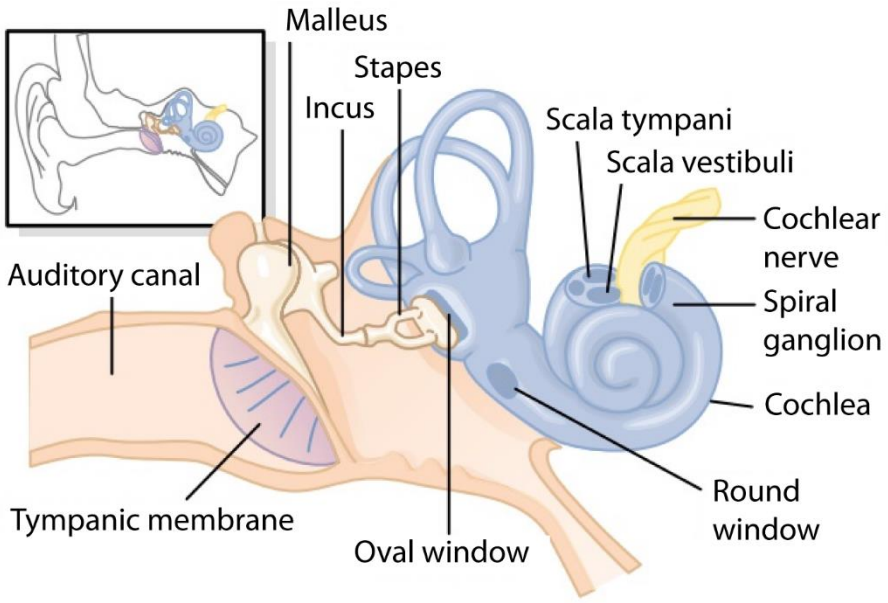

Figure 1.1: Structure of the human ear. The focus is on the middle ear with the three ossicles (malleus, incus and stapes) and the inner ear, which is coloured in blue. The inner ear consists of the cochlea and is connected to the vestibular system with its three semi-circular canals. Image source: Hall, 2010.

The inner hair cells possess a much denser afferent innervation than the outer hair cells. The hair cells transmit all acoustic information to the brain by transducing the vibrations of the basilar membrane into electrical signals. The apical pole of the hair cells contains hair bundles, several rows of stereocilia that are connected via tip links. Mechanical deflection of the hair bundle towards the tallest stereocilium opens mechanosensitive transduction channels, which are nonspecific cation channels (Beurg et al., 2009; Beurg & Fettiplace, 2017). The hair cells are surrounded by the endolymph at the apical end and by the perilymph at the basal end. These two fluids vary in their composition. The endolymph is rich in K^+-ions and poor in Na^+-ions. Whereas it is vice versa at the basal pole, the perilymph has a very low content in K^+-ions but is rich in Na^+-ions. A considerable difference in the concentration of K^+-ions is also present between the endolymph (rich in K^+-ions) and the cytosol of the hair cells (poor in K^+-ions). These differences in the concentration of K^+-ions are the reason for the endocochlear potential. This electrical gradient across the membrane of the stereocilia is the driving force that facilitates K^+-ions to flow into the hair cell after deflection of the hair bundle. The K^+-current causes a depolarisation of the cell. The depolarisation subsequently induces the opening of voltage-dependent calcium channels. Ca^{2+}-ions again are essential for the release of vesicles. This leads to a release of the neurotransmitter glutamate at the basal pole of the hair cell. The released glutamate diffuses across the synaptic cleft and initiates postsynaptic potentials in the next afferent neurone, which in turn causes the generation of action potentials. Through this process the transduction of an initial mechanical stimulus into a neuronal signal is completed. The

subsequent processing in the brain is not the subject of this work and, therefore, not further discussed in this introduction.

Like inner hair cells, outer hair cells generate oscillating receptor potentials in response to cochlear vibrations. However, in contrast to inner hair cells, outer hair cells respond to depolarisation with a cell contraction, whereas hyperpolarisation causes a lengthening of the cell. These changes in cell length in response to alterations in the membrane potential are called electromotility and are an exclusive feature of outer hair cells. The importance of this process lies in the generation of the so-called cochlear amplification, which is essential for auditory acuity in mammals (cf. 1.3).

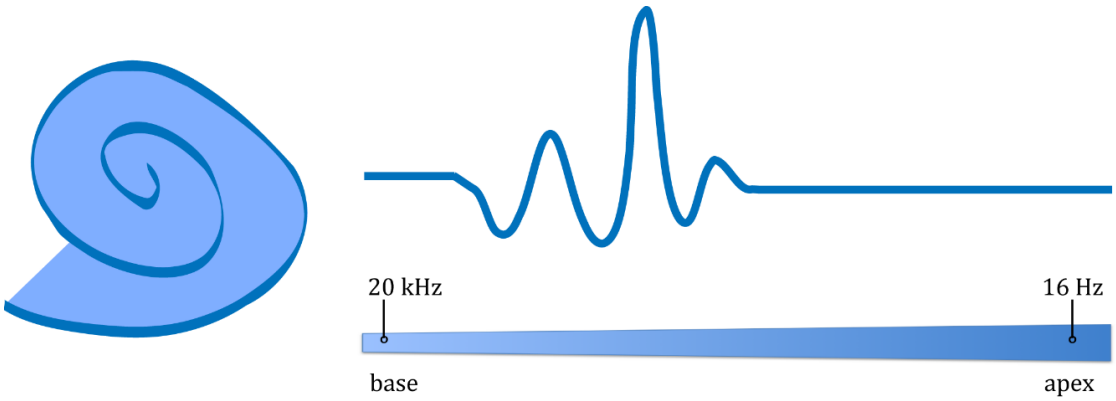

Figure 1.2: Tonotopy in the inner ear of mammals. On the left side: the wound cochlea. On the right side: the uncoiled basilar membrane with its displacement as a function of frequency of the incoming sound wave. The upper graph illustrates the deflection with a maximum at a defined position along the length of the basilar membrane. The lower graph: High frequencies produce maximum displacements near the oval window (base), with decreasing frequencies the maximum displacement of the travelling wave moves up to the apex of the cochlea. This is caused by the mechanical properties of the basilar membrane, which is stiff and narrow near the oval window and becomes wider and more compliant toward its apical end.

Zebrafishes do not have a tympanic membrane. The Weberian apparatus connects air bladder and inner ear (Bang et al., 2001). The Weberian ossicles transmit the vibrations as part of the Weberian apparatus. In the case of zebrafish, a sound wave hits the lateral window of the bony capsule, in which the air bladder is embedded. Thus, the air bladder starts to vibrate and as a consequence the sound wave is transferred via the Weberian ossicles to the unpaired perilymphatic sac. From the perilymphatic sac it travels to the unpaired endolymphatic sac and finally to the inner ear. Because of the unpaired sound conductions, the transferred sound is missing the component of sound direction. The inner ear of zebrafish is equipped with only one type of hair cells. The stereocilia of the hair cells are attached to the otolith membrane (Nicolson, 2005). The forwarded sound wave causes deflection of the stereocilia. Deflection of the hair bundle towards the tallest stereocilium opens mechanosensitive channels and results in a depolarisation of the hair cell, which

causes the opening of calcium channels and the release of neurotransmitter at the basal end of the hair cell. This mechanotransduction is mechanically essentially identical to those processes in mammalian vertebrates. Each frequency triggers stereocilia deflection with a local stimulation maximum, even though this kind of tonotopy is less precise as in the mammalian ear (Popper & Fay, 1993; Weiss et al., 2009).

There is no hair cell electromotility in non-mammalian vertebrates. Nevertheless, amplification has been described but is thought to be based on a fundamentally different mechanism, i.e. the reciprocal operation of mechanotransducer channels in their non-motile hair cells (Hudspeth, 1997; Hudspeth, 2005).

1.3 Cochlear amplification

Cochlear amplification is a positive feedback mechanism by which the energy of the travelling wave is locally amplified within the inner ear. It is essential for the exquisite sensitivity of mammalian hearing. The cochlear amplification is most efficient at low sound levels, but levels off towards increasing sound levels.

The outer hair cells play an important role for this process. Their contraction and elongation in response to voltage stimulation locally enhances the vibration energy of the travelling wave along the basilar membrane. The molecular motor behind this cell motion is the protein prestin, which is exclusively expressed in the basolateral membrane of outer hair cells. It bears unique properties providing the molecular basis of cochlear amplification.

Besides prestin, another pre-requisite of cochlear amplification is the attachment of the stereocilia of outer hair cells to the tectorial membrane. This linkage is a specialised feature of outer hair cells, but not of inner hair cells (Figure 1.3). It allows the basilar membrane to move relative to the tectorial membrane, where this movement is further amplified through the electromotile response of the outer hair cells upon voltage stimulation (Figure 1.4).

The cochlear amplification by the outer hair cells amplifies the mechanical stimulus into an adequate signal that the inner hair cells transduce into a neural response. This mechanism is most important at low sound levels. Moreover, cochlear amplification is limited to a particular locus within the cochlea. Thus, it strongly contributes to the excellent frequency resolution of the auditory system in mammals (Dong & Olson, 2013; Rhode, 2007). Consequently, a loss of outer hair cells results in hearing impairment and is in fact one of the major causes of human hearing loss (Liberman et al., 2002; Chen et al., 2008).

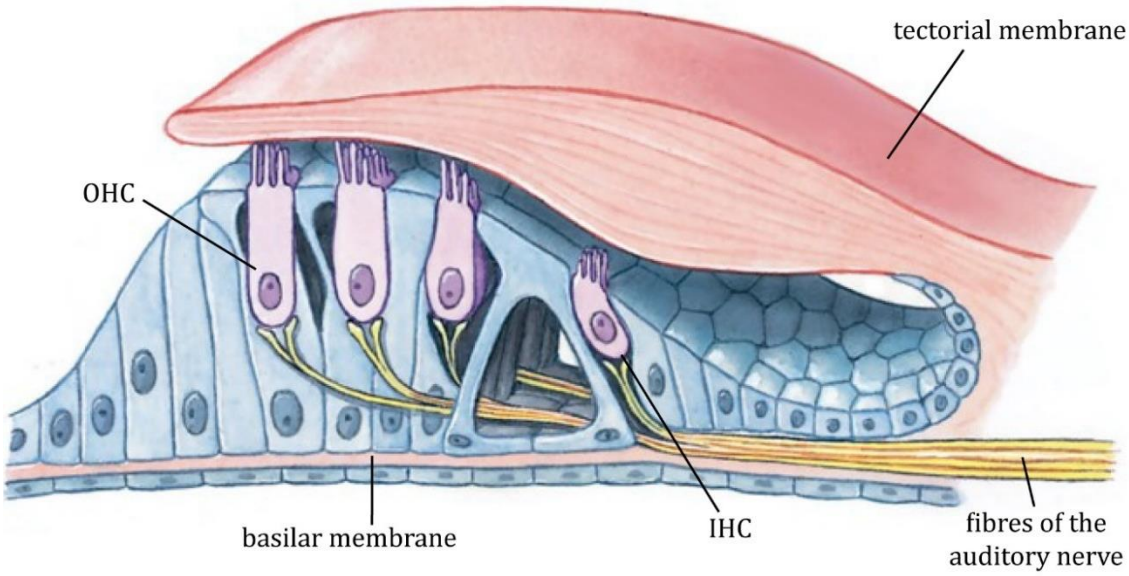

Figure 1.3: Organ of Corti. The figure shows three outer hair cells (OHCs) and one inner hair cell (IHC) representing three rows of OHCs and a single row of IHCs, which are found in the organ of Corti in mammals. These sensory cells are located between the basilar membrane at the bottom and covered by the tectorial membrane at the top. Note that the stereocilia of the OHCs are attached to the tectorial membrane but not those of the IHC. Both types of hair cells are connected to afferent and efferent nerve fibres. Image modified from Silverthorn, 2009.

The outer hair cell motility can be described as a piezoelectrical phenomenon. Brownell et al. (1985) first observed the electromotility of outer hair cells. Changes in the electrical membrane potential cause changes in the cell length; and vice versa, stretching and compressing of the basolateral membrane of outer hair cells results in changes in the membrane potential (Gale & Ashmore, 1994; S Kakehata & Santos-Sacchi, 1995). Cells contract in response to depolarisation and cells elongate in response to hyperpolarisation (Figure 1.4).

During patch-clamp measurements in outer hair cells, capacitive currents are detectable that show a nonlinear behaviour with respect to voltage. These currents are caused by charge movements within the membrane and can be measured electrophysiologically using voltage step protocols. The integral of these currents corresponds to the moved charge Q, where Q shows a sigmoidal voltage dependence. The relation between the voltage V and the charge Q can be described by a two-state model. The slope of the Q-V curve corresponds to membrane capacitance and is referred to - because of its nonlinear dependence on the voltage of the membrane - as nonlinear capacitance (NLC). Earlier studies demonstrated the maximal charge transfer correlates with the maximal change in cell length in outer hair cells, thus the NLC is often used as an experimental proxy of electromotility (Figure 1.7). The Boltzmann function describes the fractional population of the two states or, equivalently, the probability for each elementary motor unit to occupy either of these two states (cf. 1.4.3.1 and 2.6.1).

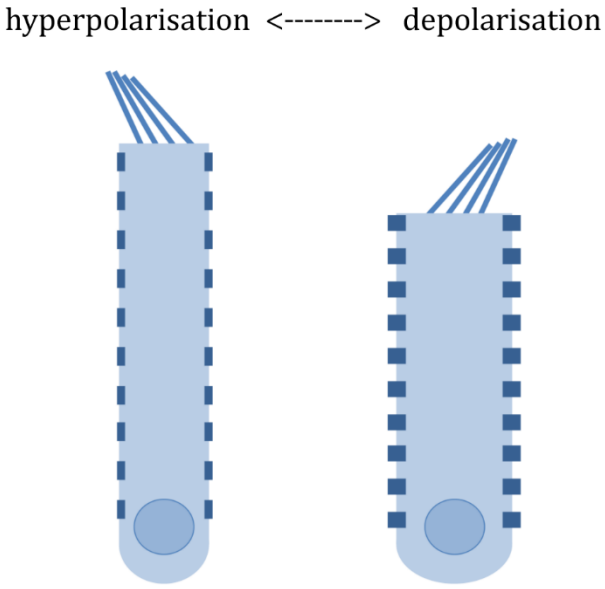

Figure 1.4: An outer hair cell in its elongated and contracted state. Outer hair cells change their length in response to changes in the membrane potential. Depolarisation results in a contraction of the cell, hyperpolarisation causes an elongation. The squares (dark blue) represent prestin proteins in the basolateral membrane of an outer hair cell that change their conformation in dependence of the electrical field across the membrane.

1.4 Prestin

1.4.1 Mammalian prestin

In 2000, Zheng and co-workers succeeded in identifying prestin as the protein being responsible for electromotility in mammals (Zheng et al., 2000a). They isolated mRNA from microdissected gerbil cochleas and identified transcription products that were only found in outer but not in inner hair cells. After cloning of cDNA of these sequences and transfection of TSA 201 cells with it, led to the identification of one sequence that produced NLC signals and conferred electromotility in heterologous systems.

In addition to capacitive responses of mammalian cells that heterologously express prestin, transfected cells also respond to salicylate, a known blocker of the NLC in outer hair cells (Zheng et al., 2000b). Furthermore, outer hair cells of prestin knock-out mice and of prestin (V499G/Y501H) knock-in mice show a lack of electromotility and cochlear amplification (Liberman et al., 2002; Dallos et al., 2008). These studies confirmed that prestin is the essential molecule for electromotility in outer hair cells.

The gene *SLC26A5* (**Sol**ute **C**arrier) codes for prestin. Human prestin is located on chromosome 7q22.1 and consists of twenty exons (Liu et al., 2003). The gene encodes a protein of 81.4 kDa with 744 amino acids. Prestin is a transmembrane protein that is exclusively localised in the basolateral membrane of outer hair cells, where it is densely packed and particularly accumulated in cholesterol-rich microdomains (Sturm et al., 2007).

Prestin is a member of the SLC26 (**Sol**ute **C**arrier) family, which is part of the SulP (**Sul**fate **P**ermease) superfamily. All known members of the SLC26 family, except prestin, transport

anions across the cell membrane. Non-mammalian prestin orthologues are anion-exchangers with a stoichiometry of 1:1, where a chloride anion is transported in exchange for a divalent anion, e.g. oxalate or sulphate (Schaechinger & Oliver, 2007a). This anion exchange is reversible dependent on driving forces. Remarkably, prestin is the only member of the SLC26 family, which does not function as transporter but produces electromotility (Mount & Romero, 2004).

Ten functional members of the SLC26 family were identified in vertebrates, but homologs were also found in many other organisms such as invertebrates, plants and bacteria (Dorwart et al., 2008). Prestin itself is highly conserved among different species. In mammals prestin is exclusively expressed in outer hair cells (Zheng et al., 2000b). The prestin orthologues of zebrafish and flies are also expressed in auditory organs even though they do not seem to cause electromotility (Weber et al., 2003).

Prestin has fourteen transmembrane domains (Gorbunov et al., 2014) and a STAS (**S**ulfate **T**ransporter and **A**nti-**S**igma factor antagonist) domain at its C-terminal end (Figure 1.5). Gorbunov and co-workers used homology modelling, MD simulations as well as experimental data to predict a 7+7 inverted repeat architecture of prestin. The model is based on the bacterial uracil transporter UraA and compared the sequences of UraA and rat prestin. The transporter UraA belongs to the nucleobase/cation symporter 2 (NCS2) proteins. The NCS2 proteins have an evolutionary proximity with the SLC26/SulP family, which made the UraA an appropriate template for homology modelling (Schlessinger et al., 2010; Höglund et al., 2011; Gorbunov et al., 2014). Furthermore, a high-resolution crystal structure of UraA was published in 2011 (Lu et al., 2011). The predicted fourteen transmembrane domains are α-helical except for two short β-sheets in the transmembrane domains 3 and 10. The N- and C-terminal ends are placed intracellular. It has been assumed that prestin molecules form oligomers. Homomultimers of two or four subunits have been hypothesised (Zheng et al., 2006; Detro-Dassen et al., 2008; Hallworth & Nichols, 2012). New structural information on bacterial SLC26 homologs and on prestin was revealed recently and supports dimerisation for SLC26 transporters in general (Chang et al., 2019). Based on the structure of UraA, prestin is predicted to form a highly hydrophobic anion translocation pathway with a central cavity that mainly consists of the transmembrane domains 1, 3, 8 and 10 (Gorbunov et al., 2014) (cf. Figure 1.9). Furthermore, there are two crystallographic structures of members of the SLC26 protein family. The first one was resolved for SLC26Dg, a prokaryotic fumarate transporter, and the second one was recently published based on crystallography of the murine SLC26A9 (Geertsma et al., 2015; Walter

et al., 2019) . These two experimental structures fully support the previous homology model based on UraA.

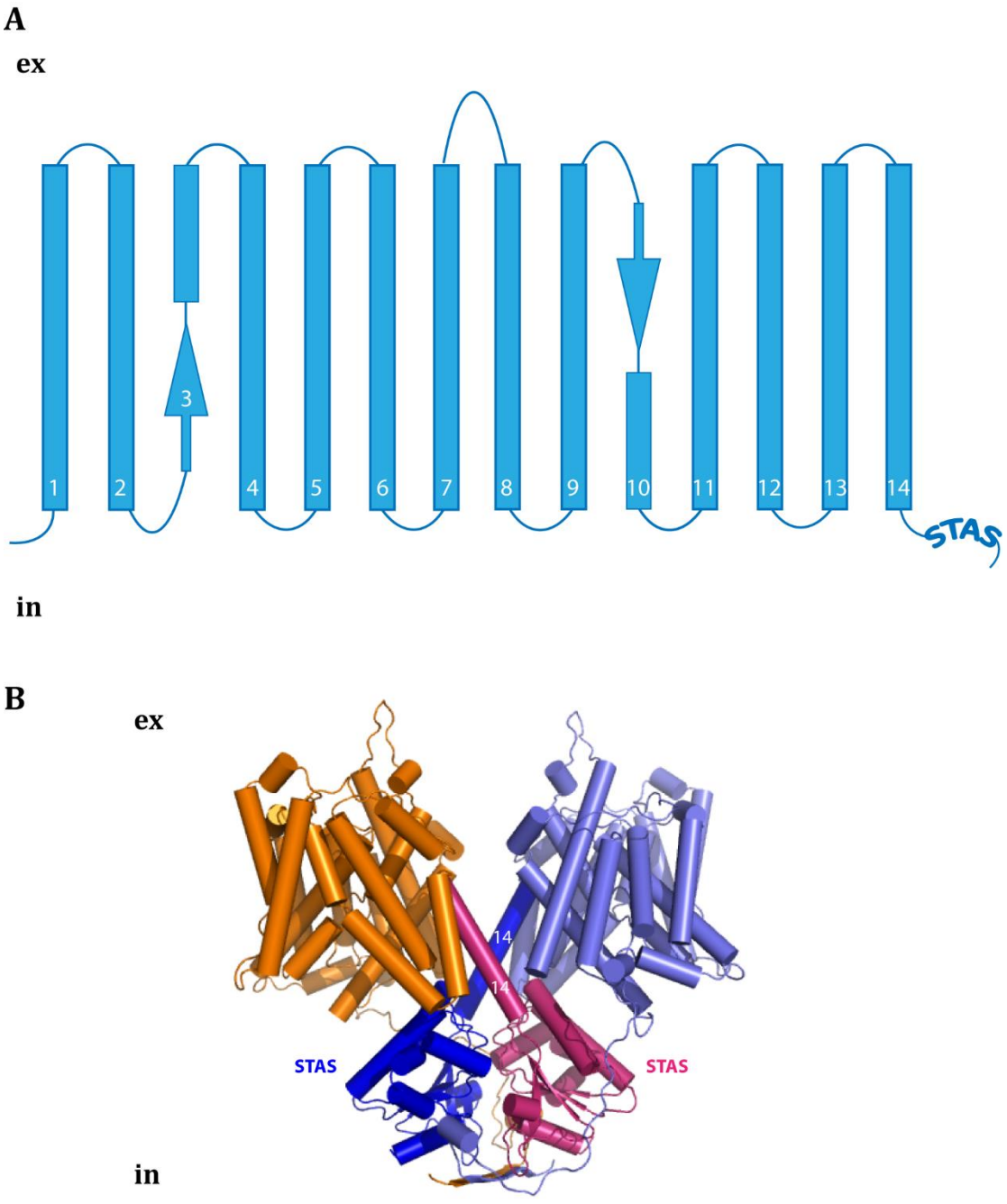

Figure 1.5: Structural model of prestin. A: SLC26A5 has fourteen transmembrane domains with a 7+7 inverted repeat architecture. Both ends of the protein are cytosolic. At the C-terminus a STAS (**S**ulfate **T**ransporter and **A**nti-**S**igma factor antagonist) domain is present, which all members of the SulP family share. Image modified from (Gorbunov et al., 2014). **B**: A dimer of prestin with one monomer in blue and the other one in orange. The model is based on the SLC26A9 (Walter, Sawicka & Dutzler, 2019) aligned with the model of rat prestin. The domains are shown as cylindrical helices. The transmembrane domains (TM) 14 and the STAS domains of the monomers are in close contact (additionally highlighted in pink and dark blue) and especially TM 14 was recently identified as the interface of prestin dimers by Chang et al., 2019.

1.4.2 Non-mammalian prestin orthologues

In contrast to mammalian prestin, non-mammalian prestin orthologues are transport-capable proteins, which work as electrogenic anion-exchangers (Schaechinger & Oliver, 2007b). They are found across vertebrates, although only few have been studied in detail, e.g. chicken (*Gallus gallus domesticus*) and zebrafish (*Danio rerio*) (Albert et al., 2007). Since these prestin orthologues are already well characterised in their function, they serve as ideal model systems to identify common molecular features of the transport mechanism in the SLC26 protein family.

Chicken and zebrafish prestin orthologues generate NLC, but, according to current knowledge, do not produce electromotile changes in cell length. In addition, the NLC characteristics vary from chicken and zebrafish prestin to mammalian prestin (Albert et al., 2007).

The distinct functional properties while sharing a high sequence similarity make zebrafish prestin an attractive model to investigate the transport mechanism of SLC26 transporters. Rat and zebrafish prestin share a high degree of sequence homology; it is about 54 % identity at the protein level. All this indicates structural and mechanistic similarities to mammalian prestin. For this study mainly zebrafish prestin as representative of non-mammalian prestin was investigated.

1.4.3 Mechanistic models of electromotility

The mechanism of the SLC26-mediated transport is not fully understood. A potential role of this transport mechanism in the electromotile properties of prestin is elusive, but based on the high sequence similarity of transport-capable and electromotile prestin orthologues the idea arose that both are related and electromotility evolved from transport. This is further supported by the finding that the motor protein prestin interacts with and only undergoes conformational rearrangements in the presence of intracellular monovalent anions (Schaechinger et al., 2011). Based on previous studies several mechanistic models of anion transport and electromotility were suggested and will be described in the following sections. Some of these models are complementary, others are competing.

1.4.3.1 Model of incomplete transport cycle and allosteric modulation of mammalian prestin

The hypothesis of an incomplete transport cycle has been proposed as the mechanistic basis for the generation of electromotility. In this model prestin binds an anion on its intracellular side that moves along a transport pathway in response to changes in the membrane potential. In turn, this movement will initiate conformational changes of prestin resulting

in changes in the cell length of the outer hair cell and in the NLC in outer hair cells and heterologously expressing CHO cells (Schaechinger et al., 2011; Gorbunov et al., 2014).

Additionally, removal of intracellular chloride resulted in an abolishment of the NLC in outer hair cells of rats (Oliver et al., 2001). Thus, intracellular anions, e.g. chloride, are necessary for the electromechanical function of prestin. This finding paired with the lack of anion release on the extracellular side led to the assumption that prestin undergoes an incomplete transport cycle.

Furthermore, the findings that the non-mammalian prestin orthologues can generate voltage-dependent charge movement and NLC (Albert et al., 2007) has led to the idea that electromotility mechanistically results from an incomplete transport (Schaechinger et al., 2011). This incomplete transport of prestin might have evolved from an ancestral anion transport mechanism conserved in the SLC26 transporter family (Figure 1.6). This incomplete transport excludes an outward-open conformation; the protein binds an anion from the cytosolic side in the inward-open conformation and rearranges into an intermediate/occluded state, but fails to unload the bound anion at the extracellular side of the cell.

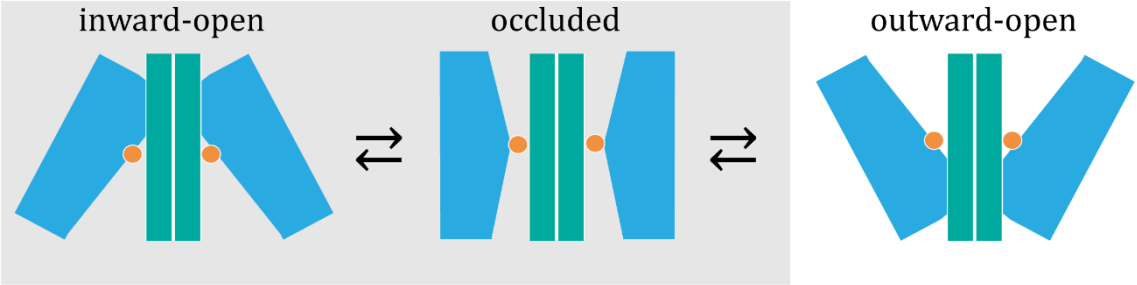

Figure 1.6: Schematic depiction of elevator-like conformational transitions during a transport cycle of prestin, which allow for alternating-access of the anion-binding site. Two prestin proteins form a dimer. The gate domain (teal) is the scaffolding along which the core domain (blue) moves during a transport cycle. The anion (orange circle) is bound to the core domain. With a rigid movement of the core domain the anion gets access to the other side of the membrane. An incomplete transport cycle is suggested for mammalian prestin, in which the outward-open conformation is never reached.

This model was attractive because it involved the charge movement as being associated with electromotility and the relationship of prestin to other SLC26 transporters. However, it failed to explain one aspect: the slope of the NLC signals changes only slightly when intracellular monovalent anions (e.g. chloride) are exchanged by multivalent anions such as sulphate (Rybalchenko & Santos-Sacchi, 2008). Since the slope of the Q-V-curve reflects the amount of net charges that are moved across the membrane, the transport of a polyvalent anion – if mechanistically identical to the transport of the monovalent anion – should affect the slope. Therefore, the model had to be refined, which was done by including an

alternative allosteric modulation mechanism. In this mechanism the binding of an anion to a site distinct from the anion translocation pathway is assumed to initiate an allosteric change in the protein structure, which facilitates the anion in the central cavity to move as voltage sensor across the membrane (Rybalchenko & Santos-Sacchi, 2008).

1.4.3.2 Area motor model

In the early 1990s, the idea of the area motor model was first published to describe the observed changes in cell length in outer hair cells (Dallos et al., 1993; Iwasa, 1994). As area motor, prestin's 3D-structure changes its spatial expansion in the membrane plane in response to voltage stimulations. The area motor model proposes that the sum of size changes of all prestin proteins finally causes the contraction or elongation of the outer hair cells (Kalinec et al., 1992; Santos-Sacchi & Song, 2014b). The most simple biophysical model is based on the assumption that prestin can switch only between two states, a compact and an extended state (Dallos et al., 1991).

The probability of the state depends on the membrane potential and can be described by a Boltzmann distribution (cf. 2.7). The first derivate of the Boltzmann function reflects the NLC depending on the voltage and delivers the three important parameters: peak capacitance, $V_{1/2}$ and slope.

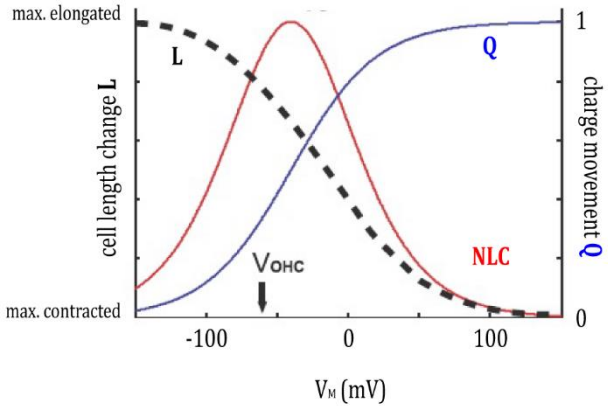

Figure 1.7: The connection between changes in the cell length, charge movement and the nonlinear capacitance (NLC). The technical read-out of the electromotility is the bell-shaped NLC, the first derivative of the Q-V curve. The NLC peaks at the $V_{1/2}$, which is the point where the charge is equally distributed on either side of the membrane. The change in cell length is also voltage-dependent, the cell contracts in response to depolarisation. A typical value of the $V_{1/2}$ in outer hair cells is additionally marked on the voltage axis. Image modified from Ashmore, 2008.

The peak capacitance is influenced by the expression level of prestin and the number of proteins targeted to the membrane. Mutations in prestin can have an impact on the size of the NLC. Furthermore, outer hair cells deliver large NLC signals due to the high expression levels of prestin and its dense arrangement in the cell membrane. Rat prestin heterologously expressed in CHO cells provides cells with piezoelectrical properties similar to those in outer hair cells, but the signal amplitude of outer hair cells has not been achieved so far in heterologous expression systems (Ludwig et al., 2002).

$V_{1/2}$ is the membrane voltage, where the charge movement within the membrane is half maximal. This value corresponds to the peak of the NLC signal. In outer hair cells, the $V_{1/2}$ is at about -70 mV (Santos-Sacchi, 1991) that is close to the resting membrane potential of these cells. It is determined by many factors such as ionic conditions, membrane pressure and stiffness (Ludwig et al., 2002; Rajagopalan et al., 2010).

The slope of the NLC is the voltage dependence of the capacitance and is less variable than the $V_{1/2}$ with a value between 30 and 40 mV (Oliver & Fakler, 1999; Ludwig et al., 2002). However, the slope can also be affected by ionic condition (Oliver et al., 2001). It is defined as the amount of charge that moves through the membrane per functional unit, which correlates with the change in cell length per voltage unit (Figure 1.7).

Furthermore, prestin differs fundamentally in structure and function from other known motor proteins like myosin, kinesin or dynein (Frank et al., 1999). Its electromotile response is independent of ATP and Ca^{2+}-ions, and yet extremely fast (at microsecond rates). In addition, its function is directly coupled to the membrane potential making it an ultrafast voltage-dependent motor protein (Dallos et al., 1991).

1.4.3.3 Anion translocation extends the area motor model

The area motor model is a pure biophysical description of the observed changes in cell length of outer hair cells. With knowledge of prestin's belonging to the transporter family SLC26, a connection between electromotility and anion translocation was investigated.

The changes in the protein structure require the interaction of prestin with an anion. NLC was proposed to result from binding chloride to a cytosolic binding site and its movement across the membrane electrical field without releasing it at the extracellular side of the cell (Oliver et al., 2001). Non-mammalian prestin orthologues are anion transporters, which mediate a 1:1 electrogenic exchange of chloride with oxalate or sulphate (Schaechinger & Oliver, 2007b). Bai and colleagues discovered transport of oxalate and formate by gerbil prestin heterologously expressed in CHO cells (Bai et al., 2009). This transport is independent of prestin's voltage-sensitive electromotile properties and its significance to outer hair cells is not known.

Combined with the early model of the area motor, prestin is elongated when the anion is positioned near the entrance of the anion translocation pathway and it is contracted when the anion moves deeper into the protein towards the extracellular side. Here, the hypothesis is that NLC is produced by the passage of the anion within the protein.

1.4.3.4 Model of alternating-access to the anion-binding site

The increasing number of crystallographic structures of transporters provides information about multiple functional states (cf. Figure 1.8), in which transporters were crystallised. These different functional states help to understand the molecular mechanism of substrate transport. Crystal structures of the distantly related SLC4 and SLC23 family were published in recent years. The SLC4 family includes several classical bicarbonate transporters. Its most prominent member is the anion-exchanger AE1 of which a crystal structure in the outward-open conformation is available (Arakawa et al., 2015). One year later, Thurtle-Schmidt and Stroud presented the crystal structure of Bor1 (also SLC4 family) in an occluded state (Thurtle-Schmidt & Stroud, 2016). By comparing both structures, the authors conclude structural transitions with alternating-access in an elevator transport mechanism. Crystal structures of two SLC23 family members were published, of UapA in the inward-open conformation (Alguel et al., 2016) and of UraA in an occluded state (Yu et al., 2017). In conclusion, comparison of these two structures also suggests an elevator transport in the SLC23 family. This information instructed a basic model for transport of members of the SLC26 family.

The substrate-binding site is accessible form either the intracellular or extracellular site of the cell membrane resulting in an alternating accessibility (Figure 1.8). There are three different alternating-access mechanisms identified across many transporter families so far: rocker switch, rocking bundle and elevator (Drew & Boudker, 2016). These mechanisms distinguish between a moving and a fixed barrier. Mitchell introduced the term of a moving-barrier mechanism (Mitchell, 1957 & 1990). Here, a substrate binds at the interface of two domains and a barrier hinders the passage across the membrane. Binding of the substrate causes conformational rearrangements and the movement of the barrier to allow for alternate access. A moving-barrier mechanism is described for the rocker switch and rocking bundle model. The main difference between these two mechanisms is that rocker switch transporters have two structurally symmetric main domains, whereas in rocking bundle transporters two structurally dissimilar domains realise alternating-access (Drew & Boudker, 2016). In contrast, the elevator principle has a fixed barrier at the interface of two distinct domains. In this mechanism, the substrate binds to one domain which subsequently moves along the other rigid domain to surmount the barrier. The rigid domain is referred to as scaffold or gate domain, whereas the substrate-binding mobile domain is referred to as core domain.

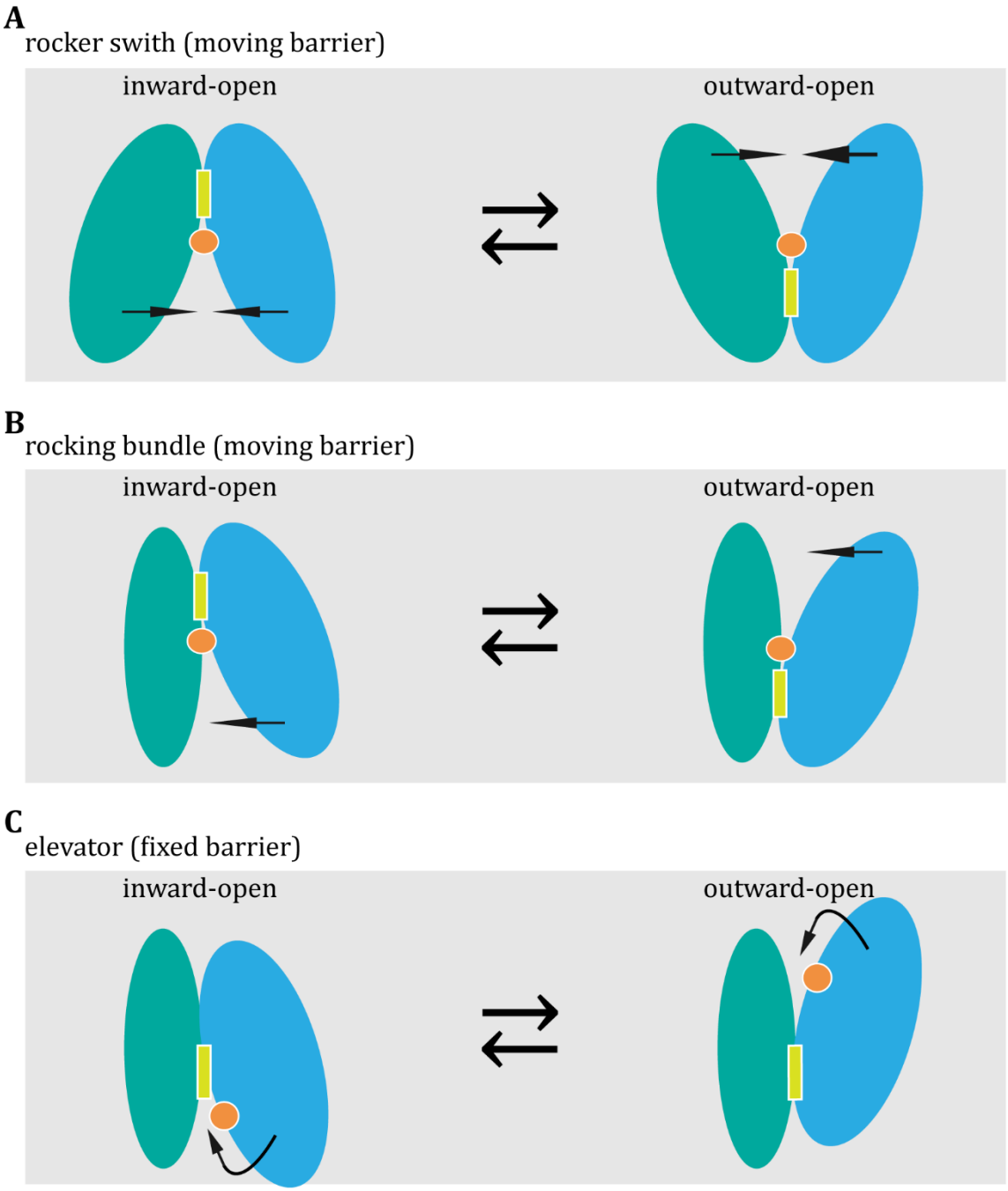

Figure 1.8: Three mechanisms of alternating-access in transporters. The three mechanisms of alternating-access differ between a moving (**A+B**) or fixed (**C**) barrier (yellow rectangle), which is at the interface of the two domains of a transporter protein. There are illustrations of the inward-open and of the outward-open conformations but the intermediate (occluded) state is not shown for a better overview. **A:** There is a moving barrier in the rocker switch mode. The substrate (orange circle) binds between two similar domains and thereby introduces a rearrangement of the domains, which leads to an alternating-access of the central cavity. **B:** The rocking bundle mechanism is similar to A but has two dissimilar domains. **C:** There is a fixed barrier in the elevator alternating-access. Furthermore, the substrate only binds to one of the dissimilar domains. The substrate-binding domain moves along a relatively immobile domain to transport the substrate across the cell membrane. Image modified from Drew & Boudker, 2016.

A recent study published a crystallographic structure of the prokaryotic fumarate transporter SLC26Dg (Geertsma et al., 2015). The authors suggest the translocation of the substrate-binding site by movement of the entire core domain against the gate domain

allows for an alternating-access to the anion-binding site. This leads to the assumption that this SLC26 family member transports substrates in an elevator-like manner across the membrane. Furthermore, the cryo-EM structure of the murine SLC26A9 provided the first high-resolution structure of a eukaryotic SLC26 family member and supported an alternating-access mechanism by SLC26 (Walter et al., 2019). If the whole SLC26 family also translocates anions in an elevator-like manner and, especially, if prestin-mediated voltage-dependent changes in cell length are based on this mechanism needs to be clarified.

1.4.3.5 Model of a multistate mechanism in the anion transport of prestin

Another approach suggests a kinetic model, the so-called *meno presto model*, where a multistate mechanism underlies electromotility (Santos-Sacchi & Song, 2014a & 2014b). After the initial binding of chloride to prestin, the protein undergoes a slow transition into an intermediate state that allows the voltage-dependent charge movement.

1.4.4 Common principles describing prestin's function

Concerning all models described above, there is the general agreement that intracellular chloride is required for electromotility regardless of its function as extrinsic voltage sensor (Oliver et al., 2001), as allosteric-like modulator (Rybalchenko & Santos-Sacchi, 2003) or regulator of prestin's kinetics in the transition between multiple states (Santos-Sacchi & Song, 2016). It is conceivable that there is an electrostatic barrier, which has to be overcome to translocate the anion. Whether this happens through the binding of chloride to prestin remains an open question. Furthermore, there are new data about a rat prestin mutant with a mutation in the region of the putative anion-binding site. The mutant S396E mimics a bound anion by the mutation of serine to glutamate. This mutant functions independently of intracellular anions, which demonstrates that the fixed negative charge at the putative anion-binding site is sufficient for the voltage-dependent function of prestin. Thus, the S396E mutant will allow for detailed kinetic studies that may explain the electromotile activity of prestin.

1.5 Cysteine accessibility scan to elucidate prestin's protein dynamics

The previous sections addressed potential model scenarios of the molecular dynamics, which may be underlying prestin's electromotile mechanism. An experimental approach to work out these molecular dynamics is to identify structures that change their accessibility to the aqueous medium along a transport cycle or with the electromotile conformational changes is a cysteine accessibility scan (SCAM: cf. 2.4). Single positions can be studied for their accessibility to thiol-specific reagents, i.e. in consequence to the aqueous medium. These reagents are either applied from the extra- or the intracellular side of the membrane and the accessibility of an amino acid verifies its orientation within the protein. The

investigation of the accessibility of certain amino acids is, therefore, a useful approach to test the different model concepts. Two transmembrane domains are of special interest in this context, namely transmembrane domain 3 and 10 (Figure 1.9). These transmembrane domains are predicted to be part of the central cavity. Furthermore, the putative anion-binding site is also located in transmembrane domain 10 (Gorbunov et al., 2014).

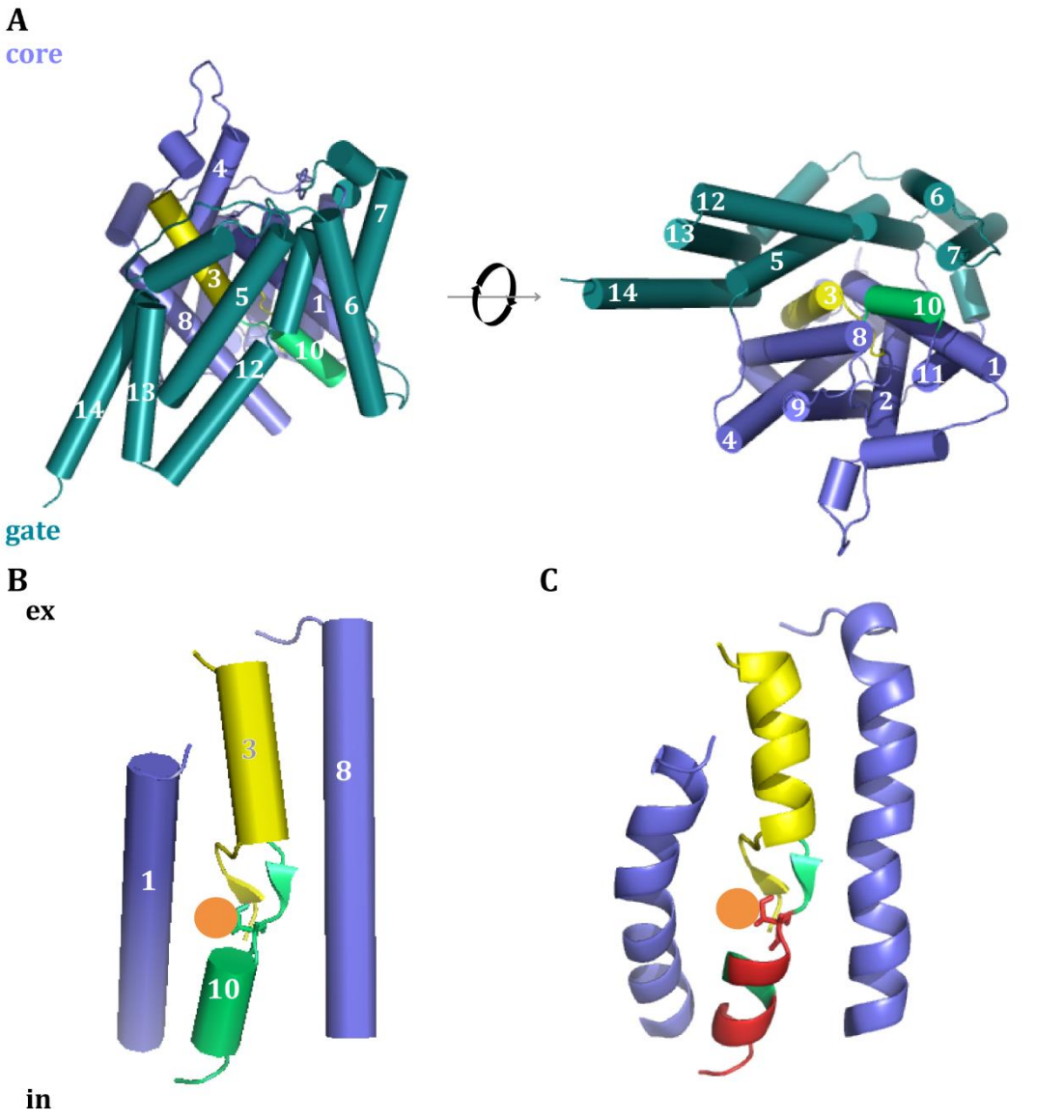

Figure 1.9: Structural homology model of rat prestin based on UraA. A: This part provides an overview on a single monomer of rat prestin without STAS domain. The transmembrane domains (TM) of the gate domain (TM 5-7 and 12-14) are coloured in teal, of the core domain (TM 1-4 and 8-11) in blue and the domains in the front are numbered. In addition, the domains of interest to be studied in this thesis are coloured in green (TM 10) and yellow (TM 3). On the right side, the molecule is tilted and the view direction into prestin is from the intracellular side. **B** and **C:** Only parts of the core domain are shown. These TMs are predicted to be part of the central cavity of prestin. The focus is on TM 3 and 10. The putative anion-binding site is in rat prestin within TM 10 around position S396 (shown in stick representation). The anion bound to S396 is indicated as orange circle. **C:** The model highlights positions in TM 10 in red, which are known to be accessible from the intracellular side by MTS reagents (Gorbunov et al., 2014). The model is based on the results of Gorbunov et al., 2014.

1.6 Aim of this study

Molecular dynamics that underlie the transport mechanism of the SLC26 protein family have remained largely elusive. Furthermore, it has been suggested but remains to be tested whether electromotile prestin undergoes structural dynamics that are similar to those of transport-capable members of the SLC26 family. Therefore, this study aims to elucidate whether the function of the SCL26 transporters and voltage-driven motors follow common structural principles. To achieve this aim, two members of the SLC26 family were used as model systems: the non-mammalian zebrafish prestin as a prototypical and highly active transporter and the mammalian rat prestin as a motor with a putatively underlying incomplete anion transport mechanism.

Recent studies of other SLC family members show crystal structures in different conformational states, which suggest a shared alternating-access mechanism for this membrane transporter family (Geertsma et al., 2015; Walter et al., 2019). Furthermore, the results of Geertsma et al. (2015) propose an elevator-like movement for a prokaryotic SLC26 family member (cf. 1.4.3). However, it still remains to be shown whether prestin uses the same mechanisms and, in particular, whether it is the anion transport which underlies electromotility.

The strategy to shed light on this issue is to perform a cysteine accessibility study (cf. 1.5 and 2.4). Therefore, single amino acids within these proteins were studied for their importance in the transport function. Here, amino acids of interest were chosen based on previous structural modelling data by Gorbunov et al., 2014. The work presented here focused on the transmembrane domains 3 and 10, because both domains are proposed to be part of the pathway for the anion to bind to prestin. Furthermore, the central positions within these amino acid stretches are thought to contribute to forming the anion-binding site. Importantly, these positions may undergo translational movements in the hypothetical elevator movements of the core domain and their accessibility can thus inform about the occurance and the travel of such – as yet hypothetical – molecular dynamics.

Single residues in transmembrane domain 3 and 10 (cf. Figure 1.9) of rat and zebrafish prestin were individually substituted towards cysteines, and their accessibility to the aqueous medium was tested by the application of thiol-specific reagents. The scanning of transmembrane 10 of rat prestin was already performed (Gorbunov et al., 2014). As read-out for chemical modification and hence accessibility, activity of the SLC26 variants before and after the application was tested by patch-clamp recordings in transiently transfected cells. Protein expression and cellular localisation were investigated via confocal microscopy.

2 Materials and methods

2.1 Chemicals

The chemicals used are listed with information of the manufacturer and the CAS-number in Table 2.1.

Table 2.1: Used chemicals.

Chemicals	**Manufacturer**	**CAS-number**
Calcium chloride ($CaCl_2$)	Fluka	10043-52-4
Caesium chloride (CsCl)	Sigma-Aldrich	7647-17-8
Caesium hydroxide monohydrate (HCsO)	Sigma-Aldrich	35103-79-8
Caesium iodide (CsI)	Sigma-Aldrich	7789-17-5
D-(+)-Glucose	Sigma-Aldrich	50-99-7
DTT (Dithiothreitol)	Sigma-Aldrich	34-83-12-3
EGTA (Ethylene glycol-bis(2-aminoethylether) - N,N,N′,N′-tetraacetic acid)	Fluka	67-42-5
HEPES (4-(2-hydroxyethyl)-1piperazine ethane sulfonic acid)	Sigma-Aldrich	7365-45-9
Hydrogen peroxide (H_2O_2)	Sigma-Aldrich	7722-84-1
Latrunculin A	Adipo Gen	76343-93-6
Magnesium chloride ($MgCl_2$)	Fluka	7786-30-3
Methyl-ß-Cyclodextrin (MßCD)	Sigma-Aldrich	128446-36-6
MTSES ($C_3H_7O_5S_3$*Na)	Toronto Research Chemicals	184644-83-5
MTSET ($C_3H_{16}BrNO_2S_2$)	Toronto Research Chemicals	91774-25-3
Oxalate dihydrate ($(COOH)_2$*$2H_2O$)	Fluka	6153-56-6
Phenol sulfonic acid ($C_6H_6O_4S$)	Sigma-Aldrich	1333-39-7
Potassium chloride (KCl)	Roth	7447-40-7
Sodium-L-Aspartate ($C_4H_8NNaO_5$)	Sigma-Aldrich	323194-76-9
Sodium chloride (NaCl)	Sigma-Aldrich	7647-14-5
Sodium hydrogen phosphate (NaH_2PO_4)	Roth	10049-21-5
Sodium hydroxide (NaOH)	Fluka	1310-73-2
Sodium salicylate ($C_7H_5O_3$*Na)	Fluka	54-21-7

The chemicals used for the cell culture are separately listed in section 2.2.

2.2 Cell lines and cell culture

2.2.1 CHO cells

The experiments for this work were mainly done with the cell line CHO $dhFr^-$, which is a subclone of the CHO cell line (***C****hinese* ***H****amster* ***O****vary*). CHO cells are epithelial cells from the ovary of an adult Chinese hamster (*Cricetulus griseus*), which were established as a cell line in 1957. The variant CHO $dhFr^-$ is negative for the enzyme dihydrofolate reductase. This

enzyme is necessary for the synthesis of purine and, therefore, CHO dhFr$^-$ are not able to grow without the exogenous addition of purines. These cells build adherent monolayers and have a doubling time of about 20-24 hours.

Media composition: MEM Alpha Medium (1x) (*Minimum Essential Medium, (+) Ribonuclesosides, (+) Deoxyribonucleosides; Lot. 1880330, Gibco by Life Technologies*)
+ 10 % FBS (*Fetal Bovine Serum Advanced; Lot. CP15-1440, Capricorn Scientific*)
+ 1 % Pen Strep (*Penicillin Streptomycin, (+) 10,000 Units/ml Penicillin, (+) 10,000 µg/ml Streptomycin; Lot. 1509763, Gibco by Life Technologies*)

2.2.2 HEK 293 cells

For comparison, some experiments were also performed in HEK 293 cells. This is a cell line, which was established from primary human embryonic kidney cells (***H**uman **E**mbryonic **K**idney*).

Media composition: DMEM + GlutaMAX (*Dulbecco´s Modified Eagle Medium, (+) 4,5g/l D-Glucose, (-) Pyruvate; Lot. 1906060, Gibco by Life Technologies*)
+ 10 % FBS (*Fetal Bovine Serum Advanced; Lot. CP15-1440, Capricorn Scientific*)
+ 1 % Pen Strep (*Penicillin Streptomycin, (+) 10,000 Units/ml Penicillin, (+) 10,000 µg/ml Streptomycin; Lot. 1509763, Gibco by Life Technologies*)
+ 1 % MEM NEAA (*MEM Nonessential Amino Acids (100x); Lot. CP13-1014, Capricorn Scientific*)
+ 1 % Sodium pyruvate (*Sodium Pyruvate 100mM (100x); Lot. 1553622, Gibco by Life Technologies*)

2.2.3 Passaging and seeding of cells

With slight variations the passaging and seeding of CHO dhFr$^-$ and HEK 293 cells were carried out similarly.

Cells were seeded in culture flasks (*TC-Flasche T75, Sarstedt*) containing the specified media (cf. 2.2.1 and 2.2.2) and stored in an incubator (*Heracell 150i*) at 37°C and 5 % CO_2 up to the

required confluence. A light microscope was used for optical control of the cell growth (*Olympus KX41*). The intended confluence for CHO dhFr$^-$ cells was 80 %, for HEK 293 cells 90 %, at which cells were passaged and seeded again. This work was done under an aseptic, sterile bench with laminar flow (*Thermo Scientific Clean Air DLF/REC 4 Kl 2A*). The bench itself as well as other work material were solely used in a sterile condition. Besides sterile purchased articles, pipette tips, Pasteur pipettes and Eppendorf reaction tubes were used after autoclave sterilisation (*Tuttnauer 3150 ELV*). In addition, the sterile bench itself as well as every article that was used at the bench were treated with 70 % w/v ethanol (96 % w/v ethanol denaturated by 1 % w/v MEK; obtained by the chemical storage of the chemistry department of Philipps-University Marburg). Cells were passaged when they reached the required confluence. Therefore, the medium was drained via a suction pump and cells were washed with PBS (*Dulbecco´s PBS (1x); Lot. CP15-1316, Capricorn Scientific)*. The cells were detached by adding trypsin (*0,5 % Trypsin-EDTA (10x); Lot. 1881866, Gibco by Life Technologies)* in PBS (1:10). Subsequent addition of medium laced with FBS stopped tryptic activity. Via centrifugation (1200 rpm, 2min; *Megafuge 2.0R, Heraeus Instruments*) cells were separated from cell debris and media. The supernatant was discarded and the cell pellet resuspended in 1 ml media. The desired amount of this suspension was added to culture flasks and petri dishes (*∅35mm, Cellstar; Greiner Bio-One*) with cover slips (*∅12mm; Art.Nr. P231.2, Roth*) that were prepared with media. In the case of HEK 293 cells these cover slips had to be coated with PDL (*Poly-D-Lysine; Lot. SLBT0548, Sigma Aldrich*).

2.2.4 Transfection of cells

For cells to express the desired protein they had to be transfected with a plasmid carrying the appropriate gene. CHO dhFr$^-$ cells were transfected with JetPei (*JetPei DNA Transfection Reagent; Product No. 101-40N, Polyplus transfection*), whereas HEK 293 cells were transfected with Lipofectamine (*Lipofectamine 2000 Reagent; Lot. 1445150, Invitrogen by Life Technologies*).

JetPei mainly consists of linear polyethylenimines, which cover the intrinsic charge of DNA. Thereby a complex of DNA and JetPei can bind to anionic proteoglycans on the cell surface and can be absorbed into the cell via endocytosis. The DNA dissolves from the complex in the cytoplasm and can be transported to the cell nucleus where its transcription takes place. CHO dhFr$^-$ cells were transfected at a confluence of about 50 % with 4 µg DNA and used for experiments about 48 hours later. The transfection was performed using the manufacturer's protocol.

Lipofectamine consists of cationic and neutral lipids, which are also capable of covering negatively charged DNA by enclosing it in a liposome. The neutral lipids chaperon the fusion

of positively charged liposomes with the negatively charged plasma membrane. HEK 293 cells were transfected at a higher confluence (~70-80 %) with 4 µg DNA following the manufacturer's protocol. Isolated cells were needed for patch-clamp measurements. Therefore, medium was drained 16-24 hours after transfection and cells were trypsinated and seeded on coated cover slips again. Measurements were performed after 24-48 hours.

The so transfected cells should express prestin and could be further investigated. The sequences of the wild type variants of rat and zebrafish prestin can be found in supplement 7.1. Because all prestin constructs were tagged with a green fluorescent protein (GFP), the expression and localisation of prestin could be checked by fluorescence of GFP. Besides wild type prestin, many mutants were investigated that were made via mutagenesis (cf. 2.3.1).

2.3 Molecular biology

2.3.1 Mutagenesis

Site-directed mutagenesis is a method to manipulate a certain DNA. Single or multiple nucleotides can be inserted, deleted or exchanged. Thereby, intended changes in the amino acid sequence of a gene product can be made. In case of the cysteine scanning single amino acids were mutated to alanines or cysteines.

The necessary primer pairs were complementary to the template DNA and designed with a length of about 20 to 35 base pairs, the requested mutation centrally located and if possible, with a content of ≥ 40 % CG and one or two C or G nucleotides at its end. The melting temperature should ideally be between 60-75°C. These properties as well as the exclusion of mismatches were checked with *Vector NTI*.

The subsequent polymerase chain reaction (PCR) was performed with the following reaction batch:

Pfu Ultra II Hotstart PCR Master Mix 2x (*Aligent*)	25 µl
H_2O (*Sigma*)	22 µl
Template DNA (10-100 ng)	1 µl
Forward primer (10 µmol/µl)	1 µl
Reverse primer (10 µmol/µl)	1 µl
∑	50 µl

The single PCR steps are indicated below:

Initial denaturation	95°C, 2 min
Denaturation	95°C, 20 sec
Annealing	60°C, 40 sec *
Elongation	72°C, 4 min
Final elongation	72°C, 3 min
Storage	16°C, ∞

* The annealing time was variable and adjusted consistent with the melting temperature of the designed mutagenesis primer pair. The melting temperature of the primer pair minus 5°C resulted in the annealing temperature. The three steps (denaturation, annealing and elongation) were performed for 16 cycles.

The newly developed PCR products were digested with *Dpn I* at 37°C for one hour. The enzyme *Dpn I* only cleaves methylated DNA. The template DNA but not the PCR product is methylated and therefore only the template DNA will be restricted.

The PCR efficiency was checked via an electrophoresis gel. If the expected band was seen on the gel, the final product was transformed into competent cells; mostly *E. coli XL10-Gold ultra* competent cells were used or, alternatively, *E. coli 5-alpha* or *10-beta* competent cells. Both the LB media and the agar plates, in and on which the cells and colonies grew, were laced with kanamycin (30 μg/ml) to select cells containing the plasmid, which contains the gene for kanamycin resistance. Four colonies were chosen and inoculated in LB media laced with kanamycin (30 μg/ml) again. A mini plasmid preparation of each batch was conducted using the *GeneAll Exprep Plasmid SV mini Kit* following the guides' manual. Afterwards the constructs were sent for sequencing (performed by *Mycrosynth* via *Sanger sequencing*). If the sequencing provided proof that the construct contained the required mutation, this construct was inoculated in LB media laced with kanamycin (30 μg/ml) and a plasmid midi preparation was made also following the guides' manual (*ZymoPure II Plasmid Midi prep Kit*). Finally, this plasmid was checked via sequencing again and the purity as well as concentration was measured via a spectral photometer (*NanoDrop OneC, Thermo Scientific*). The plasmids were diluted to a concentration of 1 μg/μl and stored at -20°C until use.

2.4 Substituted cysteine accessibility method

The substituted cysteine accessibility method (SCAM) is a common method to investigate membrane-spanning proteins. Especially amino acids that line the pore of a transport-capable protein can be tested for their accessibility to the aqueous medium. And furthermore, alterations in the protein associated with conformational changes during a transport cycle can be identified.

In a first step, a cysteine-free variant of the investigated protein has to be generated. The cysteines were mutated to alanines via *site-directed* mutagenesis as described in 2.3.1. Next the amino acid, that is to be tested for its accessibility, is mutated to cysteine resulting in a protein variant with a single cysteine. After successful expression, assembly in the plasma membrane and functionality test of the protein variant, the actual SCAM experiments could be performed. These experiments are patch-clamp measurements (cf. 2.6) with MTS reagents. MTS reagents are thiol-specific and membrane-impermeable. This allows their application from either the extracellular or intracellular side of the cell. If the cysteine residue faces the aqueous medium and is accessible to MTS compounds, it forms a disulphide bridge with the cysteine. This bond probably influences the measured signal by blocking the pore or hindering the conformational change associated with substrate transport. For this study two differently charged MTS reagents were used, the positively charged MTSET and the negatively charged MTSES. Because of their relatively short half-life, aliquots (c(MTS)=1 mM in DMSO) were frozen and freshly thawed before every measurement.

DTT is a reagent that reduces disulphide bridges. For some measurements DTT was applied after the application of the MTS reagent as it removes the formed bond between MTS and the cysteine. Thus, DTT can be used to prove the specific effect by MTSES or MTSET, respectively, as this effect is reversible.

All cysteines of the rat prestin wild type were mutated to alanines (cf. 7.1.1). Unlike rat prestin, the generation of a cysteine-free construct of zebrafish prestin was not possible. The mutation of C726 to alanine results in a dysfunctional mutant. For this reason, the zebrafish prestin base construct (WT_△Cys) still contains the cysteine at position 726 (cf. 7.1.2). This position is located in the STAS domain and, therefore, far away from the investigated parts of the protein. Furthermore, this mutant was not affected by application of MTS neither from the intracellular nor the extracellular side of the cell (cf. Figure 3.23 and Figure 3.30).

2.5 Confocal microscopy

Confocal microscopy is also called Confocal Laser Scanning Microscopy (CLSM). One of the problems with regular fluorescence microscopy is that the whole sample is illuminated by excitation light. On the one hand, this results in a faster bleaching of the fluophores and they become non-fluorescent. On the other hand, it causes scattered light. Confocal microscopy has the advantage that only a small area of the sample is illuminated at a time which minimises the scattered light. The focal points of the objective lens of the microscope generate an image where a pinhole is set and scans through the sample. Thus, the pinhole *con*jugates to the *focal* point of the lens (*confocal* pinhole).

The confocal microscope that was used in combination with *Zen* software (2009) was of the type *LSM 710 AX10 Examiner Z1* (*Zeiss*). The software *ImageJ* was used to analyse the images, especially to adjust contrast and intensity as well as to insert scaling bars.

Confocal microscopy was used to determine the cellular localisation of the fluorescently tagged prestin molecules. Images were recorded from 24 to 48 hours after transfection of the cells. The fluorophore in all recordings was GFP which was excited by an argon multiline laser at 488 nm. The objective *WPlan Apochromat 63x/1.0 M27* was used for the images. If the prestin molecules were located in the plasma membrane, a plane at the bottom of the cell was imaged.

2.6 Electrophysiology

Patch-clamp is a common technique in electrophysiology, which enables the measurement of ionic currents of an entire tissue, separated cells or single channels in membrane patches. After voltage-clamp measurements of the squid giant axon by Hodgkin and Huxley in 1952 (Hodgkin and Huxley 1952, 1952a, 1952b & 1952c), the technique was further refined by Bert Sakmann and Erwin Neher in 1976, who performed single channel recordings in frog muscle fibres (Sakmann & Neher, 1976). Performing a gigaseal was an additional innovation, which improved the signal to noise ratio and facilitated the measurement of even small currents. The principles have not changed since then and are widely the same nowadays.

A glass pipette is filled with an appropriate electrolyte solution. By placing this pipette very tight to the cell membrane, this membrane patch will be electrically isolated and the patch pipette can record currents of channels within this patch. This is possible because of an electrode within the patch pipette, which is connected to a highly sensitive differential amplifier.

There are two different techniques: voltage-clamp and current-clamp. In this study measurements were performed solely in voltage-clamp mode. In voltage-clamp configuration the voltage is kept constant at a predefined value during the whole measurement. Therefore, the membrane potential is permanently checked via a negative feedback mechanism and, if necessary, a current is injected into the cell to compensate for possible changes in membrane potential.

There are also different configurations, which can be chosen depending on the question to be answered, namely cell-attached, whole cell, inside-out and outside-out configuration. For this study measurements were mainly performed in whole cell configuration and only a few additional measurements were performed in outside-out configuration.

2.6.1 Nonlinear capacitance and transport currents

An inverted microscope (*Leica DMI 3000B*) was used for the scanning of the cells and a fluorescence light source (*Leica EL6000*) enabled the identification of cells with prestin localised in the membrane. Furthermore, an amplifier (*HEKA EPC-10*) and two micromanipulators (*Luigs & Neumann*) were part of the setup. Borosilicate capillaries (*GB100T-8P or GB100TF-8P, Science Products*) with a pipette resistance of 2-4 MΩ were filled with intracellular solution and put on a chlorinated silver wire, which connects the intracellular part of the cell and the amplifier. After forming a gigaseal (≥1 GΩ) and rupture of the cell membrane, measurements were only performed with a serial resistance under 10 MΩ. Measurements were recorded using the *Patchmaster Software v2x32* (*HEKA*) and performed using the voltage-clamp mode and at room temperature (~22°C).

A sinusoidal stimulus was superimposed on a voltage ramp and in the case of the mammalian rat prestin the membrane capacitance was measured. As the capacitance is not a constant function of voltage, it is referred to as nonlinear capacitance (NLC). The standard protocol was a sinusoidal stimulus of 2 kHz on a voltage ramp from -120 to +120 mV achieved by the lock-in function of Patchmaster. The stimulus was applied every 3 s for 300 ms with a holding potential of -20 mV in between. When the voltage ramp was adjusted to more positive or negative values, it is mentioned separately.

The non-mammalian prestin orthologues produce electrogenic anion transport currents. These currents were measured in response to voltage ramps from -120 mV to +120 mV (every 3 s with a duration of 300 ms). Depending on whether the divalent anions were applied from the intra- or extracellular side of the cell, the holding potential between the voltage ramps was -60 or +60 mV, respectively, to minimise background currents.

Extracellular solutions

The same extracellular solution was used for the measurements of NLC and transport currents. All extracellular solutions were adjusted to pH 7.4 using NaOH (1M) solution. The osmolarity was between 305 and 310 mOsm/kg.

Table 2.2: Ingredients and composition of the standard extracellular solution.

Substance	Molecular weight (g/mol)	Applied amount of substance (mM)
KCl	74.55	5.8
NaCl	58.44	144
$MgCl_2$	1	0.9
$CaCl_2$	1	1.3
NaH_2PO_4	137.99	0.7
D-(+)-Glucose	198.17	5.6
HEPES	238.30	10

In case of oxalate offered from the extracellular side, the following solutions were used.

Table 2.3: Ingredients and composition of the extracellular solution for transport measurements with low chloride concentration and without oxalate.

Substance	Molecular weight (g/mol)	Applied amount of substance (mM)
NaCl	58.44	10
HEPES	238.30	10
Sodium-L-Aspartate	173.10	150

Table 2.4: Ingredients and composition of the extracellular solution for transport measurements with low chloride concentration and with oxalate (10 mM).

Substance	Molecular weight (g/mol)	Applied amount of substance (mM)
NaCl	58.44	10
HEPES	238.30	10
Sodium-L-Aspartate	173.10	140
Oxalate dihydrate	126.07	10

If transport currents delivered only small signals the solution was adjusted to 50 mM oxalate dihydrate and 90 mM sodium-L-aspartate.

Intracellular solutions

The standard intracellular solution was used for measurements of NLC and transport measurements with extracellularly applied oxalate. All intracellular solutions were

adjusted to pH 7.4 with CsOH (1M) solution. The osmolarity was between 285 and 295 mOsm/kg.

Table 2.5: Ingredients and composition of the standard intracellular solution.

Substance	Molecular weight (g/mol)	Applied amount of substance (mM)
CsCl	168.36	160
K_2EGTA	380.35	1
HEPES	238.30	1

Table 2.6: Ingredients and composition of the intracellular solution for measurements of transport currents with intracellularly applied oxalate and low chloride concentration.

Substance	Molecular weight (g/mol)	Applied amount of substance (mM)
CsCl	168.36	10
K_2EGTA	380.35	1
HEPES	238.30	1
Sodium-L-Aspartate	173.10	140
Oxalate dihydrate	126.07	10

Some of the zebrafish mutants produced only small transport currents. To ensure that transport currents were comparable for SCAM measurements, the intracellular solution was adjusted to the maximum amount of oxalate with standard osmolarity, so that the composition was 106 mM oxalate dihydrate and 10 mM Hepes. The intracellular solution with high concentration of oxalate was used for most transport measurements except of the measurement of zebrafish prestin wild type.

2.7 Data analysis

Data were analysed using *Igor Pro* (6.03A2) as well as *Excel* (*Microsoft Office 2008*). The recorded data of NLC and transport current measurements, respectively, were imported into *Igor Pro*. The evaluation of transport currents was performed using the procedure files provided by *WaveMetrics.* The simplest model of prestin is a two-state model where the charge can be switched between two conditions. The data points collected for the nonlinear capacitance were fitted in a two-state Boltzmann function of a first-order derivative:

$$C_M(V_M) = C_{lin} + Q_{max} / (\alpha\, e^{(V-V1/2)/\alpha} (1 + e^{-(V-V1/2)/\alpha})^2)$$

C_M: membrane capacitance

V_M: membrane potential

C_{lin}: linear (passive) membrane capacitance

Q_{max}: maximum voltage-sensor charge moved through the membrane electric field

α: slope factor of the voltage dependence

$V_{1/2}$: voltage at half-maximal charge transfer

The amplitude of the NLC was quantified as peak NLC at half-maximal charge transfer as follows:

$$NLC_{max} = C_M (V_{1/2}) - C_{lin}$$

In the figures, graphs with normalised NLC measurements will be shown where the linear capacitance is subtracted from the membrane capacitance at the $V_{1/2}$. These normalised NLC traces were plotted as a function of membrane potential.

The mean value of either the NLC, the $V_{1/2}$ or the transport current was calculated in *Igor Pro* but tests of significances of the obtained data were done using *Excel*. First, the mean value (a_1) of five to ten traces from one measurement at a single condition (e.g. before application of MTS reagents) were determined, and, second, compared with the mean value (a_2) of another condition (e.g. during application of MTS reagents) within the same measurement. To quantify changes in the amplitude of the NLC or the transport current, the ratio between a_1 and a_2 was calculated. Thus, changes in the NLC were stated as percentage values. In terms of the $V_{1/2}$, the difference (a_2-a_1) was determined as a parameter to describe changes in the voltage-dependent behaviour. Unless stated otherwise, there were five independent measurements analysed for each condition. Again, an average value of these five calculated changes as well as the variation of the values via the standard error of the mean (SEM) were determined. The comparison of different conditions was made via the Student`s t-test. Statistical significance was defined as follows: $p>0.05$ as n.s.; $p\leq0.05$ as *; $p\leq0.01$ as **; $p\leq0.001$ as ***.

3 Results

3.1 Functional characterisation of cysteine substitution mutants

The prestin constructs investigated for the cysteine accessibility study are based on a cysteine-free background where the cysteines were mutated to alanines (cf. 7.1). These rat and zebrafish constructs served as the control for MTS background activity. In the regions predicted to be part of the anion translocation pathway and the anion-binding site single cysteines were introduced on the cysteine-free background via *site-directed* mutagenesis (cf. 2.3.1). In a first step, the constructs generated for the cysteine accessibility scanning were studied for retained functionality. To allow for functional investigation, each prestin mutant needs to be expressed and targeted to the plasma membrane. All constructs were cloned into the pEGFP-N1 vector. The prestin proteins were C-terminal GFP-tagged, so that GFP served as the reporter for a successful expression and localisation of prestin. These two aspects were tested via confocal microscopy. To check for membrane localisation the bottom layer of the cells was focused. The controls (WT_△Cys) were targeted to the plasma membrane and showed a characteristic clustered pattern like rat and zebrafish prestin wild type proteins. The following figures (Figure 3.1 - Figure 3.3) show representative confocal images of each mutant to be investigated in the SCAM experiments.

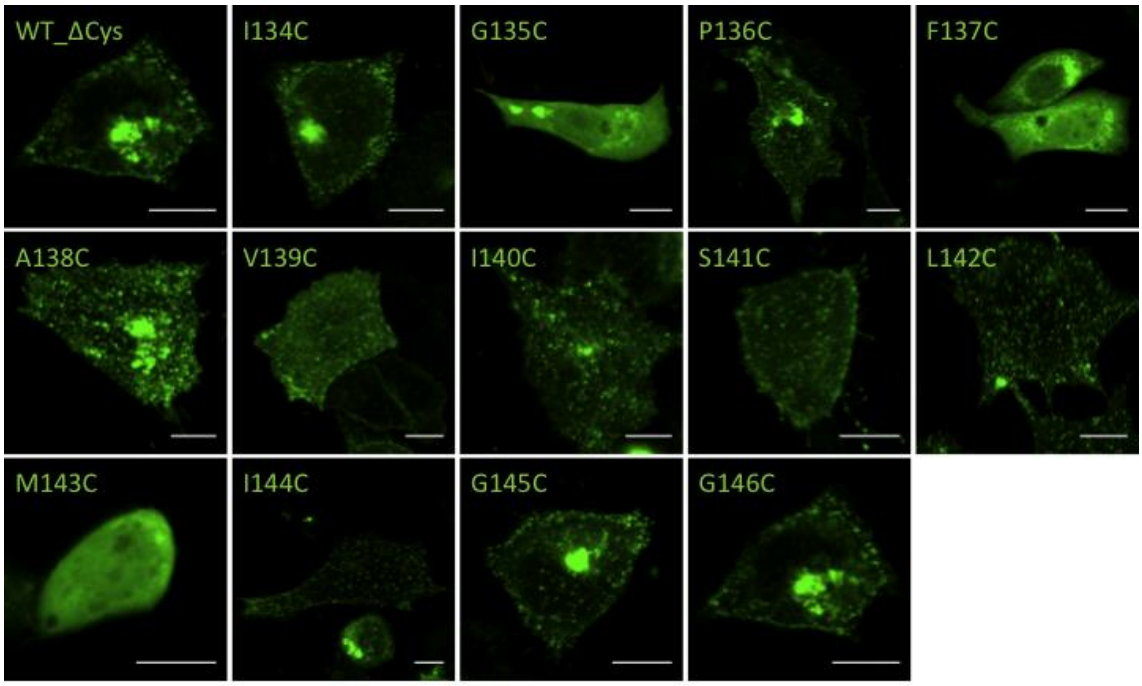

Figure 3.1: Confocal images of CHO cells transiently transfected with rat prestin constructs used for SCAM experiments in TM 3. WT_△Cys was the control of rat prestin with all cysteines mutated to alanines. All other constructs were based on the control and contain the named mutation in addition. All prestin constructs were GFP-tagged at the C-terminus. Scale bars: 10 μm.

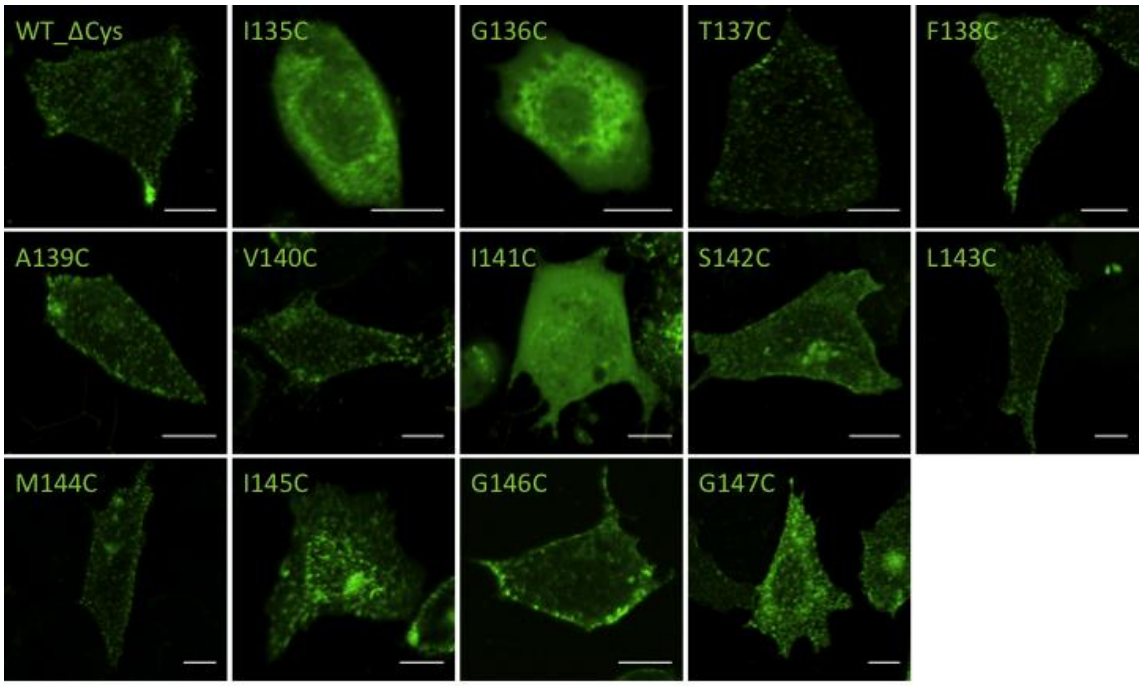

Figure 3.2: Confocal images of CHO cells transiently transfected with zebrafish prestin constructs used for SCAM experiments in TM 3. WT_△Cys was the control of zebrafish prestin with nearly all cysteines mutated to alanines (cf. 7.1.2). All other constructs were based on the control and contain the named mutation in addition. All prestin constructs were GFP-tagged at the C-terminus. Scale bars: 10 μm.

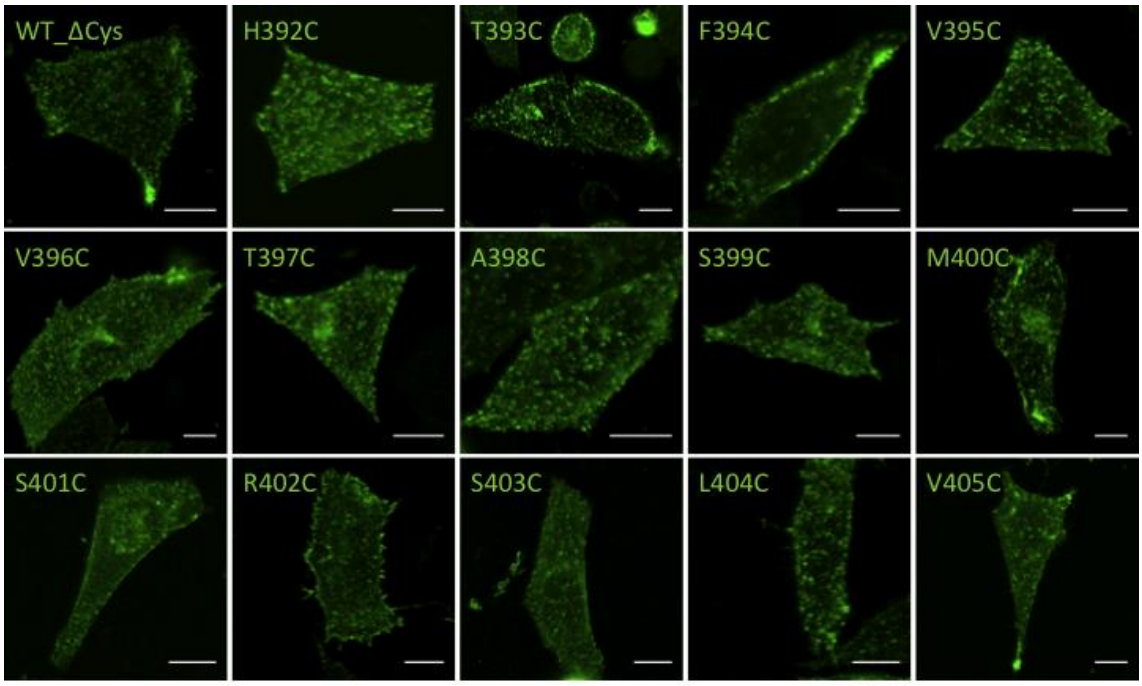

Figure 3.3: Confocal images of CHO cells transiently transfected with zebrafish prestin constructs used for SCAM experiments in TM 10. WT_△Cys was the control of zebrafish prestin with nearly all cysteines mutated to alanines (cf. 7.1.2). All other constructs were based on the control and contain the named mutation in addition. All prestin constructs were GFP-tagged at the C-terminus. Scale bars: 10 μm.

Even though the expression levels of the individual mutants differed considerably in terms of intensity and the formation of clustered structures, only those mutants that displayed a clear cytosolic localisation while lacking detectable (i.e. strong) membrane localisation were excluded from further experiments. The localisation patterns of these mutants were checked for at least two independent transfections, which revealed consistent cytosolic localisation in each replicate. According to these specifications all constructs of zebrafish prestin with mutations within transmembrane domain 10 in a cysteine-free background featured membrane targeted prestin, but the following mutants could not be examined by the accessibility experiments:

- Rat prestin with the following mutations within transmembrane domain 3 in a cysteine-free background: G135C, F137C and M143C.

- Zebrafish prestin with the following mutations within transmembrane domain 3 in a cysteine-free background: I135C, G136C and I141C.

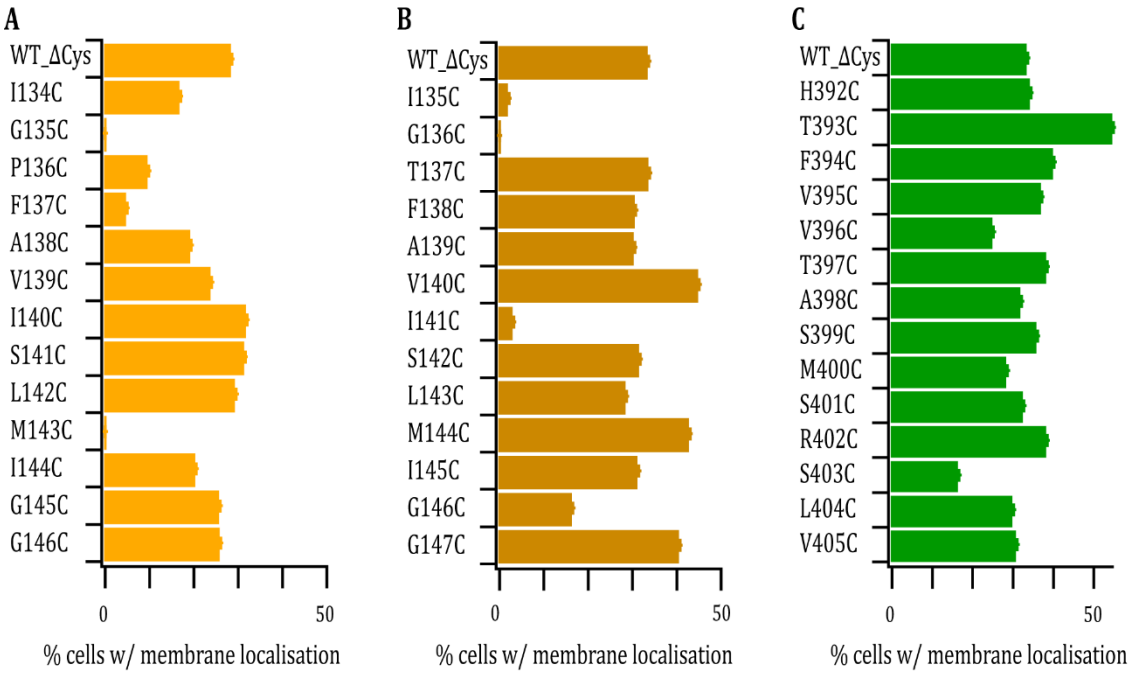

Figure 3.4: Percentage of CHO cells with prestin located in the cell membrane. WT_△Cys was the control of rat with all cysteines mutated to alanines or zebrafish prestin with nearly all cysteines mutated to alanines (cf. 7.1.2). **A**: Rat prestin constructs with cysteine mutations within TM 3. **B**: Zebrafish prestin constructs with cysteine mutations within TM 3. **C**: Zebrafish prestin constructs with cysteine mutations within TM 10.

In addition, transfected cells were counted and the percentage of cells with fluorescence in the plasma membrane was quantified. The counting was performed with two independent transfections for each mutant at the patch setup (cf. 2.6). Each construct was transfected

onto cells seeded into a petri dish with four coverslips. Five spots on each coverslip were chosen randomly and the number of fluorescent cells as well as the number of cells with prestin in the membrane was determined. The results are shown in Figure 3.4. There is a relatively wide range in the percentage of cells with membrane localisation. The exact values for constructs of rat prestin with mutations within transmembrane domain 3 and missing membrane localisation were G135C: 0 %, F137C: 4.9 ± 0.0 % and M143C: 0 %. The values for constructs of zebrafish prestin with mutations within transmembrane domain 3 without prestin targeted to the membrane were I135C: 2.1 ± 0.0 %, G136C: 0 % and I141C: 3.2 ± 0.0 %.

Next, all mutants that targeted properly were examined for retained function by electrophysiology. In the case of rat prestin mutants, NLC was recorded, and in the case of zebrafish prestin mutants, transport currents in the presence of the divalent transport substrate oxalate were measured.

Figure 3.5 shows representative measurements of the NLC of the rat prestin constructs with mutations within transmembrane domain 3. It displays single representative traces of a standard measurement with standard solutions and without the application of MTS reagents.

Rat prestin WT_△Cys delivered a reliable signal (peak NLC: 617.04 ± 153.08 fF; $V_{1/2}$: -43.47 ± 7.00 mV; n=5). Even though the NLC peak amplitude was moderately smaller and the $V_{1/2}$ was shifted to more positive values the signal was comparable to the signal of rat prestin wild type (peak NLC: 878.16 ± 64.01 fF; $V_{1/2}$: -81.39 ± 10.35 mV; n=5; not shown).

The NLC peak amplitude and the position of the $V_{1/2}$ varied between the individual mutants (cf. Table 3.1). Despite this fact, eight of the ten mutants produced robust signals, sufficient for subsequent SCAM experiments. In the case of the mutant A138C, a slight increase of the NLC trace in direction of depolarisation was observed, but also the extension of the voltage ramps up to +200 mV (not shown) did not result in a reliable NLC signal. Therefore, this mutant was classified as dysfunctional. Furthermore, the mutant G164C was also dysfunctional.

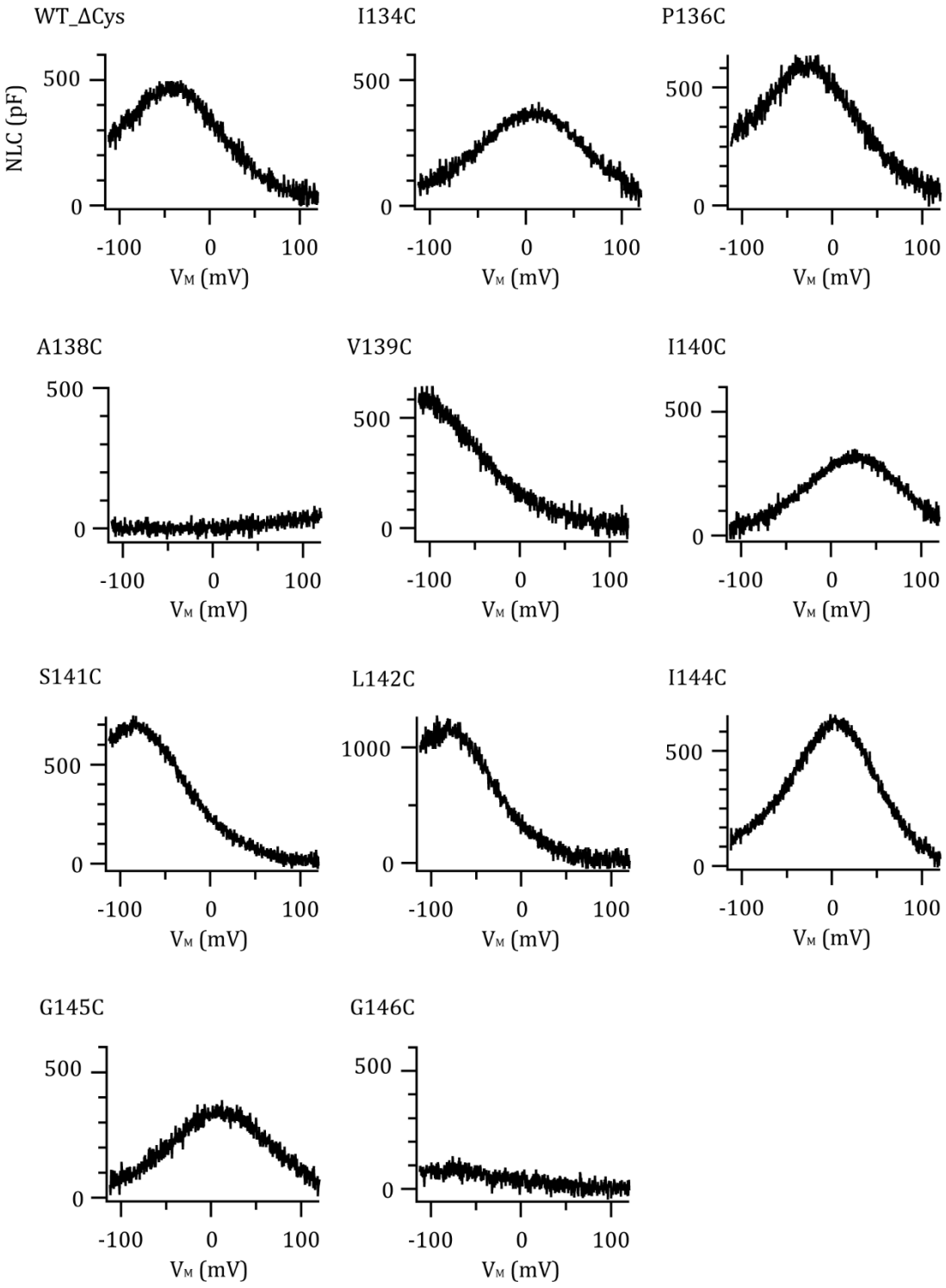

Figure 3.5: Basal function of the rat prestin constructs with mutations within TM 3. Shown are representative NLC signals of the basic construct (WT_△Cys) and all mutants with predominant membrane localisation of prestin. The traces were measured under standard conditions.

The following Table 3.1 shows mean values of NLC signals and $V_{1/2}$ of the rat prestin constructs with mutations within transmembrane domain 3, which had a strong membrane localisation and showed proper signals.

Table 3.1: Average values of the NLC and $V_{1/2}$ of the rat prestin constructs with mutations within TM 3. The table shows mean values with SEM for five measurements (n=5) under standard conditions.

	NLC amplitude size (fF)		$V_{1/2}$ (mV)	
	mean	SEM	mean	SEM
WT_△Cys	617.04	153.08	-43.47	7.00
I134C	301.37	18.48	0.64	8.31
P136C	363.83	67.36	-27.03	10.13
V139C	363.42	60.53	-111.78	2.41
I140C	302.81	24.66	11.46	7.75
S141C	722.17	168.48	-94.90	2.95
L142C	522.07	132.13	-77.94	7.00
I144C	351.91	70.75	-8.47	5.24
G145C	325.00	36.36	-13.09	10.66

The basal functionality of the zebrafish prestin constructs was also tested. The transport function of those mutants with retained wild type-like strong membrane localisation was examined. Figure 3.6 shows representative traces of transport currents measured in zebrafish prestin constructs with mutations within transmembrane domain 3 under standard conditions. Oxalate (106 mM) was provided from the inside of the cell via the patch pipette, whereas the extracellular bath solution contained chloride (cf. Table 2.2). Under these conditions, zebrafish prestin mediates 1:1 chloride/oxalate exchange, which is electrogenic and can thus be measured as an ionic current in voltage-clamp experiments. The transport currents were measured in response to voltage ramps from -120 mV to +120 mV. Thus, the holding potential between the voltage ramps was set to -60 mV to minimise background currents and initiate a transport current only during the voltage ramps.

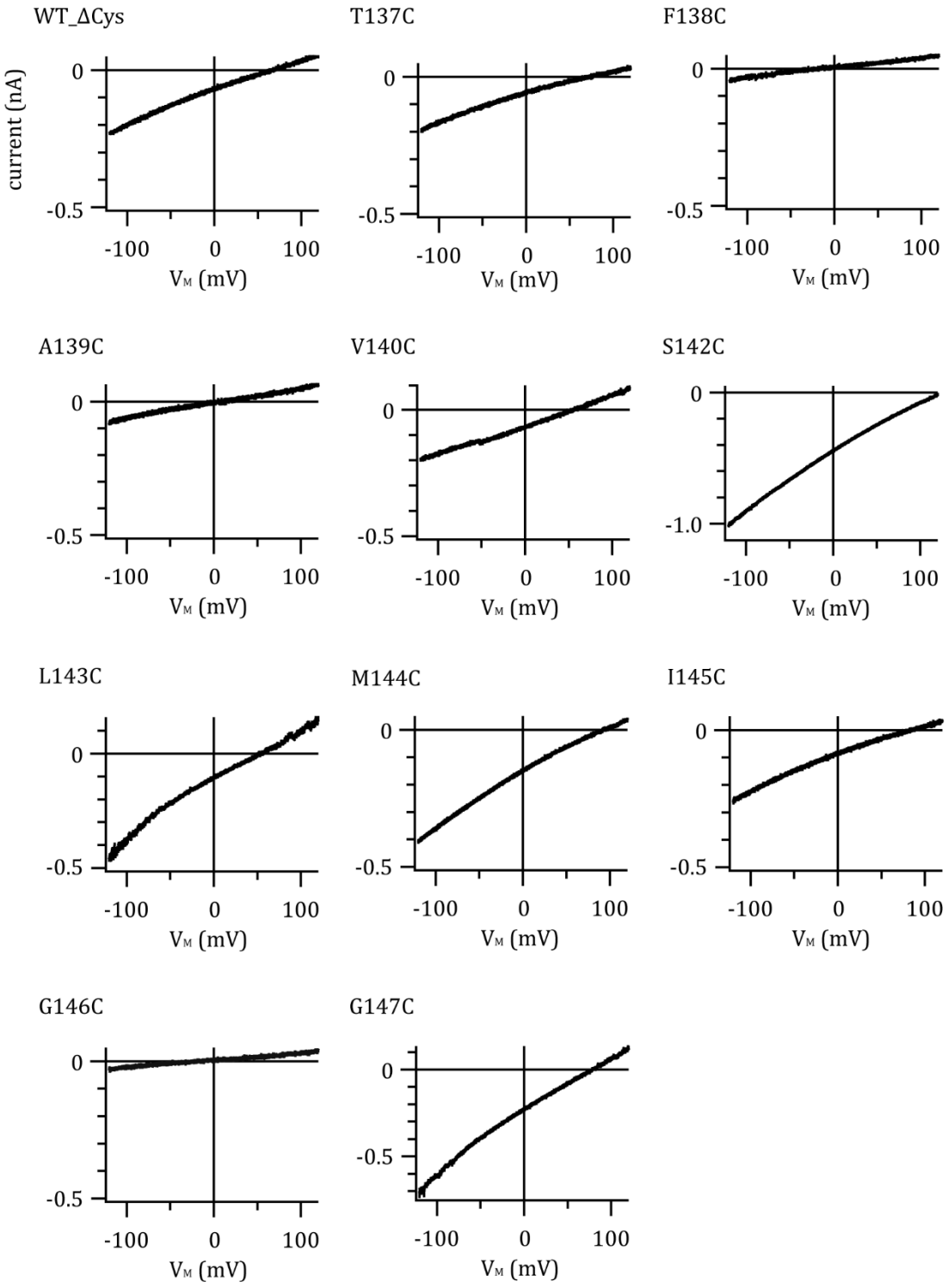

Figure 3.6: Basal function of the zebrafish prestin constructs with mutations within TM 3. Shown are representative transport currents of the basic construct (WT_△Cys) and all mutants with predominant membrane localisation of prestin. The traces were measured under standard conditions.

Despite the high concentration of oxalate, three mutants did not display detectable transport currents: F138C, A139C and G146C. The small currents reflect leakage currents also observed in non-transfected cells. This is also confirmed by the slightly negatively

shifted reversal potential (to -20 mV), which is incompatible with anion exchange (Cl:oxalate) under the chosen substrate gradients. Since endogenous leak currents are minimal at 0 mV, for quantification of transport currents, the (inward) currents at 0 mV were analysed. Therefore, no leakage correction was necessary. In contrast to the dysfunctional constructs, the mutants S142C and T137C exhibited particularly large currents. Notwithstanding the differences in the transport current, seven of the ten mutants with a single cysteine in transmembrane domain 3 were found suitable for subsequent accessibility measurements with the MTS reagents, as their transport currents were large enough to be identified unequivocally (cf. Figure 3.6 and Table 3.2).

Table 3.2: Average values of the transport currents of the zebrafish prestin constructs with mutations within TM 3. The table shows mean values with SEM for five measurements (n=5) under standard conditions.

	transport current (pA) at 0 mV	
	mean	SEM
WT_△Cys	-50.57	20.90
T137C	-238.52	39.15
V140C	-52.42	8.84
S142C	-293.79	77.88
L143C	-74.58	28.01
M144C	-235.83	73.54
I145C	-123.54	20.28
G147C	-126.96	35.15

Comparable to the previous graphs, Figure 3.7 shows representative transport currents of zebrafish prestin mutants with an exchange of an amino acid to cysteine in transmembrane domain 10. Moreover, these mutants differ with respect to their transport currents (cf. Table 3.3). Although the mutants T393C, F394C and V395C showed appropriate membrane targeting, they were not further examined because they are predicted to be located in the bulk of the protein and are therefore very unlikely to be accessible to the MTS compounds. In addition, the position H392 was analysed because the structurally homologous position of rat prestin (Q389) was previously shown to be extracellularly accessible (Gorbunov et al., 2014). No transport currents were detectable in two of the eleven remaining mutants: S399C and R402C (Figure 3.7).

Table 3.3 shows mean values of transport currents of the zebrafish prestin constructs with a mutation within transmembrane domain 10, which had a strong membrane localisation and showed proper signals.

Table 3.3: Average values of the transport currents of the zebrafish prestin constructs with mutations within TM 10. The table shows mean values with SEM for five measurements (n=5) under standard conditions.

	transport current (pA) at 0 mV	
	mean	SEM
WT_△Cys	-50.57	20.90
H392C	-147.09	66.91
V396C	-99.25	62.59
T397C	-274.39	45.23
A398C	-228.30	86.21
M400C	-136.43	39.48
S401C	-39.64	7.64
S403C	-109.96	19.28
L404C	-198.64	6.69
V405C	-48.21	14.10

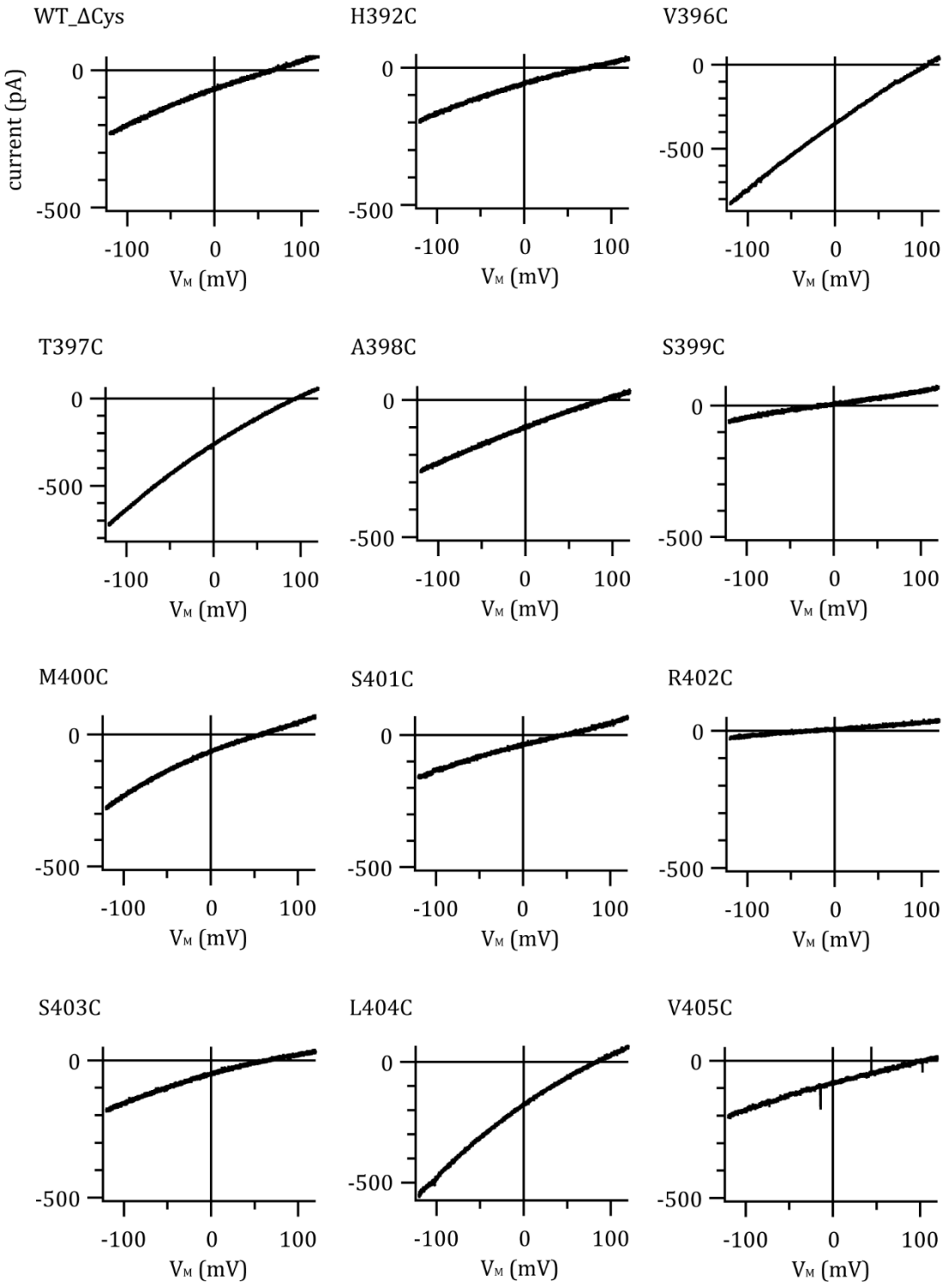

Figure 3.7: Basal function of the zebrafish prestin constructs with mutations within TM 10. Shown are representative transport currents of the basic construct (WT_△Cys) and all mutants with predominant membrane localisation of prestin. The traces were measured under standard conditions.

3.2 SCAM of rat prestin

3.2.1 Extracellular accessibility of positions within TM 3 in rat prestin

The following figures show representative measurements for each condition, i.e. a control measurement without application of MTS reagents (black), as well as measurements with extracellularly applied MTSES (red) or MTET (blue), respectively. The final concentration of the MTS reagents was 1 mM or less. Covalent modification by the MTS reagents can be deduced from any irreversible effect of application on the functional readout, either a decrease in the NLC peak amplitude and/or a shift of the $V_{1/2}$. Such changes induced by the application of MTS reagents thus indicate solute accessibility of the introduced cysteine and in consequence of this amino acid position.

Figure 3.8 shows two exemplary constructs of rat prestin. As expected, the mutant WT_△Cys was entirely insensitive to the application of MTS reagents. The mutant R236C was not part of the scanning of positions within transmembrane domain 3, but served as positive control that was sensitive to the application of MTSES as well as MTSET as can be seen by shifts of the $V_{1/2}$ upon MTS application (cf. Gorbunov et al., 2014).

In Figure 3.9 changes in the NLC peak amplitude can be seen, whereas Figure 3.10 shows shifts of the $V_{1/2}$ in response to the application of MTS reagents. All constructs of rat prestin with mutations within transmembrane 3 are shown, that exhibited predominant membrane localisation and strong NLC signals.

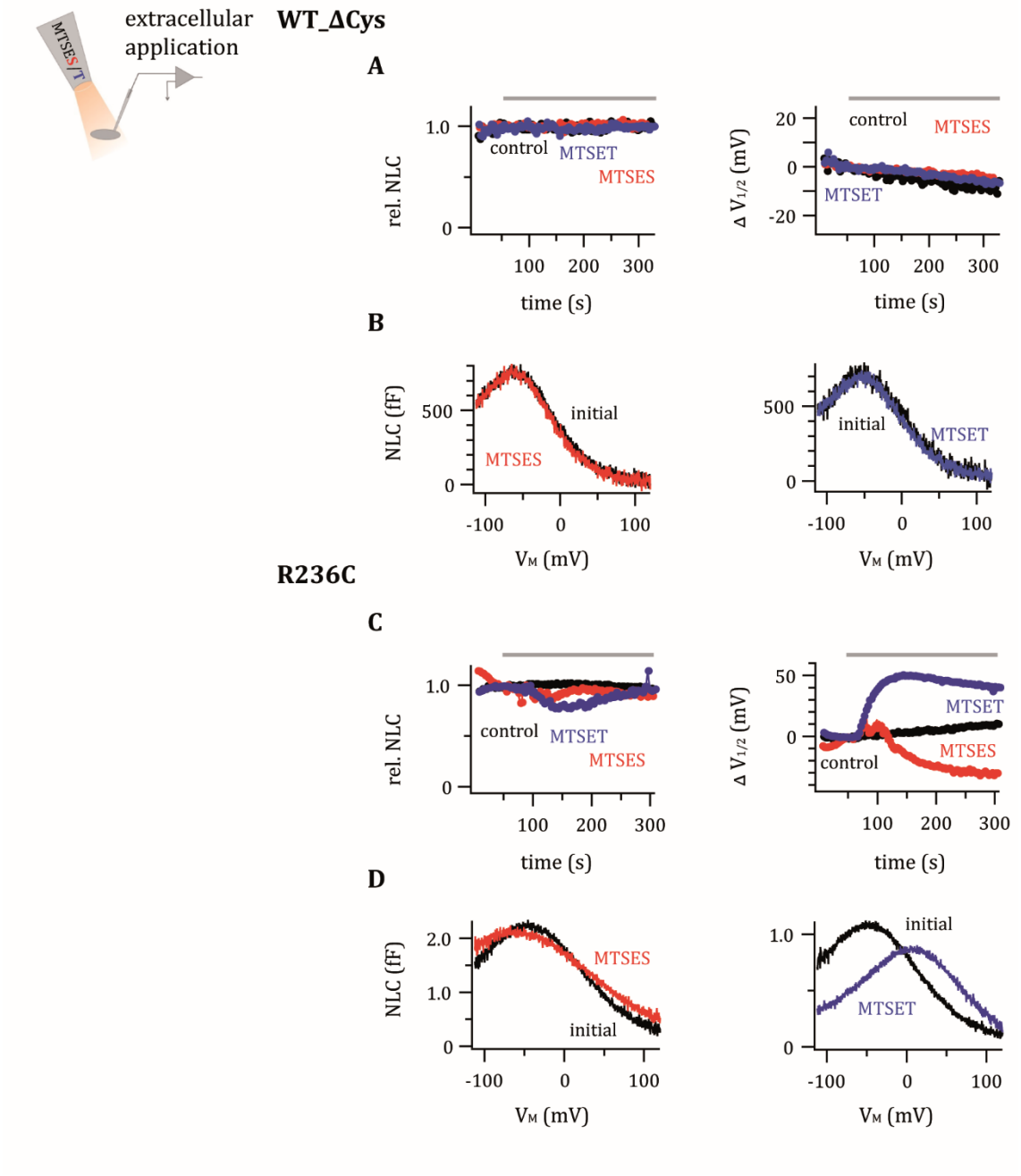

Figure 3.8: The effects of extracellular MTS application on rat prestin constructs. A+B: WT_△Cys. **A:** Normalised NLC traces and shifts of the $V_{1/2}$. **B:** Shown are single traces from the upper graphs: the initial trace (black) is a trace before the application of the MTS reagent was started and the red (MTSES) and blue (MTSET) traces are single representative traces from a time point during the MTS application. **C+D:** The mutant R236C is shown as example for an extracellularly accessible position (cf. Gorbunov et al., 2014). **C:** The two graphs are representative normalised traces of the NLC and the $V_{1/2}$ of the mutant R236C. **D:** Shown are single traces from the upper graphs: the initial trace (black) is a trace before the application of the MTS reagent was started and the red (MTSES) and blue (MTSET) traces are single representative traces from a time point during the MTS application with a fully established effect. **A+C:** The grey bars indicate the start and end points of the application of the MTS reagents.

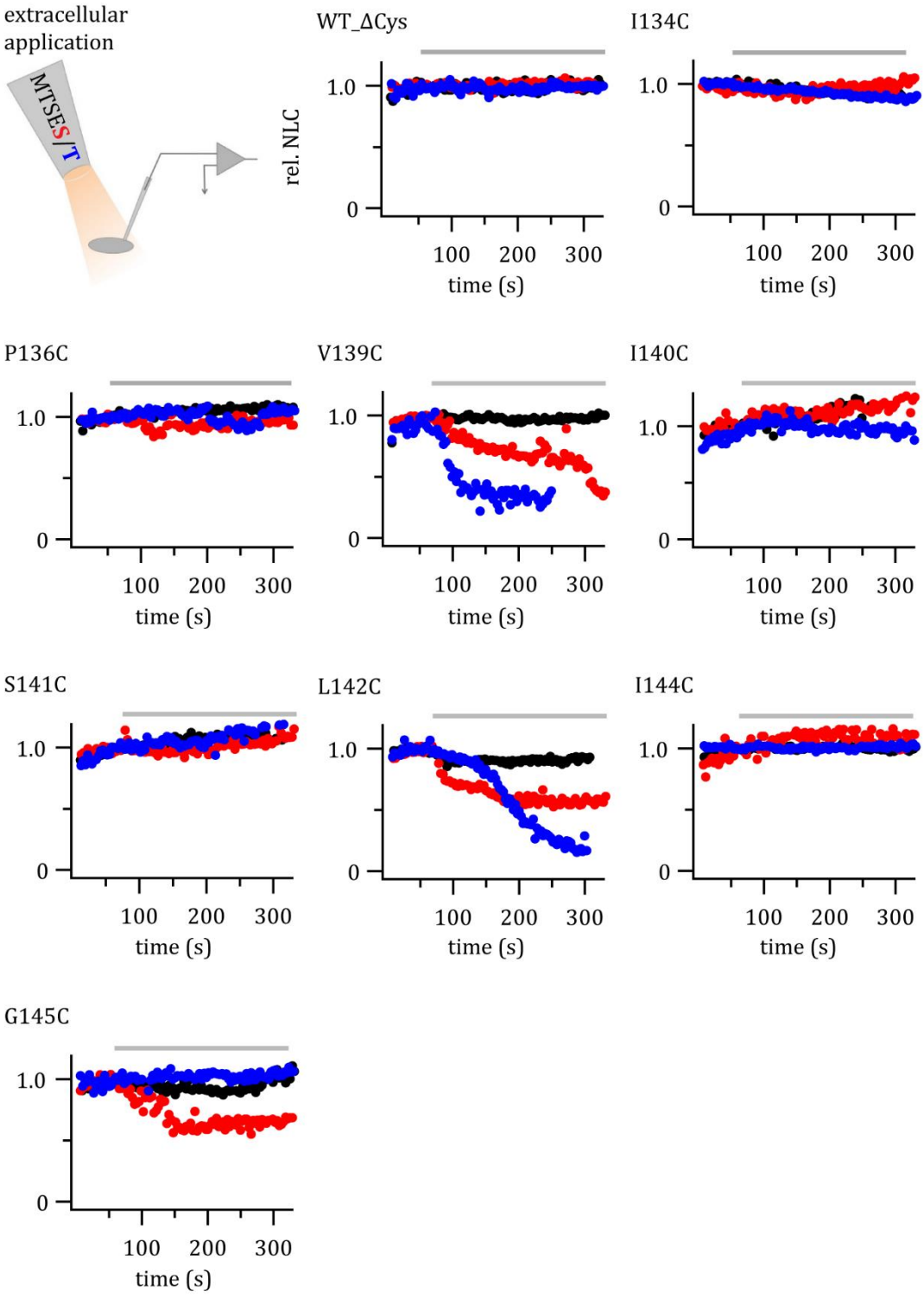

Figure 3.9: The effects of extracellularly applied MTS reagents on the NLC peak amplitude of rat prestin constructs with mutations within TM 3. WT_△Cys was the basic construct with all cysteines mutated to alanines. All traces show a representative capacitance measurement and were normalised. In black: a control measurement without application of MTS reagents. In red: a measurement with extracellularly applied MTSES. In blue: a measurement with extracellularly applied MTSET. The grey bars indicate the start and end points of the application of the MTS reagents.

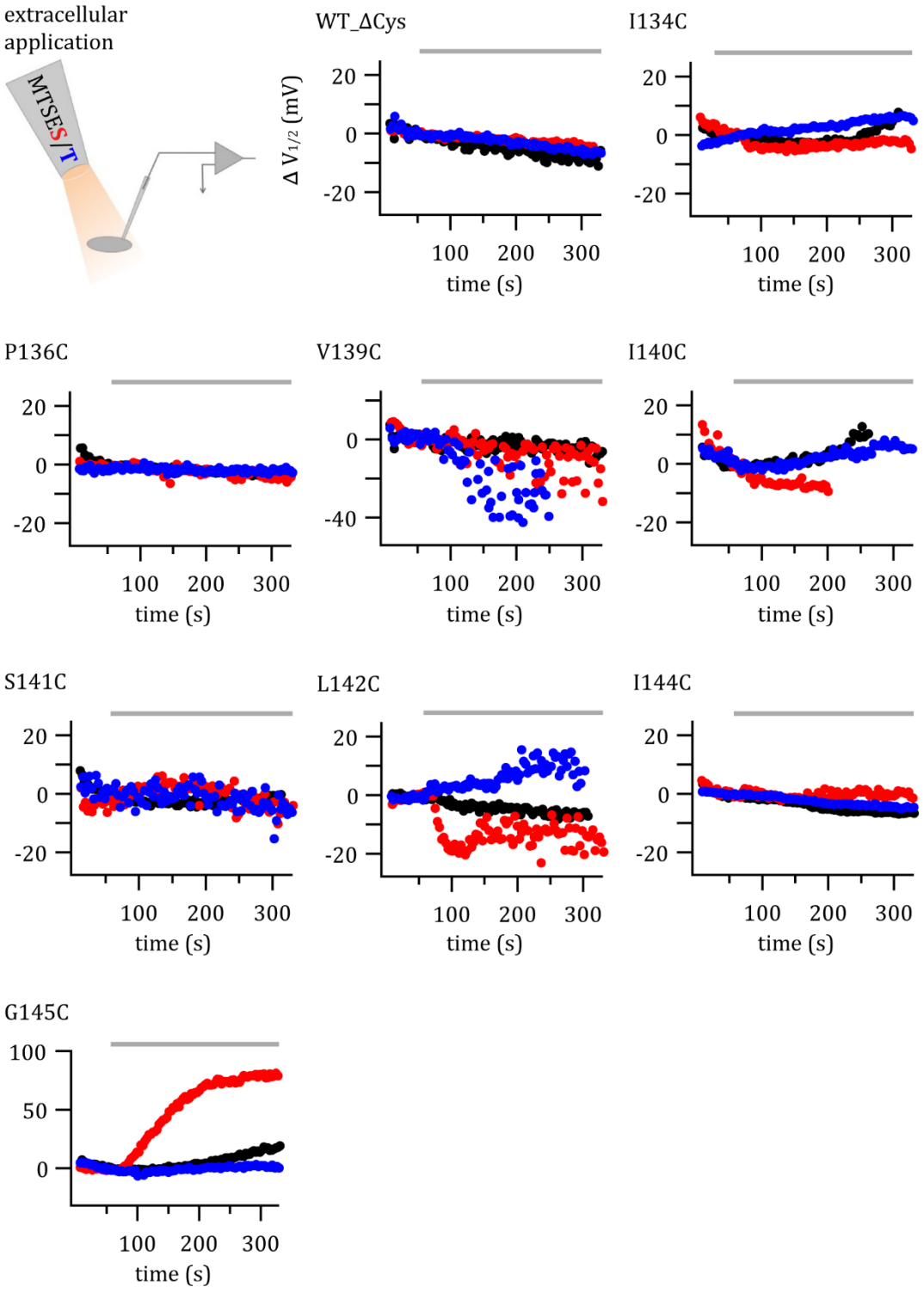

Figure 3.10: The effects of extracellularly applied MTS reagents on the $V_{1/2}$ of the rat prestin constructs with mutations within TM 3. WT_△Cys was the basic construct with all cysteines mutated to alanines. All traces show the $V_{1/2}$ of a representative measurement and were normalised. In black: a control measurement without application of MTS reagents. In red: a measurement with extracellularly applied MTSES. In blue: a measurement with extracellularly applied MTSET. The grey bars indicate the start and end points of the application of the MTS reagents.

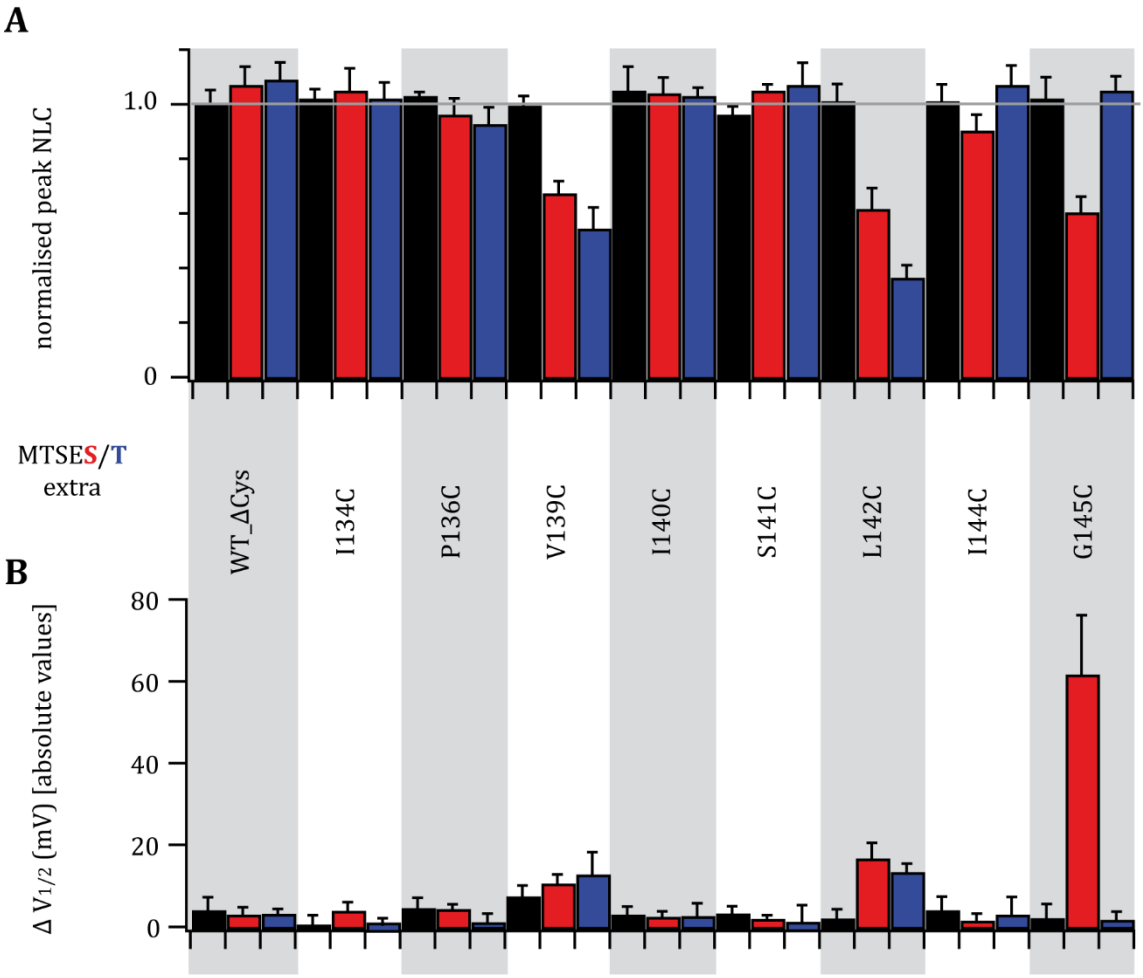

Figure 3.11: Summary of the effects of extracellularly applied MTS on rat prestin constructs with mutations within TM 3. Bars represent the mean of five measurements (n=5) ± SEM. Black bars are the control measurements without MTS application, red bars are measurements with MTSES application and blue bars are measurements with MTSET application. **A:** The bar diagram shows the changes of the normalised NLC peak amplitude upon extracellular MTS application. **B:** The bar diagram shows the changes of the $V_{1/2}$ upon extracellular MTS application. Absolute values of the changes of the $V_{1/2}$ are shown.

Among all eight functional cysteine mutants, only three (V139C, L142C and G145C) were sensitive to extracellular MTS application as indicated by changes in NLC amplitude and/or by shifts of $V_{1/2}$ (cf. Figure 3.11) and were thus classified as accessible to extracellular solutes. Detailed effects of MTS reagents on these three mutants are given below.

V139C was modified by application of MTSES and MTSET as can be seen by a decrease in the NLC peak amplitude combined with a shift of the $V_{1/2}$ to more negative values. The effect was significant for both applied MTS reagents. The following Figure 3.12 depicts cysteine accessibility of the mutant V139C expanded for statistics and representative traces before and after application of the MTS reagents. The NLC decreased upon application of MTS, to 67.3 ± 4.6 % for MTSES and 54.4 ± 7.8 % for MTSET. Shifts of the $V_{1/2}$ were found in the hyperpolarised direction, on average -10.6 ± 2.2 mV in response to MTSES and -12.8 ± 5.5 mV in response to MTSET. The statistics were performed for five measurements under

each condition. The effects on the NLC amplitude peak size and shifts of the $V_{1/2}$ were significant for both reagents.

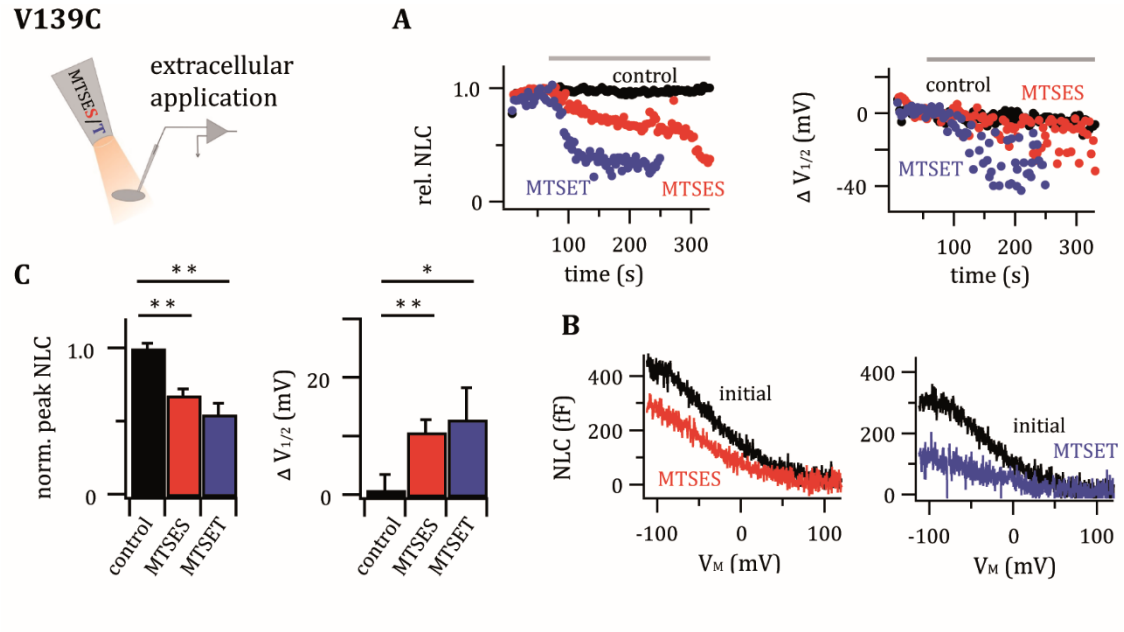

Figure 3.12: The effects of extracellular MTS application on rat prestin V139C. A: The upper two graphs of the normalised NLC and shifts of the $V_{1/2}$ are taken from Figure 3.9 and Figure 3.10. **B:** The lower two graphs are single traces from the upper graphs: the initial trace (black) is a trace before the application of the MTS reagent was started and the red (MTSES) and blue (MTSET) traces are single representative traces from a time point during the MTS application with a fully established effect. **C:** The bar diagram shows the average effect based on five measurements (n=5) with SEM for changes in the NLC peak amplitude as normalised values and changes in the $V_{1/2}$ are presented as absolute values.

Another mutant in rat prestin that was accessible to MTS reagents from the extracellular side was L142C (cf. Figure 3.13). The effect was more pronounced for MTSET as shown by a decrease in the NLC peak amplitude (36.4 ± 4.7 %) combined with a slight shift of the $V_{1/2}$ to more positive values (+13.4 ± 2.1 mV). The effect of MTSES application was more moderate and can mainly be seen as a decrease in the NLC peak amplitude (61.6 ± 7.7 %). The $V_{1/2}$ shifted to more negative values in response to the application of MTSES (-16.7 ± 3.8 mV).

The third extracellularly accessible mutant in rat prestin was G145C. The effect was only observed with MTSES, whereas there was no significant effect of MTSET. There was a strong shift of the $V_{1/2}$ of 61.7 ± 14.5 mV combined with a decrease in the NLC amplitude to 60.4 ± 5.7 % upon MTSES application. Representative traces and bar diagrams with the statistics are shown in Figure 3.14.

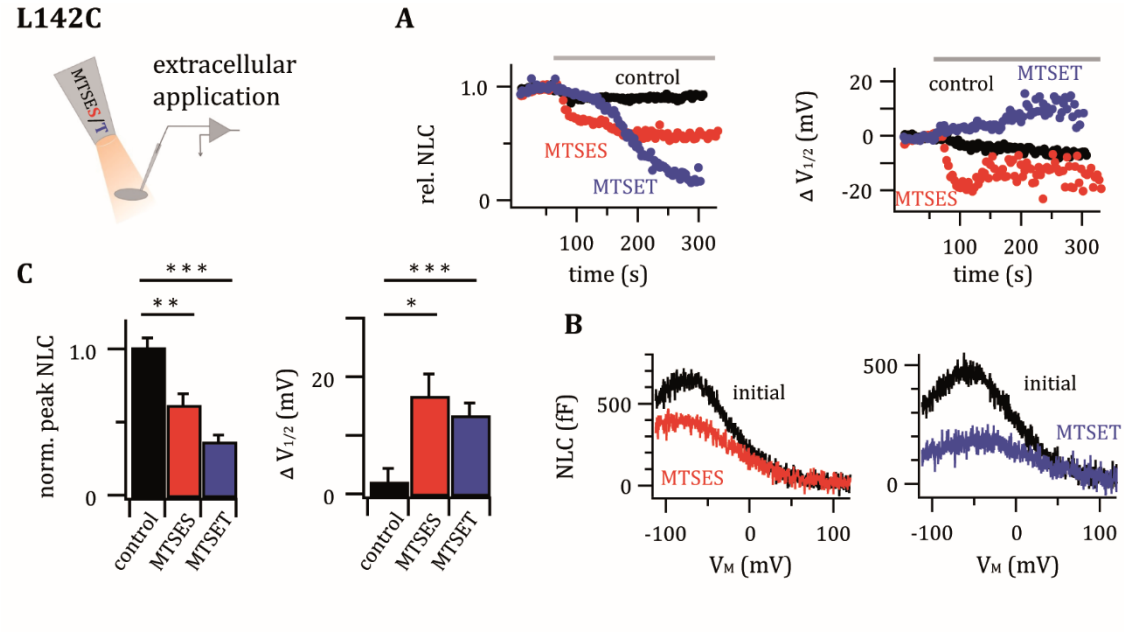

Figure 3.13: The effects of extracellular MTS application on rat prestin L142C. A: The upper two graphs of the normalised NLC and shifts of the $V_{1/2}$ are taken from Figure 3.9 and Figure 3.10. **B:** The lower two graphs are single traces from the upper graphs: the initial trace (black) is a trace before the application of the MTS reagent was started and the red (MTSES) and blue (MTSET) traces are single representative traces from a time point during the MTS application with a fully established effect. **C** The bar diagram shows the average effect based on five measurements (n=5) with SEM for changes in the NLC peak amplitude as normalised values and changes in the $V_{1/2}$ are presented as absolute values.

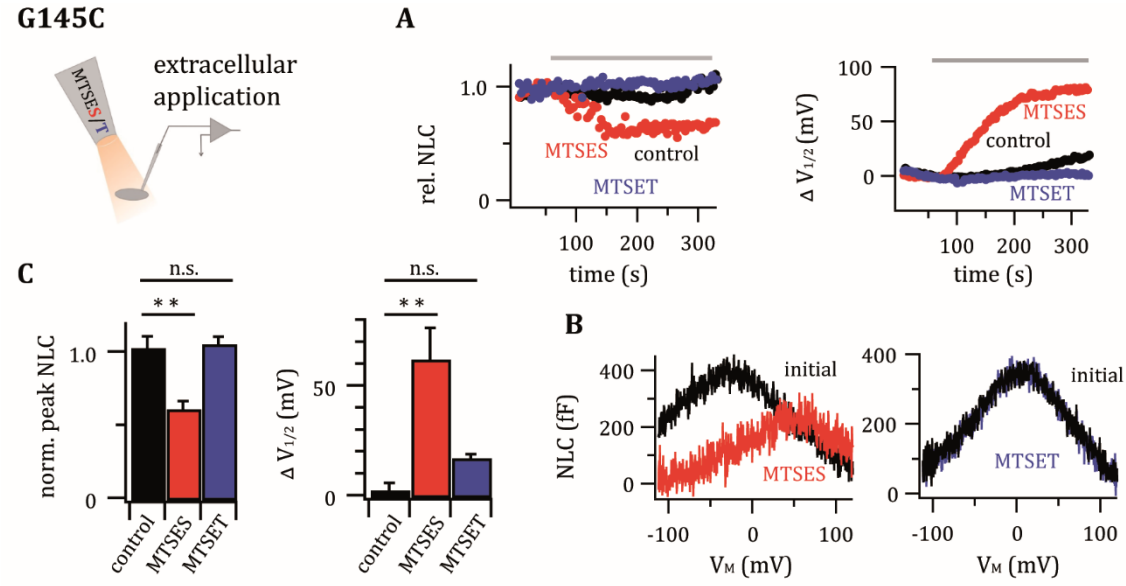

Figure 3.14: The effects of extracellular MTS application on rat prestin G145C. A: The upper two graphs of the normalised NLC and shifts of the $V_{1/2}$ are taken from Figure 3.9 and Figure 3.10. **B:** The lower two graphs are single traces from the upper graphs: the initial trace (black) is a trace before the application of the MTS reagent was started and the red (MTSES) and blue (MTSET) traces are single representative traces from a time point during the MTS application with a fully established effect. **C:** The bar diagram shows the average effect based on five measurements (n=5) with SEM for changes in the NLC peak amplitude as normalised values and changes in the $V_{1/2}$ are presented as absolute values.

3.2.2 Intracellular accessibility of positions within TM 3 in rat prestin

As before, Figure 3.15 shows WT_△Cys as a reference example for a rat prestin construct insensitive to the intracellular application of MTS reagents perfused through the patch pipette. Position S465C was previously shown to be accessible from the intracellular side (cf. Gorbunov et al., 2014) and served as a positive control for MTS modification.

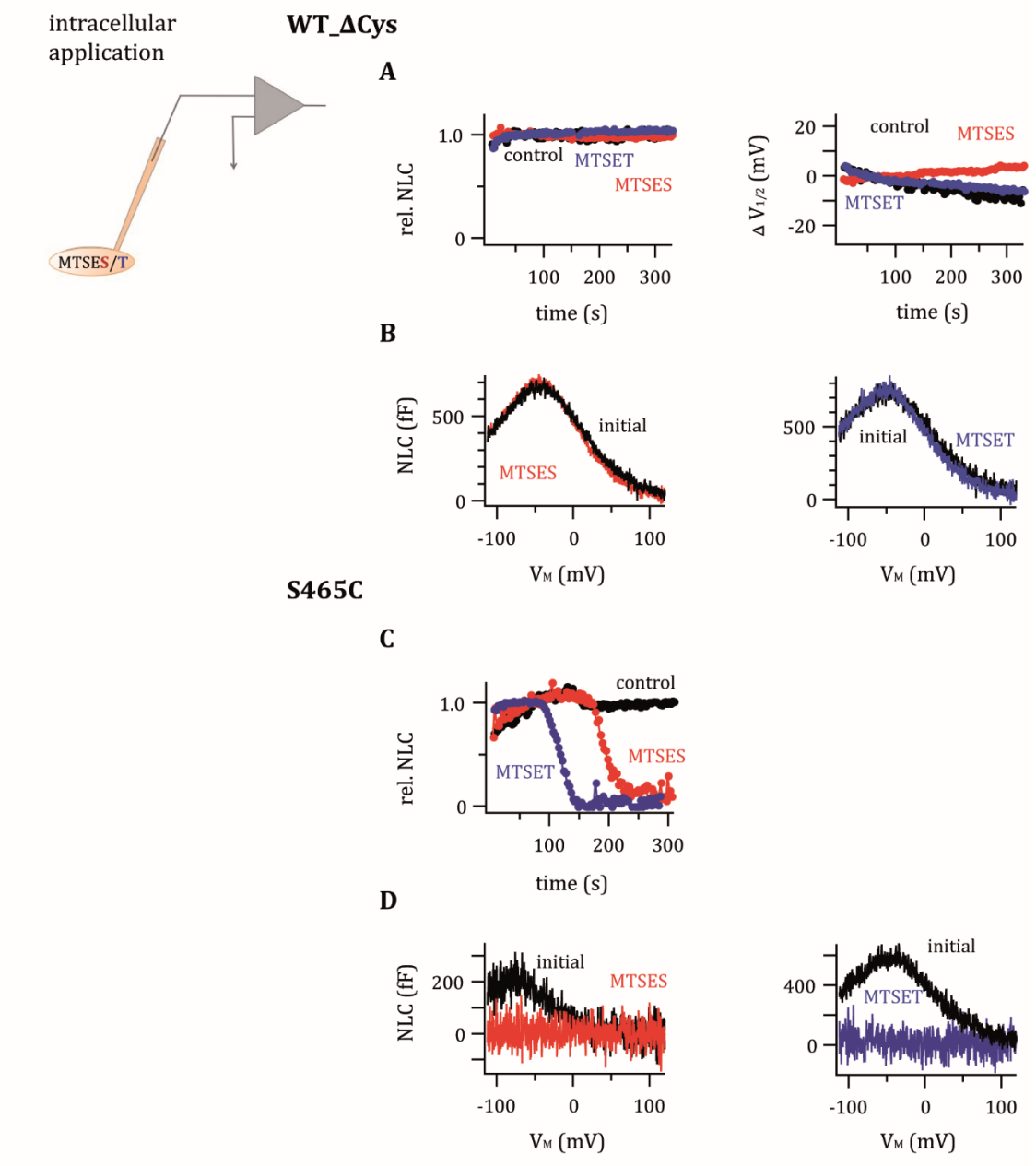

Figure 3.15: The effects of intracellular MTS application on rat prestin constructs. A+B: WT_△Cys. **A:** Normalised NLC traces and shifts of the $V_{1/2}$. **B:** Shown are single traces from the upper graphs: the initial trace (black) is a trace shortly after starting the measurement before a potential effect was distinct and the red (MTSES) and blue (MTSET) traces are single representative traces from a time point towards the end of the measurement. **C+D:** The mutant S465C is shown as example for an intracellularly accessible position (cf. Gorbunov et al., 2014). **C:** The two graphs are representative normalised traces of the NLC and the $V_{1/2}$ of the mutant S465C. **D:** Shown are single traces from the upper graphs: the initial trace (black) is a trace shortly after starting the measurement before a potential effect was distinct and the red (MTSES) and blue (MTSET) traces are single representative traces from a time point towards the end of the measurement with a fully established effect.

The results for the intracellular accessibility of positions within transmembrane domain 3 in rat prestin are presented in Figure 3.16 and Figure 3.17 in the same way as for the extracellular accessibility.

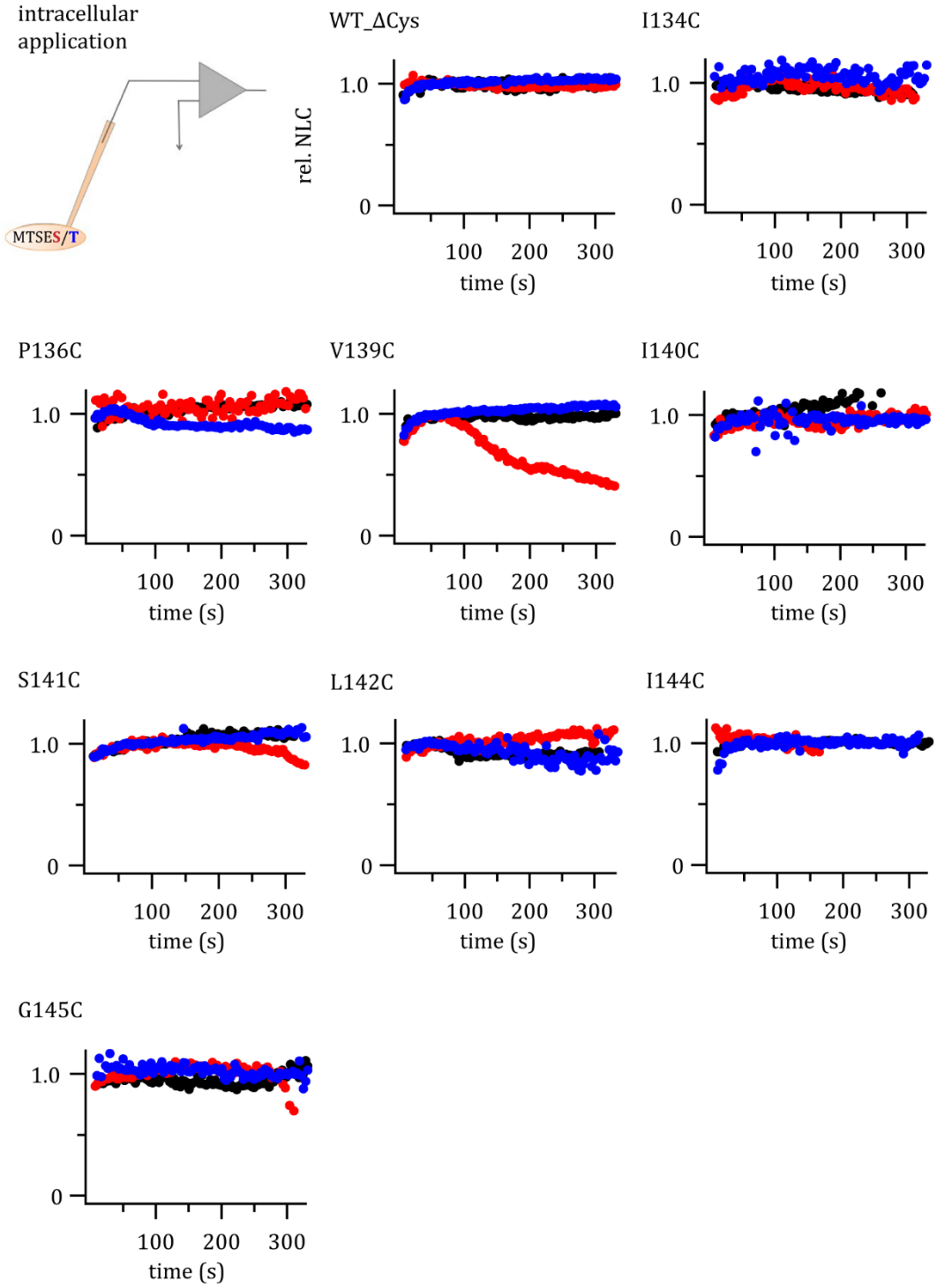

Figure 3.16: The effects of intracellularly applied MTS reagents on the NLC peak amplitude of rat prestin constructs with mutations within TM 3. WT_ΔCys was the basic construct with all cysteines mutated to alanines. All traces show a representative capacitance measurement and were normalised. In black: a control measurement without application of MTS reagents. In red: a measurement with intracellularly applied MTSES. In blue: a measurement with intracellularly applied MTSET.

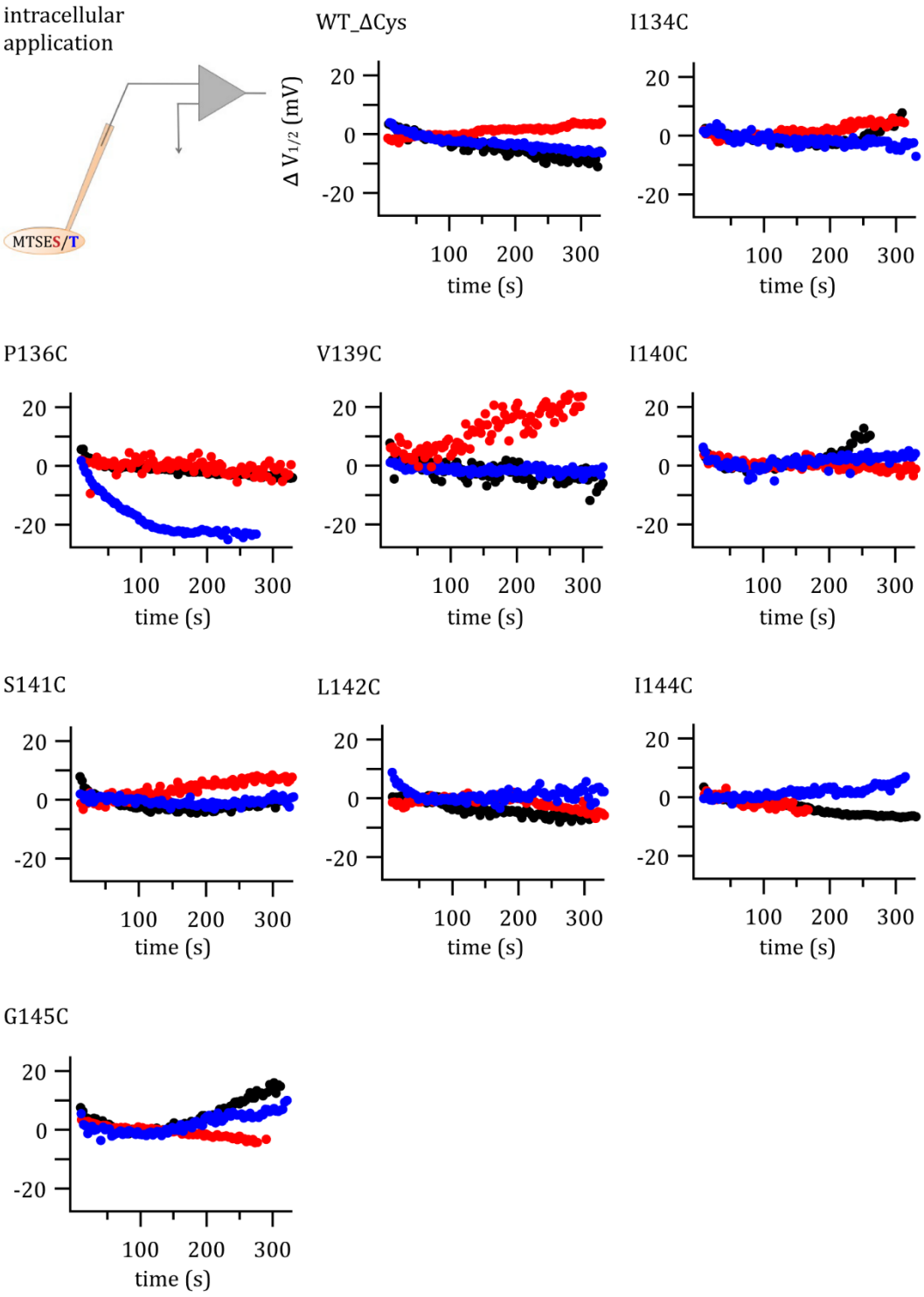

Figure 3.17: The effects of intracellularly applied MTS reagents on the $V_{1/2}$ of the rat prestin constructs with mutations within TM 3. WT_△Cys was the basic construct with all cysteines mutated to alanines. All traces show the $V_{1/2}$ of a representative measurement and were normalised. In black: a control measurement without application of MTS reagents. In red: a measurement with intracellularly applied MTSES. In blue: a measurement with intracellularly applied MTSET.

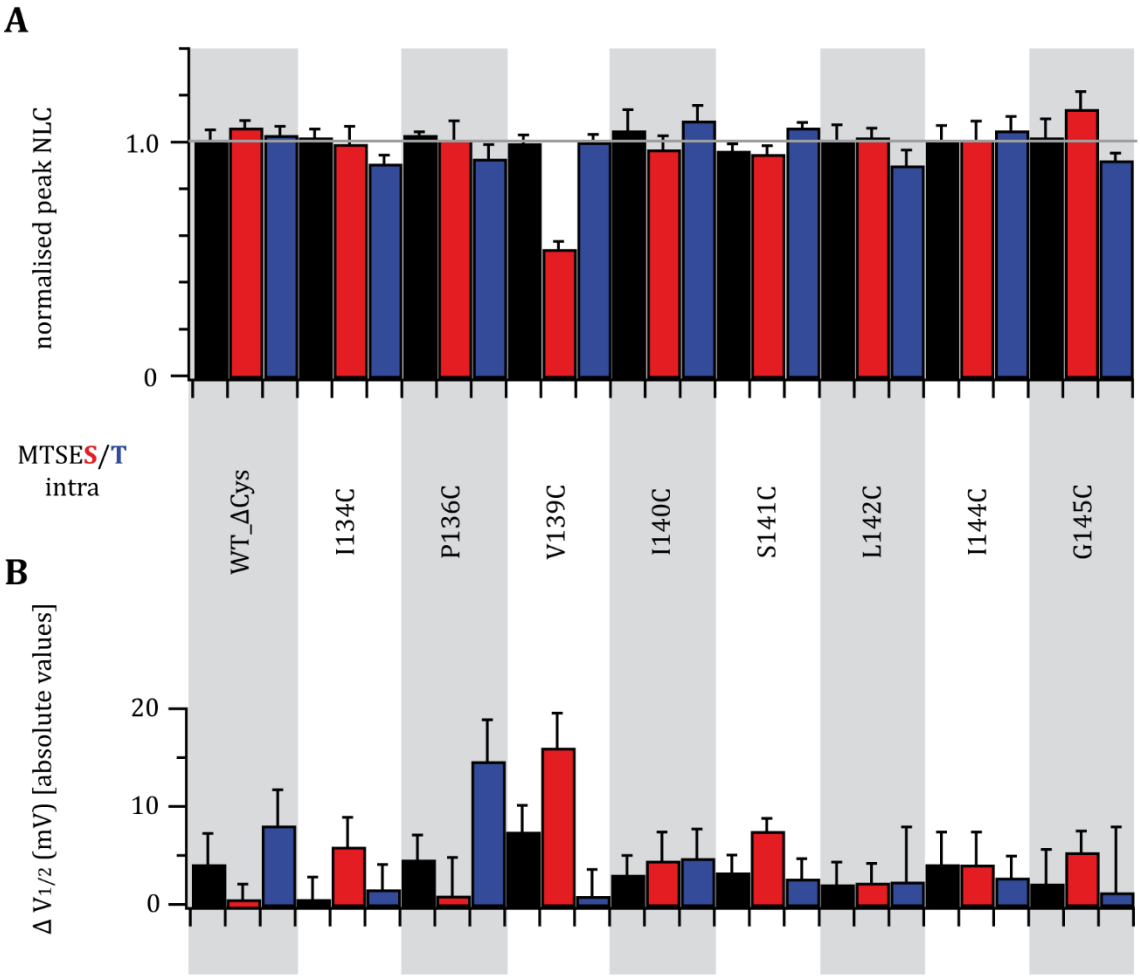

Figure 3.18: Summary of the effects of intracellularly applied MTS on rat prestin constructs with mutations within TM 3. Bars represent the mean of five measurements (n=5) ± SEM. Black bars are the control measurements without MTS application, red bars are measurements with MTSES application and blue bars are measurements with MTSET application. **A:** The bar diagram shows the changes of the normalised NLC peak amplitude upon intracellular MTS application. **B:** The bar diagram shows the changes of the $V_{1/2}$ upon intracellular MTS application. Absolute values of the $V_{1/2}$ are shown.

Figure 3.18 summarises the effects of the application of MTS reagents. It demonstrates intracellular accessibility for two mutants. The mutant P136C was intracellularly accessible to MTSET as can be seen by a shift of the $V_{1/2}$ of 14.6 ± 4.3 mV in the hyperpolarised direction (Figure 3.19). The mutant V139C exhibited changes in NLC peak combined with a shift of the $V_{1/2}$ to more positive values upon intracellular application of MTSES. Consequently, the mutant V139C is intracellularly accessible. Figure 3.20 gives detailed data that provide evidence for the intracellular accessibility of the mutant V139C. The effect following the MTSES application was a decrease in the peak NLC (54.2 ± 3.3 %) combined with a shift of the $V_{1/2}$ of 16.0 ± 3.6 mV in the depolarised direction.

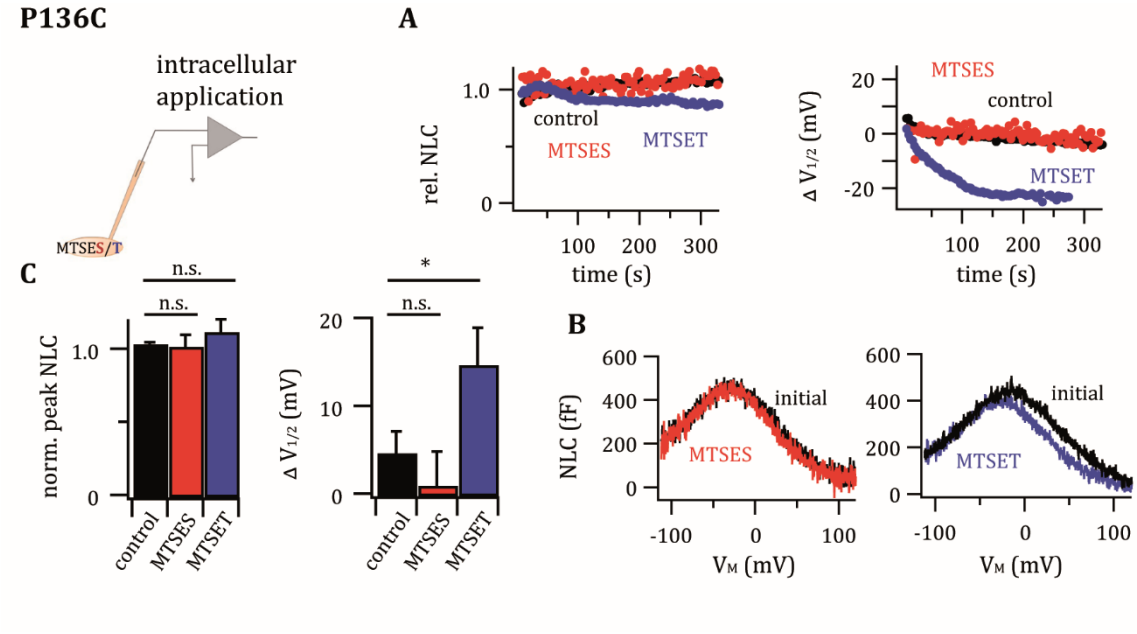

Figure 3.19: The effects of intracellular MTS application on rat prestin P136C. A: The upper two graphs of the normalised NLC and shifts of the $V_{1/2}$ are taken from Figure 3.16 and Figure 3.17. **B:** The lower two graphs are single traces from the upper graphs: the initial trace (black) is a trace shortly after starting the measurement before a potential effect was distinct and the red (MTSES) and blue (MTSET) traces are single representative traces from a time point towards the end of the measurement with a potentially fully established effect. **C:** The bar diagram shows the average effect based on five measurements (n=5) with SEM for changes in the NLC peak amplitude as normalised values and changes in the $V_{1/2}$ as absolute values.

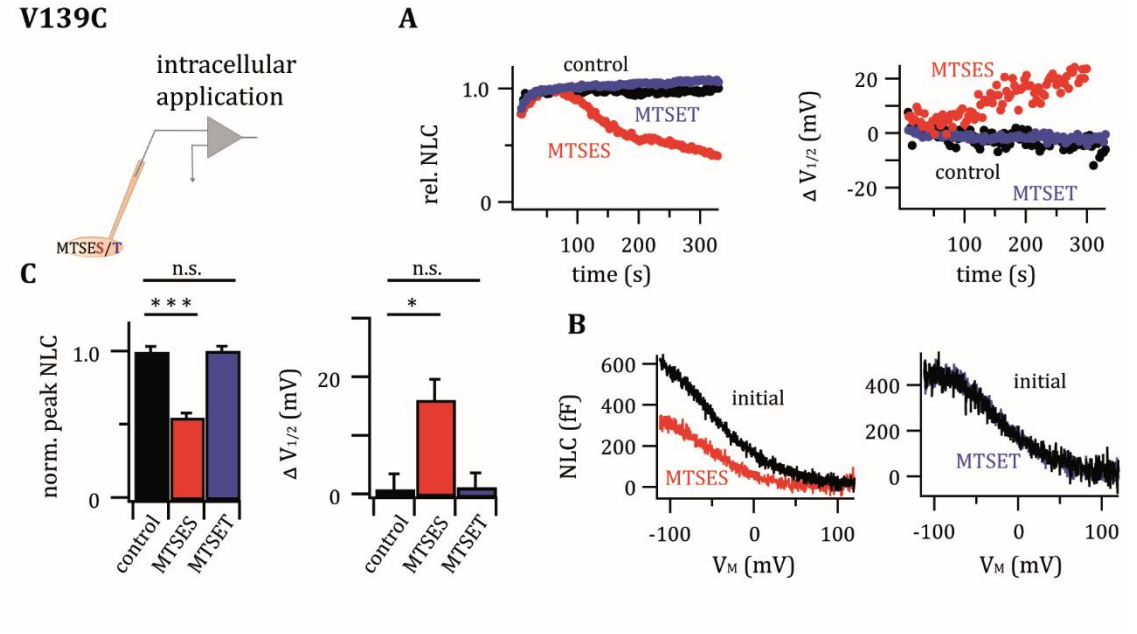

Figure 3.20: The effects of intracellular MTS application on rat prestin V139C. A: The upper two graphs of the normalised NLC and shifts of the $V_{1/2}$ are taken from Figure 3.16 and Figure 3.17. **B:** The lower two graphs are single traces from the upper graphs: the initial trace (black) is a trace shortly after starting the measurement before a potential effect was distinct and the red (MTSES) and blue (MTSET) traces are single representative traces from a time point towards the end of the measurement with a potentially fully established effect. **C:** The bar diagram shows the average effect based on five measurements (n=5) with SEM for changes in the NLC peak amplitude as normalised values and changes in the $V_{1/2}$ as absolute values.

3.2.3 Summary of cysteine accessibility in TM 3 in rat prestin

Transmembrane domain 3 in rat prestin was investigated from position I134C to I144. Table 3.4 summarises all conclusions as to the accessibility derived from the data described above. The three mutants that lacked membrane targeting (G135C, F137C, M143C) and another two mutants that were dysfunctional (A138C, G146C) are also included in Table 3.4.

The previous sections showed the effects of MTS modification on WT_△Cys and the eight rat prestin constructs with mutations within transmembrane domain 3 which displayed a strong membrane localisation and delivered proper signals. The average effects on the NLC peak amplitudes and the $V_{1/2}$ were presented in Figure 3.11 and Figure 3.18. Detailed information on each position, which was not modified by application of MTS reagents, is attached in the supplement (Supplemental figure 7.1). Table 3.4 sums up the results of the experiments concerning membrane localisation, functionality and accessibilities.

Table 3.4: Overview of the results of the scanning of rat prestin constructs with mutations within TM 3. Predominant membrane localisation and functionality are marked with + and accordingly cytosolic localisation and lack of functionality with -. Yellow indicates insensitivity (-) to MTS reagents, accessibility from the extracellular side is marked in blue, from the intracellular side in red and additionally with +. Positions with a lack of membrane targeting or functionality were not tested for their accessibility and are therefore not determined (n.d.).

	PM	functional	extracellularly accessible		intracellularly accessible	
			MTSES	MTSET	MTSES	MTSET
I134	+	+	—	—	—	—
G135	—	n.d.	n.d.	n.d.	n.d.	n.d.
P136	+	+	—	—	—	+
F137	—	n.d.	n.d.	n.d.	n.d.	n.d.
A138	+	—	n.d.	n.d.	n.d.	n.d.
V139	+	+	+	+	+	—
I140	+	+	—	—	—	—
S141	+	+	—	—	—	—
L142	+	+	+	+	—	—
M143	—	n.d.	n.d.	n.d.	n.d.	n.d.
I144	+	+	—	—	—	—
G145	+	+	+	—	—	—
G146	+	—	n.d.	n.d.	n.d.	n.d.

Figure 3.21 maps these results onto the structural homology model of Gorbunov et al. from 2014. The transmembrane domains 1, 3, 8 and 10 are shown and additionally the accessible positions were highlighted in colour.

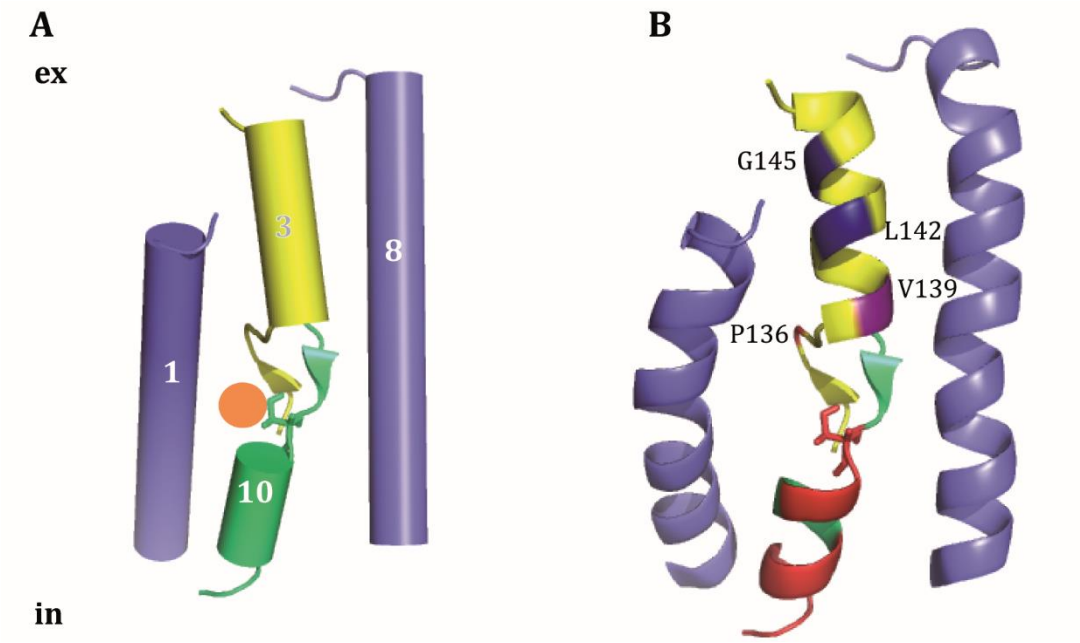

Figure 3.21: Parts of the structural homology model of rat prestin based on UraA with the TMs 1, 3, 8 and 10. TM 3 is shown in yellow, TM 10 in green and the putative anion-binding site (S396) is shown as sticks. **A:** The orange circle represents a bound anion at the presumptive anion-binding site. **B**: The model is expanded for accessibility results of TM 3. The model shows the presumptive structural localisation of positions that were accessible from the intracellular (red), extracellular (blue) side or double accessible (purple). The model is based on the results of Gorbunov et al., 2014.

3.3 SCAM of zebrafish prestin

The zebrafish prestin constructs with cysteine substitutions in transmembrane domains 3 and 10 that showed a wild type-like membrane localisation (cf. Figure 3.2 and Figure 3.3) and delivered robust transport currents (cf. Figure 3.6 and Figure 3.7) were further investigated for MTS accessibilities. The principles of the measurements of the transport currents of the zebrafish prestin constructs were as described in section 3.1.

3.3.1 Transmembrane domain 3 of zebrafish prestin

Among the 13 zebrafish prestin constructs with mutations in transmembrane domain 3, three mutants lacked a predominant membrane localisation of prestin and another three mutants were dysfunctional. Thus, seven mutants were analysed by SCAM.

3.3.2 Extracellular accessibility of positions within TM 3 in zebrafish prestin

In Figure 3.22 representative traces of two zebrafish prestin mutants are shown, of the basic construct WT_△Cys which was insensitive to applied MTS reagents as expected and of a mutant whose transport current decreased upon extracellular MTSES application and which was therefore considered extracellularly accessible (cf. Figure 3.24). The increase of the transport current at the beginning of the measurements was observed consistently in all functional mutants and can be attributed to relatively slow equilibration of oxalate between the patch pipette and the cell.

Figure 3.23 shows representative measurements of normalised transport currents and the effects of extracellular MTS application on the zebrafish prestin constructs with cysteine mutations in transmembrane domain 3. There was a strong decrease of the transport currents upon MTS application in the mutants V140C, S142C, L143C and G147. Application of MTSES was also followed by a decrease in the transport current in the mutant M144C in this individual recording. However, this effect was less pronounced between experiments and, ultimately, turned out to be not statistically significant. Thus, position M144C was considered not to be extracellularly accessible. The extracellular accessibility of the other positions is summarised by the bar diagram of Figure 3.24 and details are shown in the following figures.

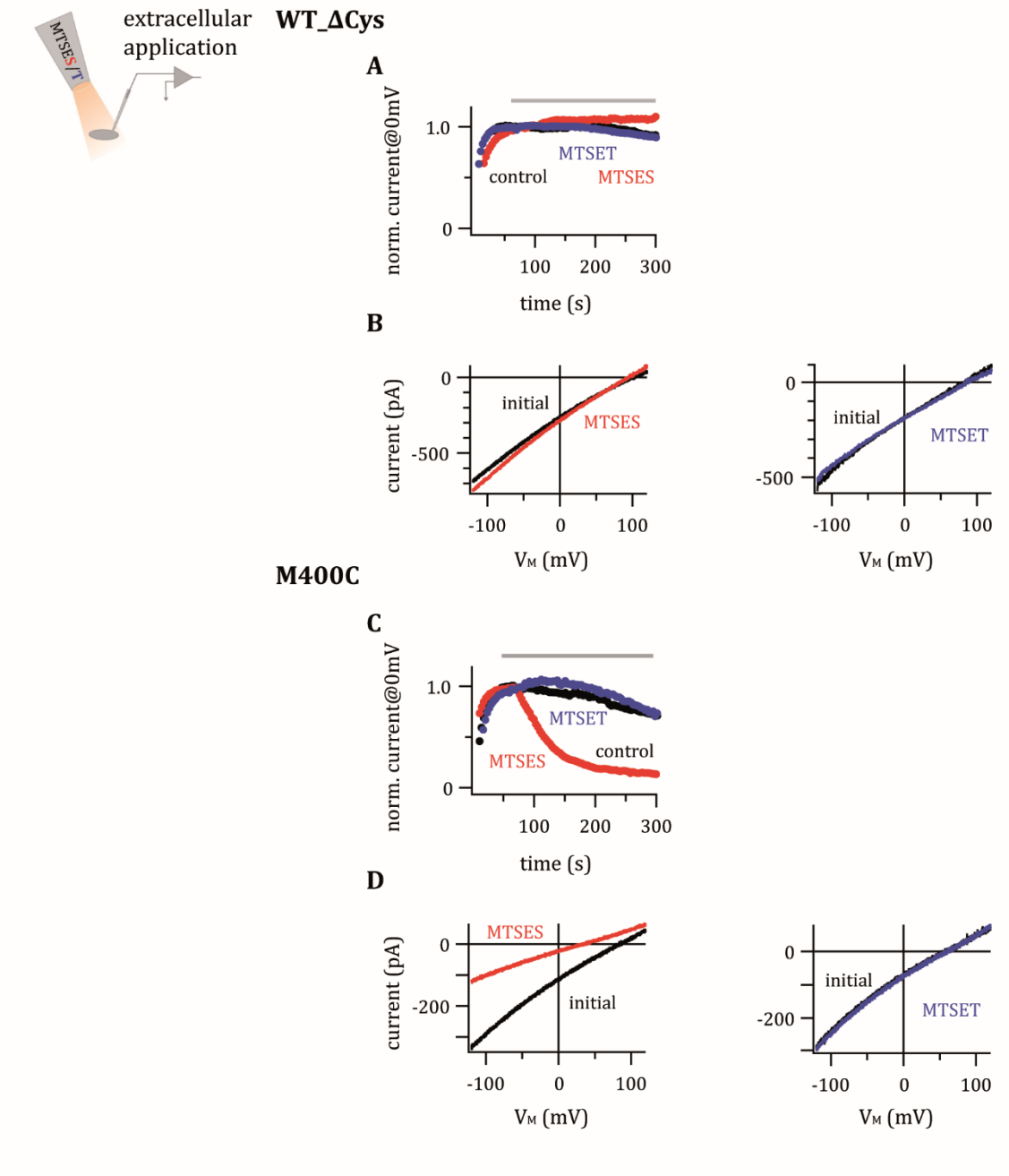

Figure 3.22: The effects of extracellular MTS application on zebrafish prestin constructs. A+B: WT_△Cys. **A:** A graph of representative normalised traces of the transport currents at 0 mV. **B:** Shown are single traces from the upper graph: the initial trace (black) was a trace before the application of MTS reagents was started and the red (MTSES) and blue (MTSET) traces were single representative traces from a time point during the MTS application. **C+D:** The mutant M400C is shown as an example for an extracellularly accessible position. **C:** The two graphs are representative normalised traces of the transport current at 0 mV of the mutant M400C. **D:** Shown are single traces from the upper graphs: the initial trace (black) was a trace before the application of the MTS reagents was started and the red (MTSES) and blue (MTSET) traces were single representative traces from a time point during the MTS application with a fully established effect.

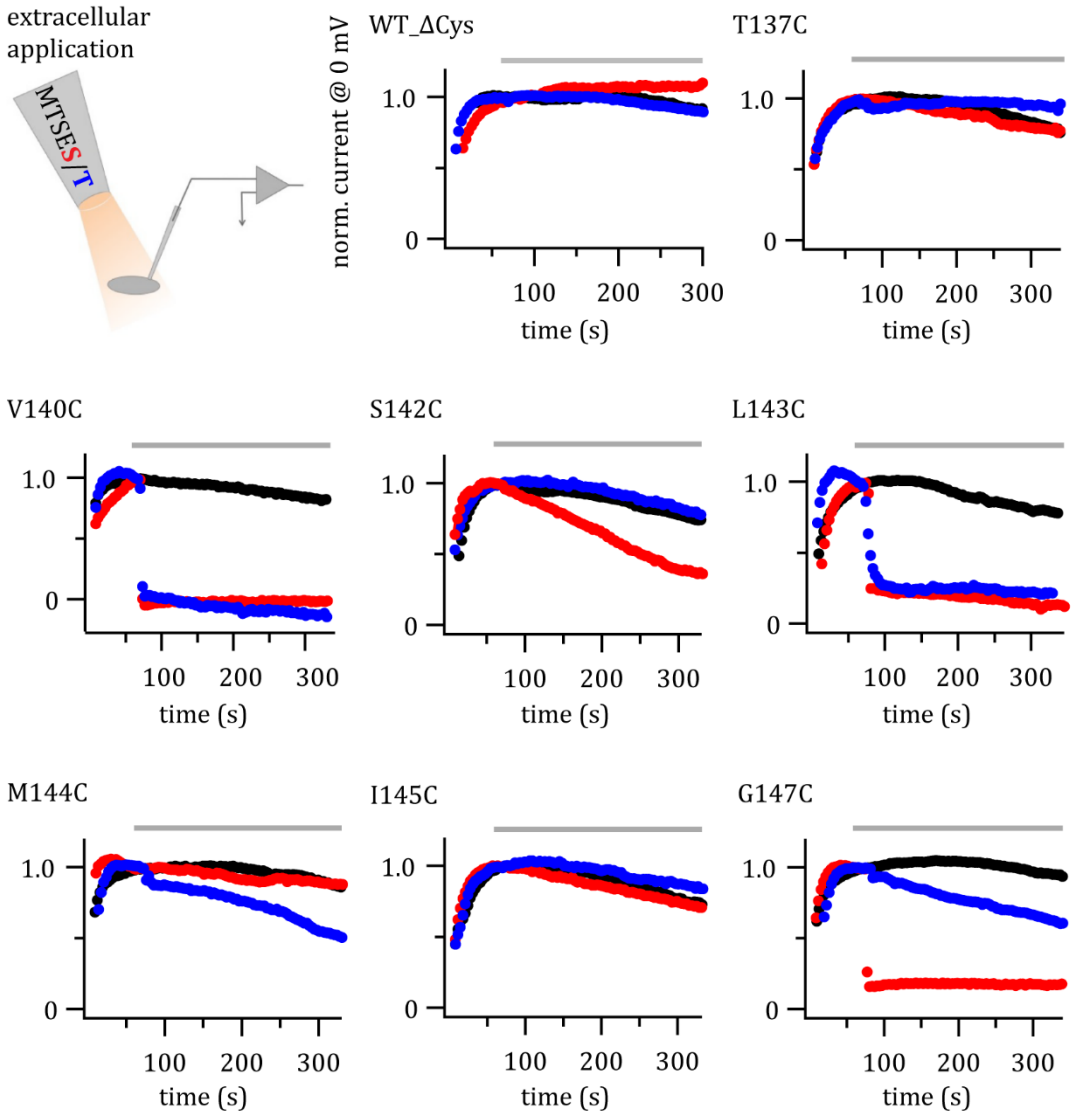

Figure 3.23: The effects of extracellularly applied MTS reagents on the transport currents of the zebrafish prestin constructs with mutations within TM 3. WT_△Cys was the basic construct with nearly all cysteines mutated to alanines (cf. 2.4). All traces show transport currents of a representative measurement and were normalised. In black: a control measurement without application of MTS reagents. In red: a measurement with extracellularly applied MTSES. In blue: a measurement with extracellularly applied MTSET.

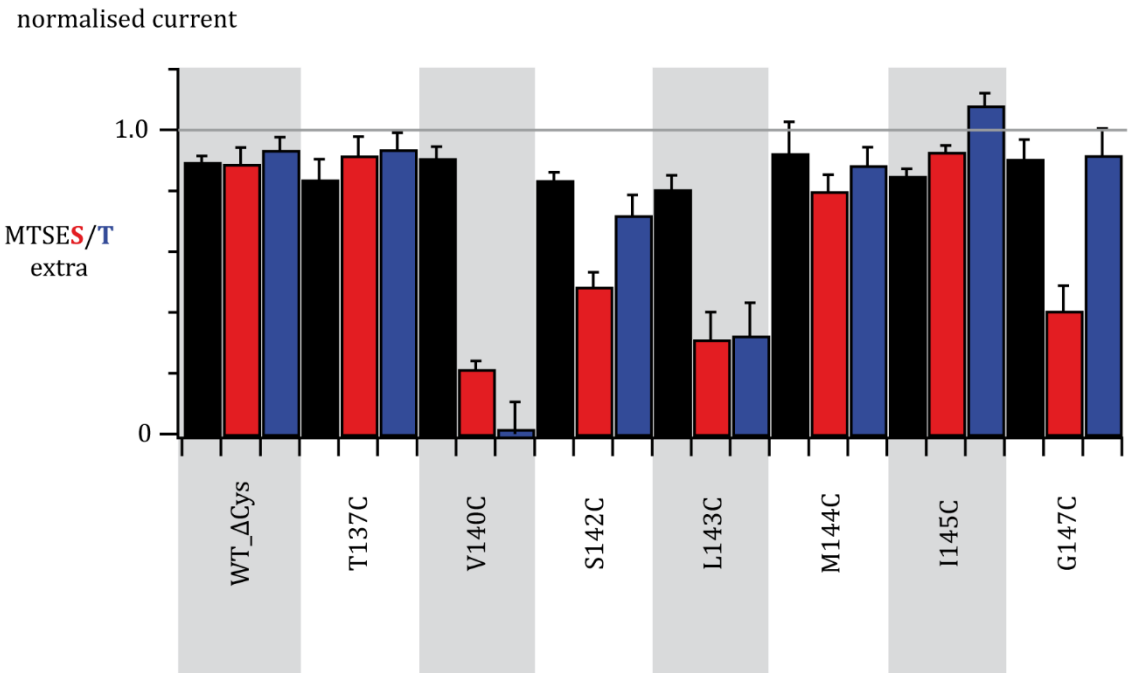

Figure 3.24: Summary of the effects of extracellularly applied MTS on zebrafish prestin constructs with mutations within TM 3. Bars represent the mean of five measurements (n=5) ± SEM. Black bars are the control measurements without MTS application, red bars are measurements with MTSES application and blue bars are measurements with MTSET application. The bar diagram shows the changes of normalised transport currents on extracellular MTS application.

The cysteine at position V140C was accessible from the extracellular side to both MTS reagents. The effects were statistically highly significant as the bar diagram of Figure 3.25 demonstrates. The transport current decreased drastically upon the application of MTSES (to 2.1 ± 2.6 % of the initial current) as well as of MTSET (to 0 ± 10.5 %).

Accessibility of cysteine S142C was only moderate in terms of kinetics and maximal effect (Figure 3.26). Even if the effect built up slowly upon MTSES application, the transport current decreased to 48.5 ± 4.7 % compared to its initial value, which was highly significant. In contrast, the application of MTSET did not affect the transport current of S142C (72.0 ± 6.7 %).

The transport currents of the mutant L143C were also affected by extracellular MTS (Figure 3.27). The effects were statistically significant (MTSES: 31.2 ± 8.9 % and MTSET: 32.4 ± 10.9 %). The cysteine G147C was only accessible to the negatively charged MTSES (Figure 3.28). The average decrease of the transport current was to 40.6 ± 8.2 % upon application of MTSES (MTSET: 91.7 ± 8.8 %).

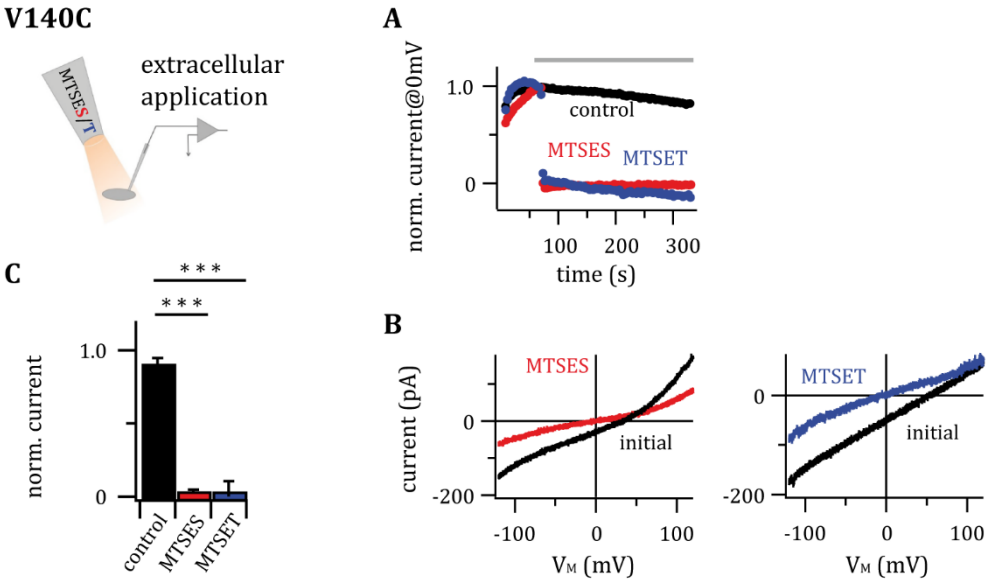

Figure 3.25: The effects of extracellular MTS application on zebrafish prestin V140C. A: The upper graph is taken from Figure 3.23. **B:** The lower two graphs are single traces from the upper graphs: the initial trace (black) is a trace before the application of the MTS reagents was started and the red (MTSES) and blue (MTSET) traces are single representative traces from a time point during the MTS application with a fully established effect. **C:** The bar diagram shows the average effect based on five measurements (n=5) with SEM for changes in the transport currents as normalised values.

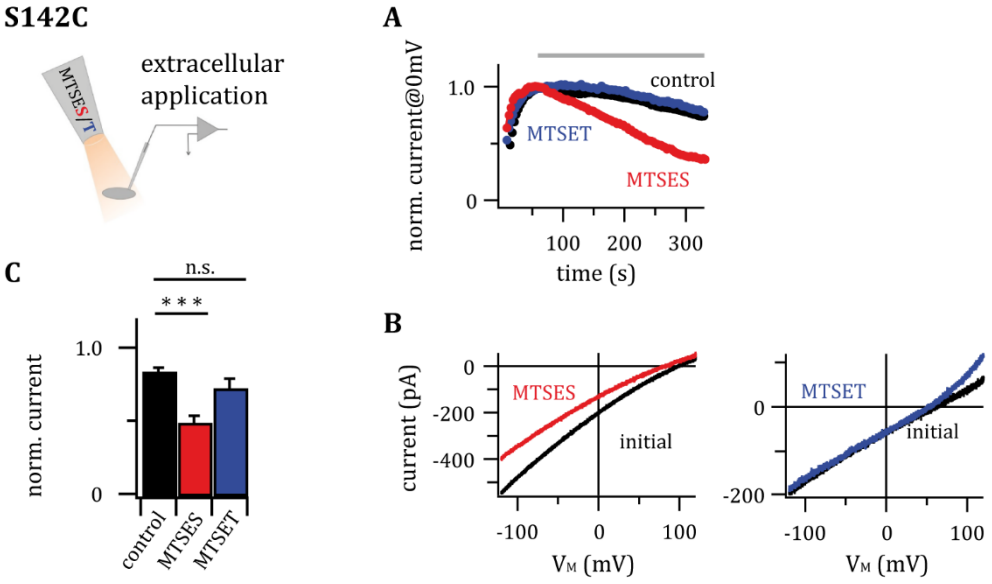

Figure 3.26: The effects of extracellular MTS application on zebrafish prestin S142C. A: The upper graph is taken from Figure 3.23. **B:** The lower two graphs are single traces from the upper graphs: the initial trace (black) is a trace before the application of the MTS reagents was started and the red (MTSES) and blue (MTSET) traces are single representative traces from a time point during the MTS application with a fully established effect. **C:** The bar diagram shows the average effect based on five measurements (n=5) with SEM for changes in the transport currents as normalised values.

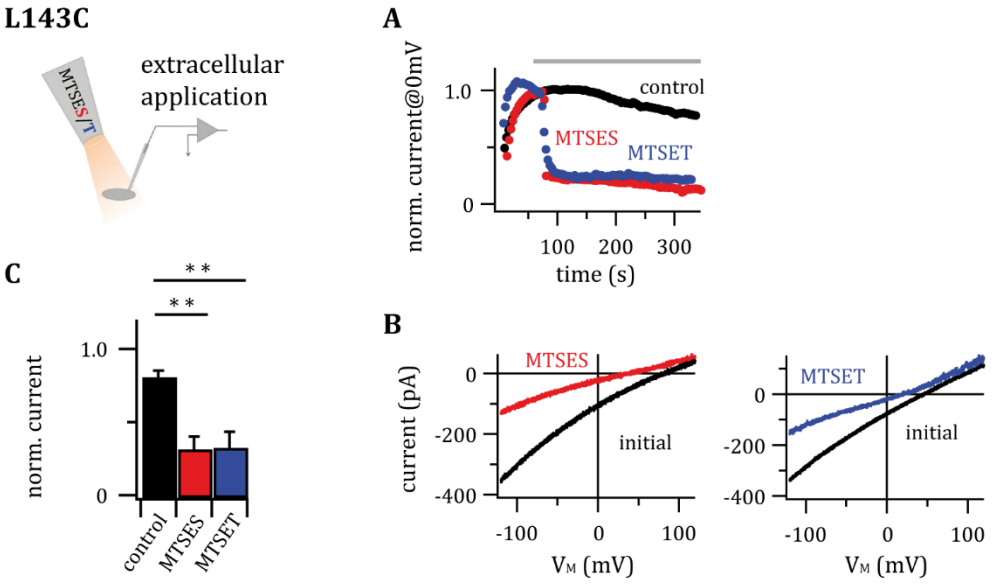

Figure 3.27: The effects of extracellular MTS application on zebrafish prestin L143C. A: The upper graph is taken from Figure 3.23. **B:** The lower two graphs are single traces from the upper graphs: the initial trace (black) is a trace before the application of the MTS reagents was started and the red (MTSES) and blue (MTSET) traces are single representative traces from a time point during the MTS application with a fully established effect. **C** The bar diagram shows the average effect based on five measurements (n=5) with SEM for changes in the transport currents as normalised values.

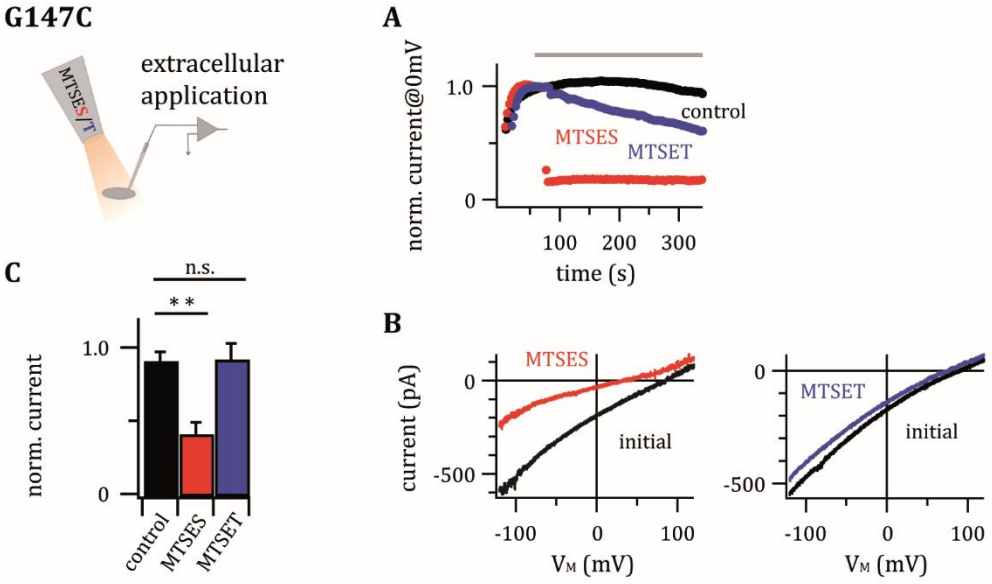

Figure 3.28: The effects of extracellular MTS application on zebrafish prestin G147C. A: The upper graph is taken from Figure 3.23. **B:** The lower two graphs are single traces from the upper graphs: the initial trace (black) is a trace before the application of the MTS reagents was started and the red (MTSES) and blue (MTSET) traces are single representative traces from a time point during the MTS application with a fully established effect. **C** The bar diagram shows the average effect based on five measurements (n=5) with SEM for changes in the transport currents as normalised values.

3.3.3 Intracellular accessibility of positions within TM 3 in zebrafish prestin

Again, representative traces of normalised currents and the associated I-V curves of the zebrafish prestin construct WT_△Cys and the mutant M400C, which was sensitive to the intracellular application of MTS, are shown in Figure 3.29.

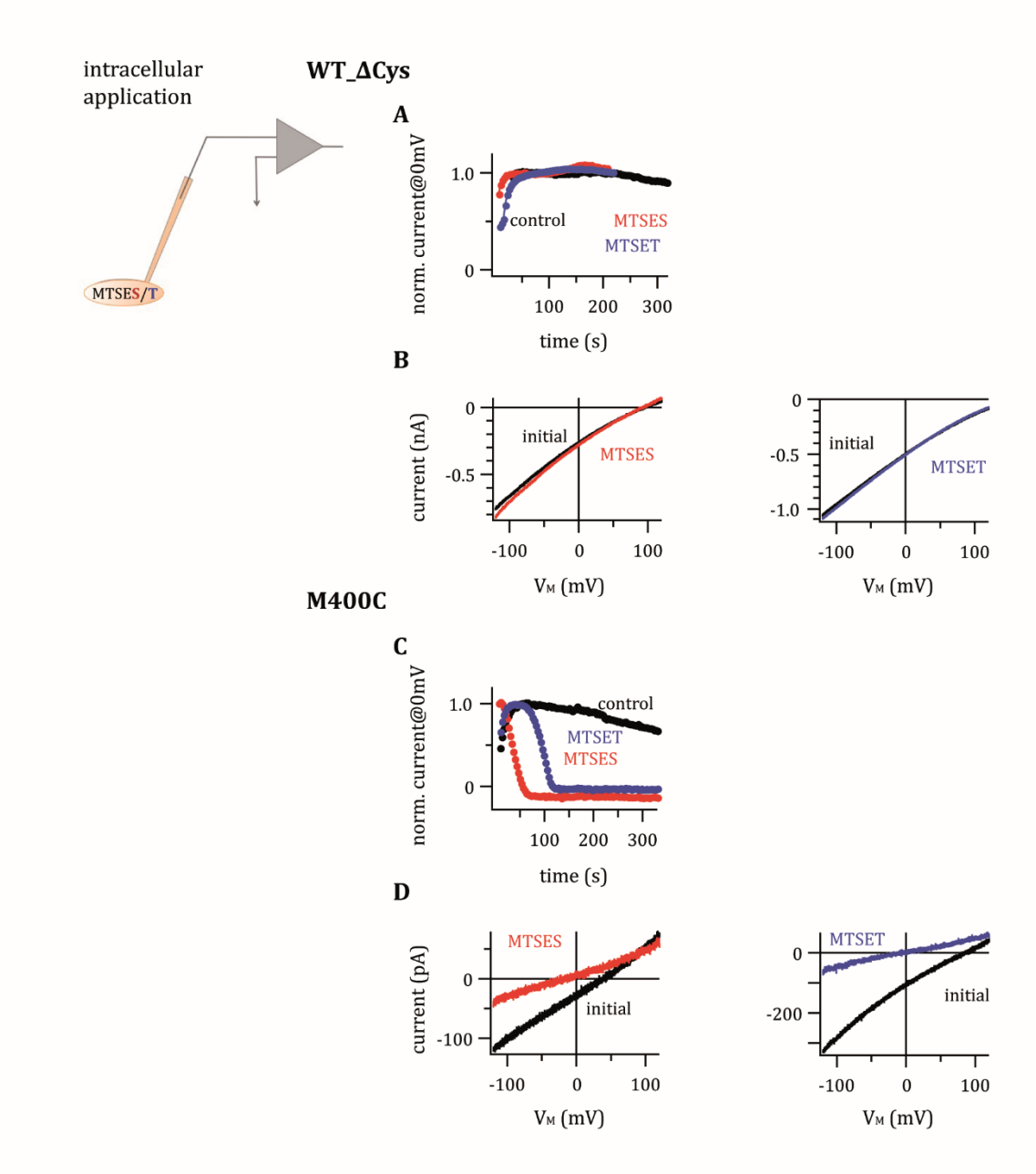

Figure 3.29: The effects of intracellular MTS application on zebrafish prestin constructs. A+B: WT_△Cys. **A:** A graph of representative normalised traces of the transport current at 0 mV. **B:** Shown are single traces from the upper graph: the initial trace (black) is a trace shortly after starting the measurement before a potential effect was distinct and the red (MTSES) and blue (MTSET) traces are single representative traces from a time point towards the end of the measurement. **C+D:** The mutant M400C is shown as example for an intracellularly accessible position. **C:** The two graphs are representative normalised traces of the transport current at 0 mV of the mutant M400C. **D:** Shown are single traces from the upper graphs: the initial trace (black) is a trace shortly after starting the measurement before a potential effect was distinct and the red (MTSES) and blue (MTSET) traces are single representative traces from a time point towards the end of the measurement with a potentially fully established effect.

Figure 3.30 shows representative measurements of normalised transport currents and the effects of intracellular MTS application on all of the functional cysteine mutants. Figure 3.31 gives an overview of the effects of intracellular MTS application on the zebrafish prestin constructs with mutations within transmembrane domain 3. A representative normalised trace as well as the statistics of intracellularly applied MTSES are missing for the mutant V140C because of a lack of sufficient independent recordings of appropriate quality.

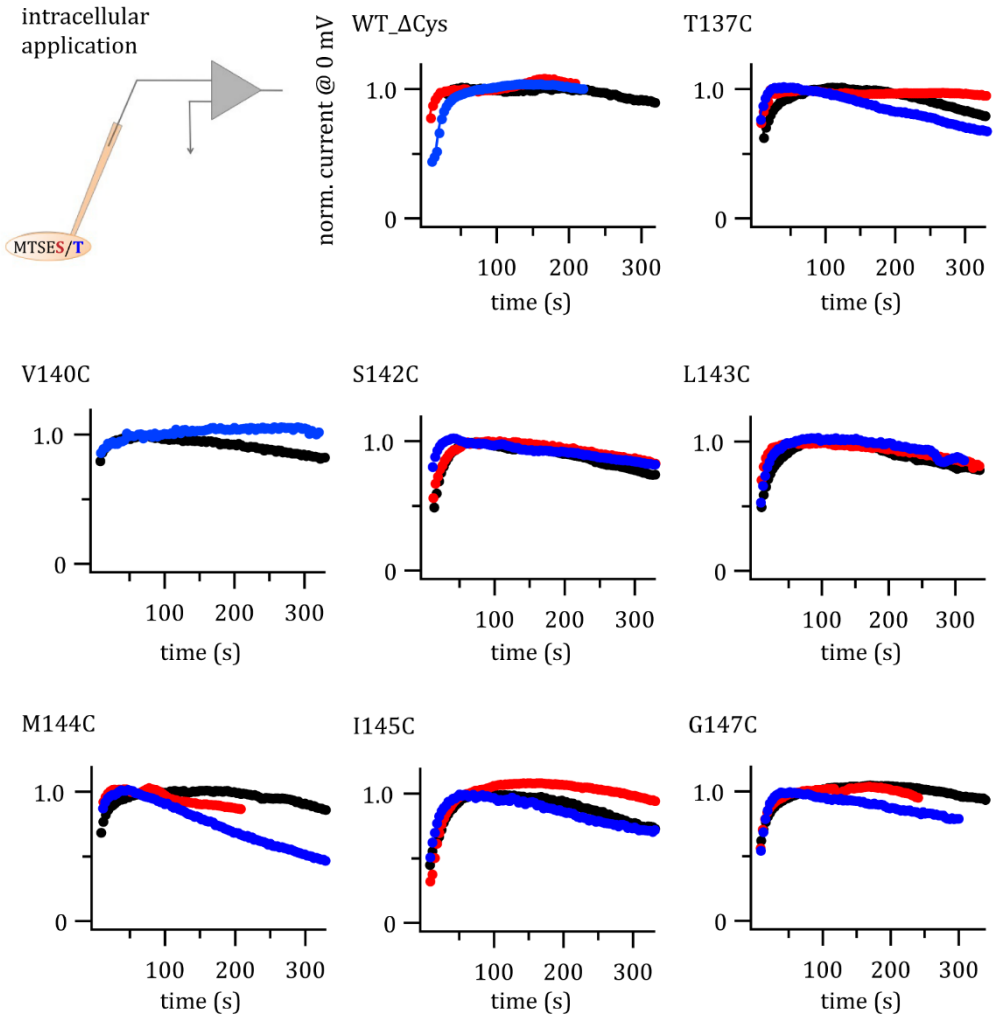

Figure 3.30: The effects of intracellularly applied MTS reagents on the transport currents of the zebrafish prestin constructs with mutations within TM 3. WT_△Cys was the basic construct with nearly all cysteines mutated to alanines (cf. 2.4). All traces show transport currents of a representative measurement and were normalised. In black: a control measurement without application of MTS reagents. In red: a measurement with intracellularly applied MTSES. In blue: a measurement with intracellularly applied MTSET.

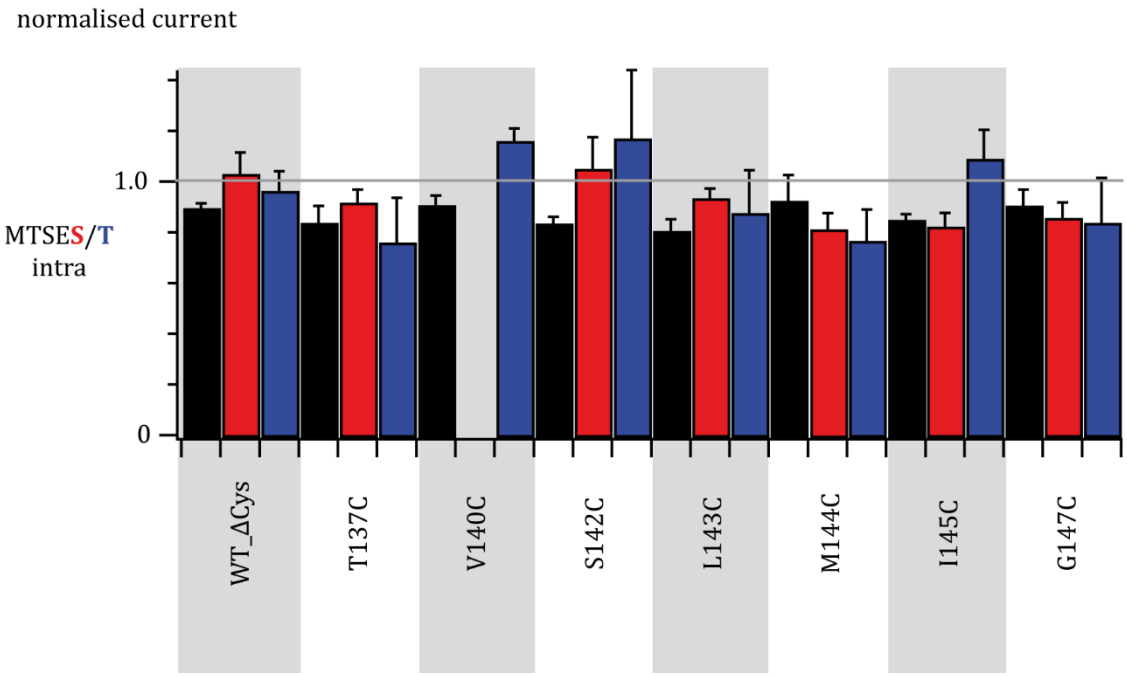

Figure 3.31: Summary of the effects of intracellularly applied MTS on zebrafish prestin constructs with mutations within TM 3. Bars represent the mean of five measurements (n=5) measurements ± SEM, except for position V140C under intracellular MTSET application where the bar only represents four measurements (n=4) ± SEM. The bar of intracellular MTSES application for the mutant V140C is missing because of a lack of sufficient independent recordings of appropriate quality. Black bars are the control measurements without MTS application, red bars are measurements with MTSES application and blue bars are measurements with MTSET application. The bar diagram shows the changes of the normalised transport currents on intracellular MTS application.

An effect of intracellularly applied MTS reagents on constructs of zebrafish prestin with mutations within transmembrane domain 3 was limited to V140C if at all. While measurements without MTS application produced strong signals (Table 3.2), measurements with intracellularly offered oxalate (106 mM) and MTSES delivered no or only very small transport currents. There have been numerous unsuccessful attempts to get evaluable signals. Possible explanations for this problem will be considered in the discussion section. The statistics for the effect of intracellularly applied MTSET were based on four measurements and the transport current was not affected by the application of MTSET from the intracellular side (116.1 ± 5.1 %).

3.3.4 Summary of cysteine accessibility in TM 3 in zebrafish prestin

Transmembrane domain 3 in zebrafish prestin was investigated from position I135 to G147, which are the structurally homologous positions to the investigated part of transmembrane domain 3 in rat prestin. All results of the scanning of the zebrafish prestin constructs with mutations within transmembrane domain 3 are listed in Table 3.5. Detailed information on each position insensitive to MTS reagents, is presented in the supplement (Supplemental figure 7.2).

Table 3.5: Overview of the results of the scanning of zebrafish prestin constructs with mutations within TM 3. Predominant membrane localisation and functionality are marked with + and accordingly cytosolic localisation and lack of functionality with -. Yellow indicates insensitivity (-) to MTS reagents, accessibility from the extracellular side is marked in blue, from the intracellular side in red and additionally with +. Positions with a lack of membrane targeting or functionality were not tested for their accessibility and are therefore not determined (n.d.). No final conclusion of the intracellular accessibility (MTSES) can yet be made for the position V140.

	PM	functional	extracellularly accessible		Intracellularly accessible	
			MTSES	MTSET	MTSES	MTSET
I135	—	n.d.	n.d.	n.d.	n.d.	n.d.
G136	—	n.d.	n.d.	n.d.	n.d.	n.d.
T137	+	+	—	—	—	—
F138	+	—	n.d.	n.d.	n.d.	n.d.
A139	+	—	n.d.	n.d.	n.d.	n.d.
V140	+	+	+	+	?	—
I141	—	n.d.	n.d.	n.d.	n.d.	n.d.
S142	+	+	+	—	—	—
L143	+	+	+	+	—	—
M144	+	+	n.d.	n.d.	n.d.	n.d.
I145	+	+	—	—	—	—
G146	+	—	n.d.	n.d.	n.d.	n.d.
G147	+	+	+	—	—	—

Figure 3.32 maps the results of the cysteine accessibility of transmembrane domain 3 in zebrafish prestin onto the structural homology model. Comparable with transmembrane domain 3 in rat prestin, the positions of zebrafish prestin within transmembrane domain 3 were expected to be mainly accessible from the extracellular side of the plasma membrane. In fact, four positions were accessible from the outside. Three of them are structurally homologous positions to the extracellularly accessible positions in rat prestin. Data on the intracellular application of MTSES for V140C were inconsistent and therefore, the accessibility from the intracellular side of the position V140 remains unknown. For this reason, this possible accessibility was not included in Figure 3.32.

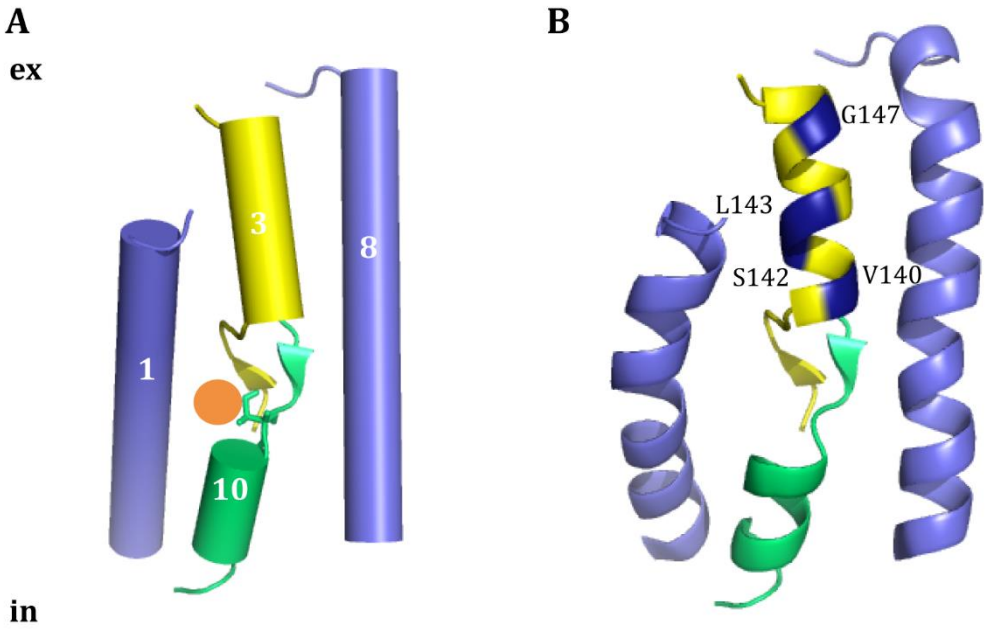

Figure 3.32: Parts of the structural homology model of zebrafish prestin based on UraA with the TMs 1, 3, 8 and 10. TM 3 is shown in yellow, TM 10 in green and the putative anion-binding site (S399 in zebrafish prestin) is shown as sticks. **A:** The orange circle represents a bound anion at the presumptive anion-binding site. **B**: The model is expanded for accessibility results of TM 3. The model shows the presumptive structural localisation of positions that were accessible from the extracellular (blue) side. The model is based on the results of Gorbunov et al., 2014.

3.3.5 Transmembrane domain 10 of zebrafish prestin

All zebrafish prestin constructs with mutations within transmembrane domain 10 showed a strong membrane localisation (cf. Figure 3.3). As mentioned before, the mutants T393C, F394C and V395C showed appropriate membrane targeting of prestin but because of their positions, which are predicted to be located in the bulk of the protein, they were not further investigated. Additionally, the mutant H392C was examined, since the structurally homologous position in rat prestin (Q389) was extracellularly accessible (Gorbunov et al., 2014). Finally, nine mutants which were tested for their functionality exhibited transport currents that were large enough to be identified unequivocally (cf. Figure 3.7) and thus, were examined for their accessibility.

3.3.6 Extracellular accessibility of positions within TM 10 in zebrafish prestin

Representative experiments obtained with zebrafish prestin constructs were already shown in Figure 3.22 and Figure 3.29 and, thus, were not additionally included in this section. Figure 3.33 shows normalised transport currents of constructs with mutations within transmembrane domain 10.

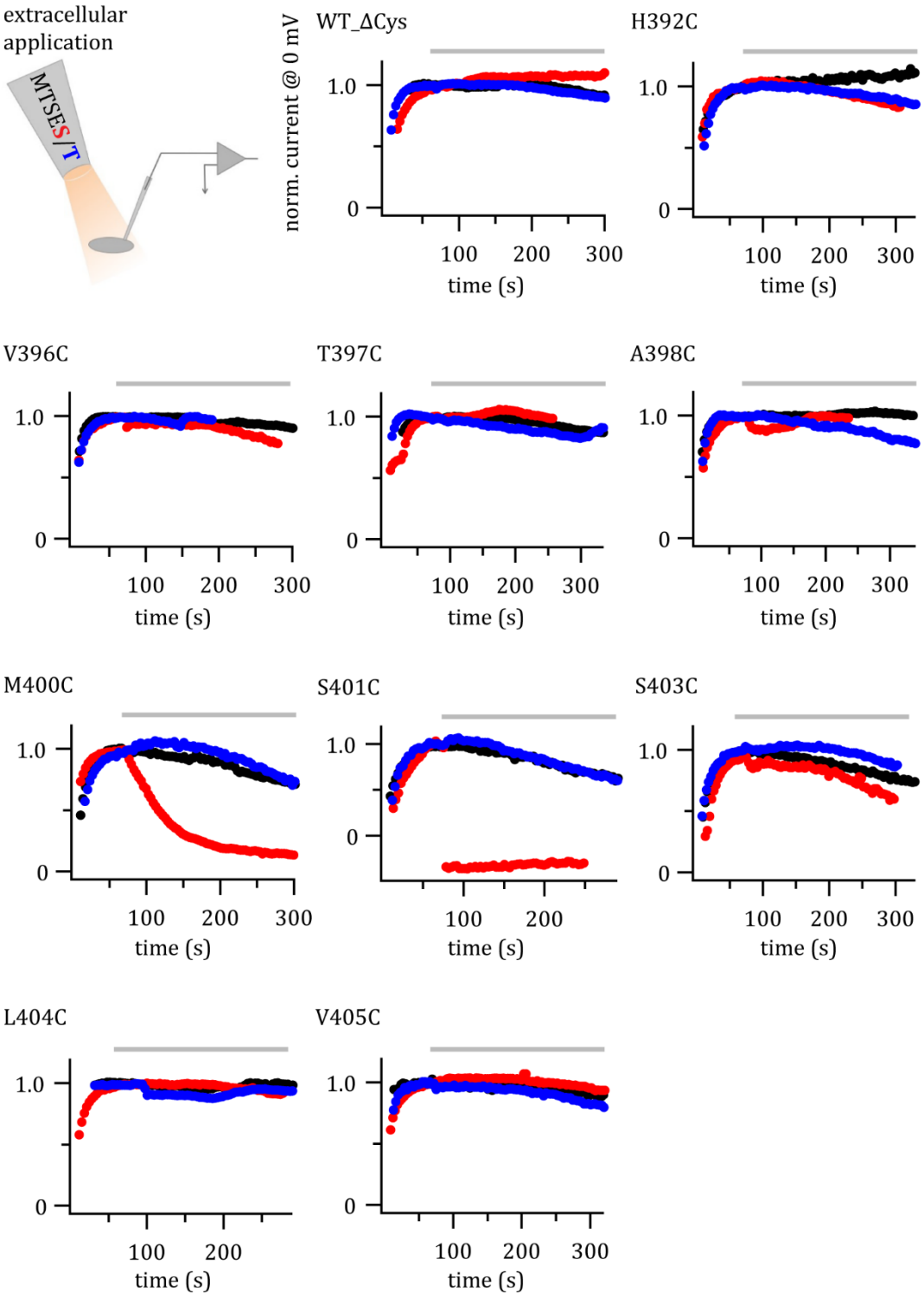

Figure 3.33: The effects of extracellularly applied MTS reagents on the transport currents of the zebrafish prestin constructs with mutations within TM 10. WT_△Cys was the basic construct with nearly all cysteines mutated to alanines (cf. 2.4). All traces show transport currents of a representative measurement and were normalised. In black: a control measurement without application of MTS reagents. In red: a measurement with extracellularly applied MTSES. In blue: a measurement with extracellularly applied MTSET.

Figure 3.34 gives an overview of the mean effects of extracellular MTS application on transport currents of the zebrafish prestin constructs with mutations within transmembrane domain 10. The transport currents of the mutants M400C and S401C were modified by MTSES, as indicated by a rapid decrease of the transport current upon extracellular MTSES application. The transport current of the mutant M400C decreased to 15.0 ± 3.0 % (73.6 ± 4.3 %) upon application of MTSES (MTSET) (Figure 3.35). The effect of extracellularly applied MTSES on the mutant S401C was even more pronounced, as the transport current was entirely abolished (0 ± 8.1 %), whereas the application of MTSET had no effect (102.0 ± 2.1 %) (Figure 3.36).

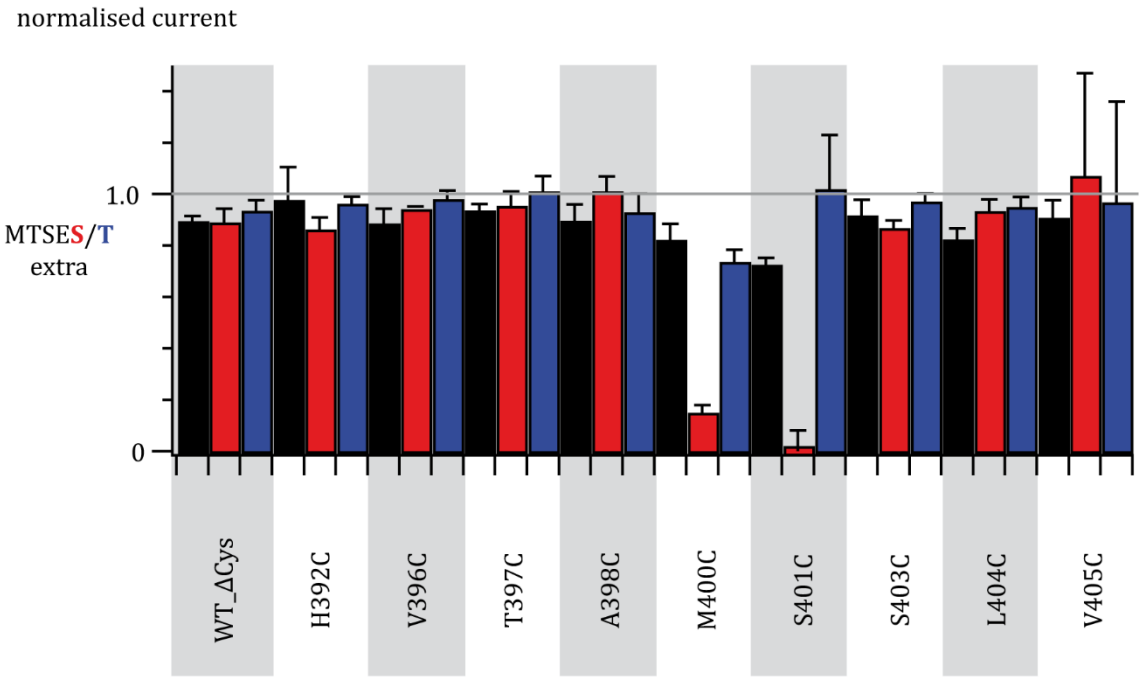

Figure 3.34: Summary of the effects of extracellularly applied MTS on zebrafish prestin constructs with mutations within TM 10. Bars represent the mean of five measurements (n=5) ± SEM. Black bars are the control measurements without MTS application, red bars are measurements with MTSES application and blue bars are measurements with MTSET application. The bar diagram shows the changes of the normalised transport currents on extracellular MTS application.

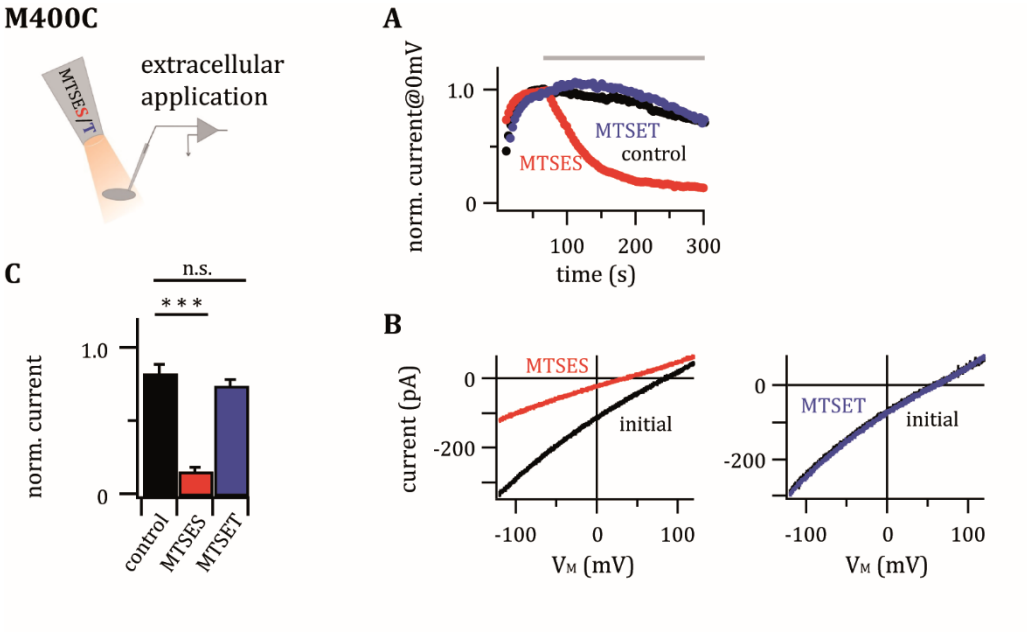

Figure 3.35: The effects of extracellular MTS application on zebrafish prestin M400C. A: The upper graph is taken from Figure 3.33. **B:** The lower two graphs are single traces from the upper graphs: the initial trace (black) is a trace before the application of the MTS reagents was started and the red (MTSES) and blue (MTSET) traces are single representative traces from a time point during the MTS application with a fully established effect. **C:** The bar diagram shows the average effect based on five measurements (n=5) with SEM for changes in the transport currents as normalised values.

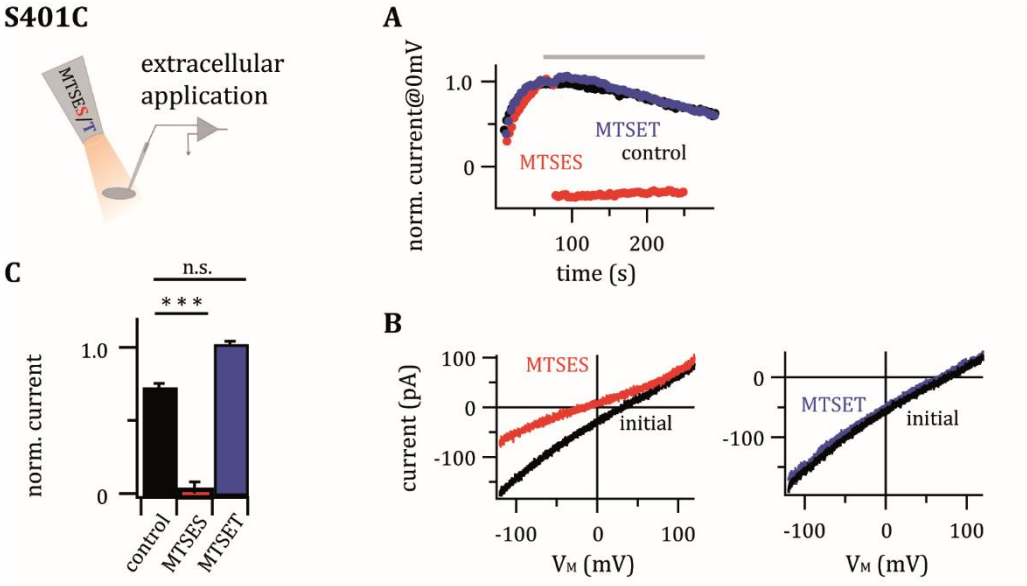

Figure 3.36: The effects of extracellular MTS application on zebrafish prestin S401C. A: The upper graph is taken from Figure 3.33. **B:** The lower two graphs are single traces from the upper graphs: the initial trace (black) is a trace before the application of the MTS reagents was started and the red (MTSES) and blue (MTSET) traces are single representative traces from a time point during the MTS application with a fully established effect. **C:** The bar diagram shows the average effect based on five measurements (n=5) with SEM for changes in the transport currents as normalised values.

3.3.7 Intracellular accessibility of positions within TM 10 in zebrafish prestin

In Figure 3.37 representative normalised transport currents show the effects of intracellular MTS application on zebrafish prestin constructs with mutations within transmembrane domain 10 and Figure 3.38 summarises the average (± SEM) of five independent measurements for each mutant.

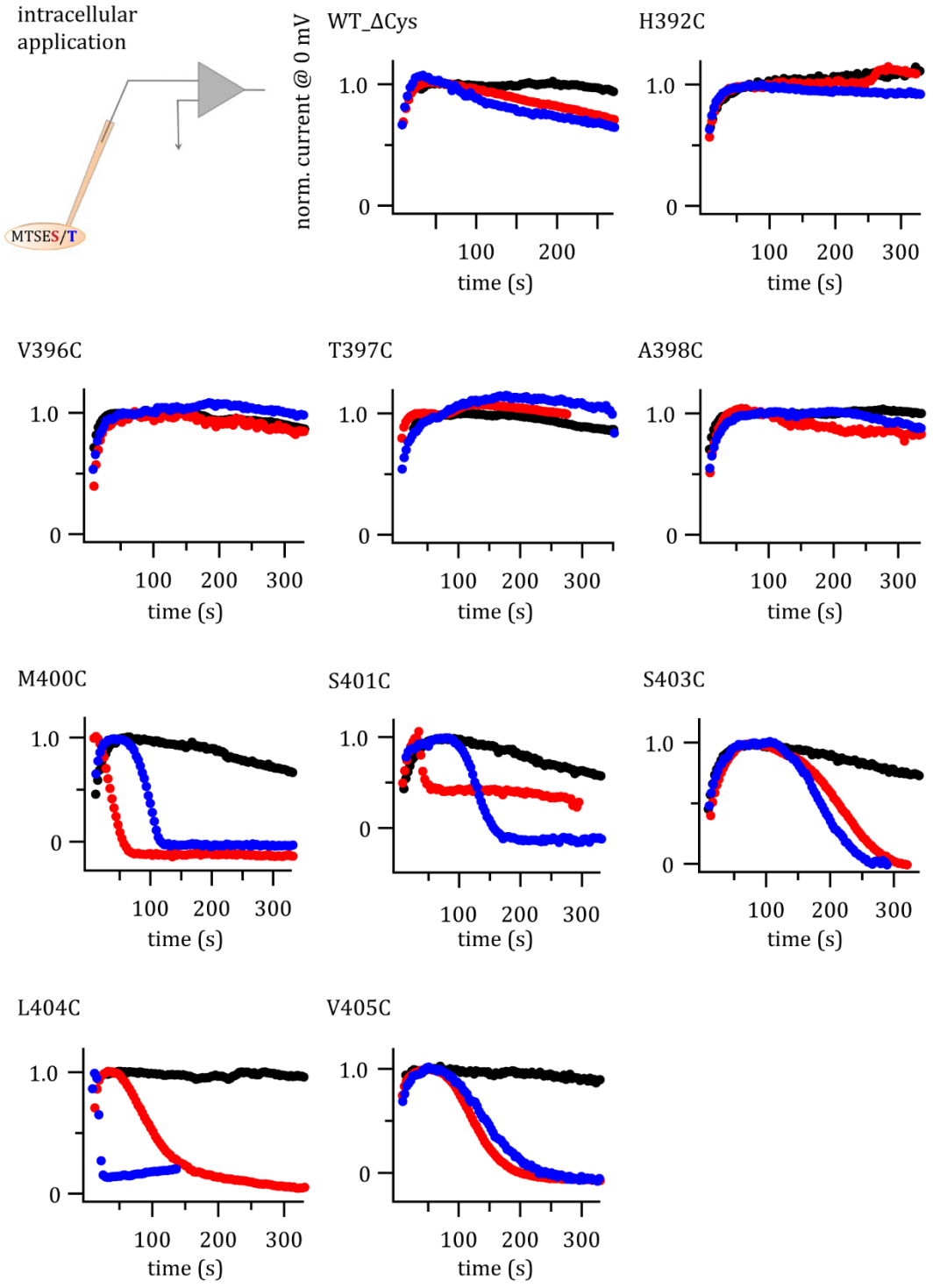

Figure 3.37: The effects of intracellularly applied MTS reagents on the transport currents of the zebrafish prestin constructs with mutations within TM 10. WT_△Cys is the basic construct with nearly all cysteines mutated to alanines (cf. 2.4). All traces show transport currents of a representative measurement and were normalised. In black: a control measurement without application of MTS reagents. In red: a measurement with intracellularly applied MTSES. In blue: a measurement with intracellularly applied MTSET.

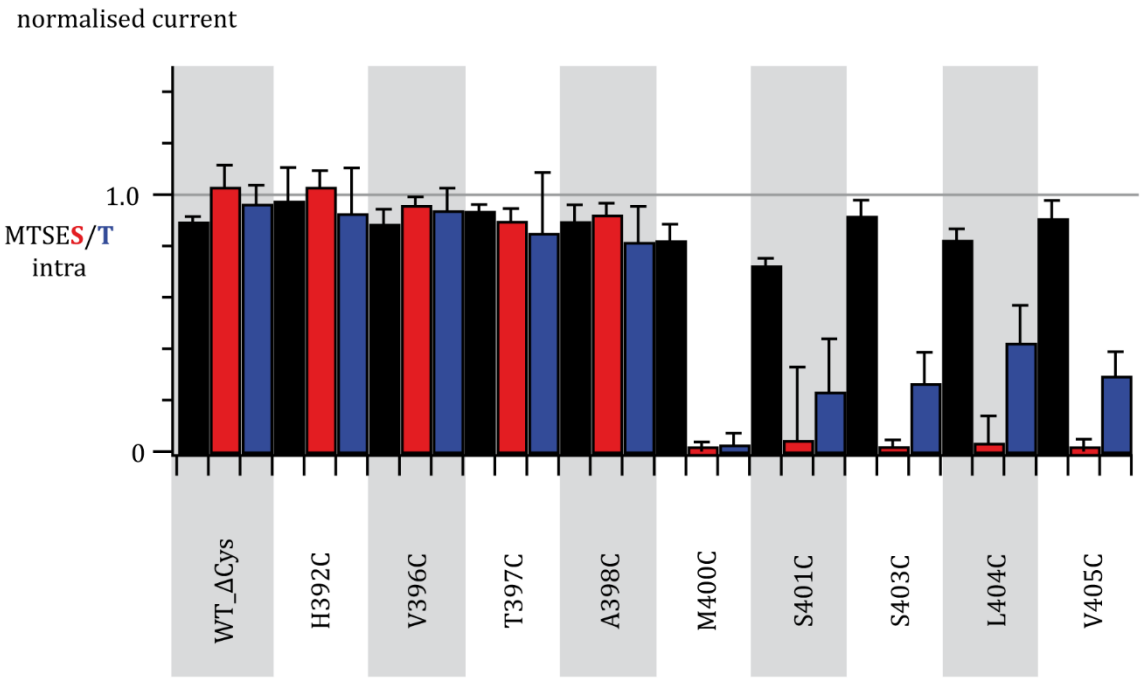

Figure 3.38: Summary of the effects of intracellularly applied MTS on zebrafish prestin constructs with mutations within TM 10. Bars represent the mean of five measurements (n=5) ± SEM. Black bars are the control measurements without MTS application, red bars are measurements with MTSES application and blue bars are measurements with MTSET application. The bar diagram shows the changes of the normalised transport currents on intracellular MTS application.

Five mutants (M400C, S401C, S403C, L404C and V405C) showed an effect upon intracellular presentation of MTSES and MTSET. Detailed data for these MTS-sensitive mutants are presented in Figure 3.39 to Figure 3.43. The transport currents of the mutant M400C decreased to 19.7 ± 3.3 % of the initial current when the pipette contained MTSES and to 2.8 ± 4.5 % with MTSET (Figure 3.39). A decrease in the transport currents was also found in the mutant S401C (Figure 3.40). MTS application led to a decrease in the transport current to 23.7 ± 22.7 % (MTSES) and to 0 ± 7.3 % (MTSET), respectively.

Similarly, the transport currents of the mutant S403C diminished drastically to 2.1 ± 2.5 % with MTSES and decreased more moderately to 26.6 ± 11.9 % in the presence of MTSET (Figure 3.41).

The effects of intracellular MTS application on the mutant L404C were a decrease of the transport currents to 33.8 ± 10.5 % (MTSES) and to 42.3 ± 14.5 % (MTSET) (Figure 3.42).

The cysteine at position V405 was also modified by the intracellular application of MTS compounds (Figure 3.43). Upon MTSES (MTSET) application the transport currents declined to 12.0 ± 4.8 % (29.5 ± 9.4 %).

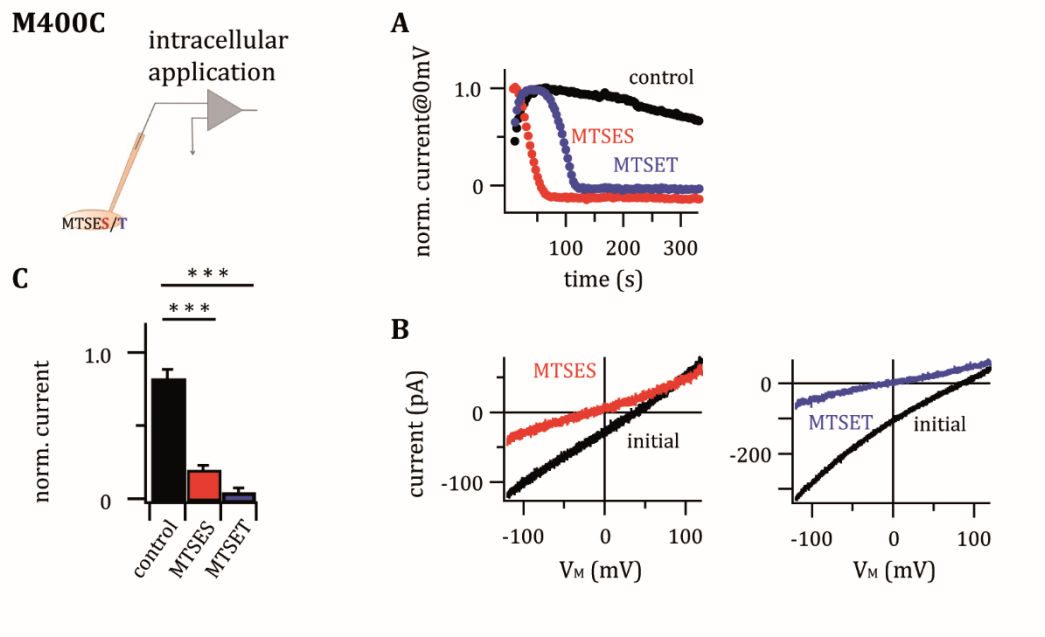

Figure 3.39: The effects of intracellular MTS application on zebrafish prestin M400C. A: The upper graph is taken from Figure 3.37. **B:** The lower two graphs are single traces from the upper graphs: the initial trace (black) is a trace shortly after starting the measurement before a potential effect was distinct and the red (MTSES) and blue (MTSET) traces are single representative traces from a time point towards the end of the measurement with a potentially fully established effect. **C:** The bar diagram shows the average effect based on five measurements (n=5) with SEM for changes in the transport currents as normalised values.

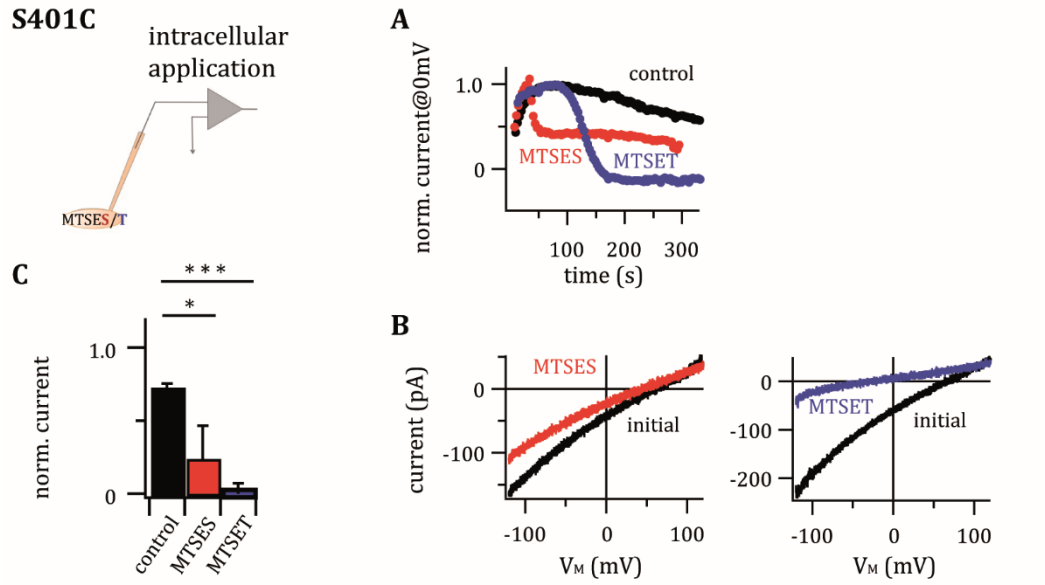

Figure 3.40: The effects of intracellular MTS application on zebrafish prestin S401C. A: The upper graph is taken from Figure 3.37. **B:** The lower two graphs are single traces from the upper graphs: the initial trace (black) is a trace shortly after starting the measurement before a potential effect was distinct and the red (MTSES) and blue (MTSET) traces are single representative traces from a time point towards the end of the measurement with a potentially fully established effect. **C:** The bar diagram shows the average effect based on five measurements (n=5) with SEM for changes in the transport currents as normalised values.

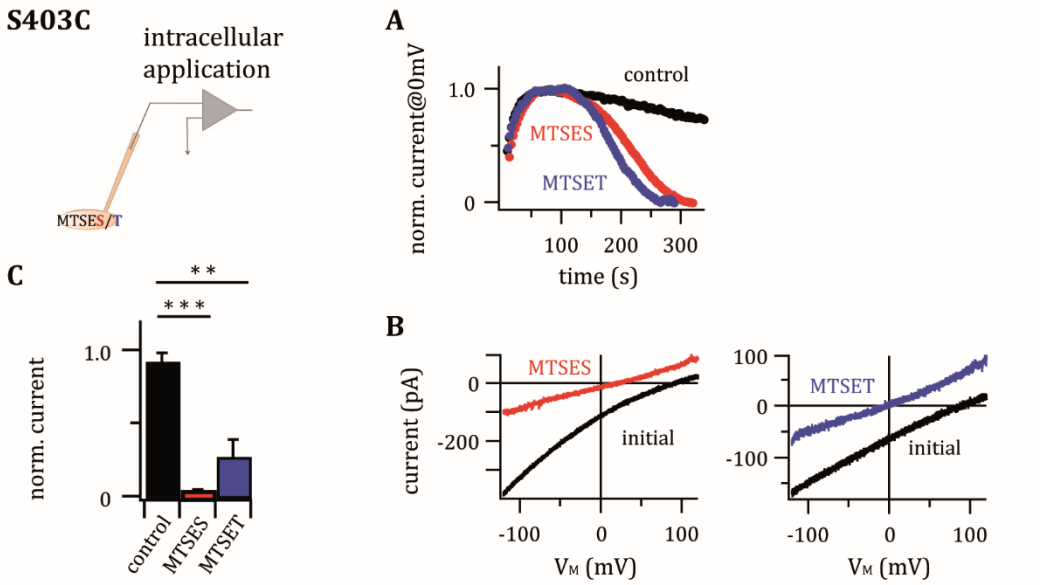

Figure 3.41: The effects of intracellular MTS application on zebrafish prestin S403C. A: The upper graph is taken from Figure 3.37. **B:** The lower two graphs are single traces from the upper graphs: the initial trace (black) is a trace shortly after starting the measurement before a potential effect was distinct and the red (MTSES) and blue (MTSET) traces are single representative traces from a time point towards the end of the measurement with a potentially fully established effect. **C:** The bar diagram shows the average effect based on five measurements (n=5) with SEM for changes in the transport currents as normalised values.

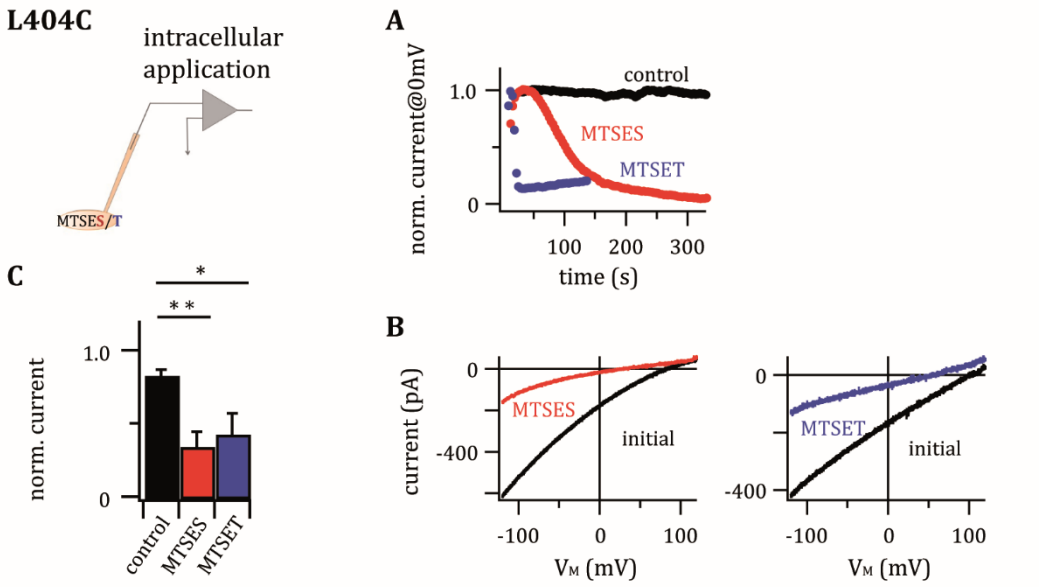

Figure 3.42: The effects of intracellular MTS application on zebrafish prestin L404C. A: The upper graph is taken from Figure 3.37. **B:** The lower two graphs are single traces from the upper graphs: the initial trace (black) is a trace shortly after starting the measurement before a potential effect was distinct and the red (MTSES) and blue (MTSET) traces are single representative traces from a time point towards the end of the measurement with a potentially fully established effect. **C:** The bar diagram shows the average effect based on five measurements (n=5) with SEM for changes in the transport currents as normalised values.

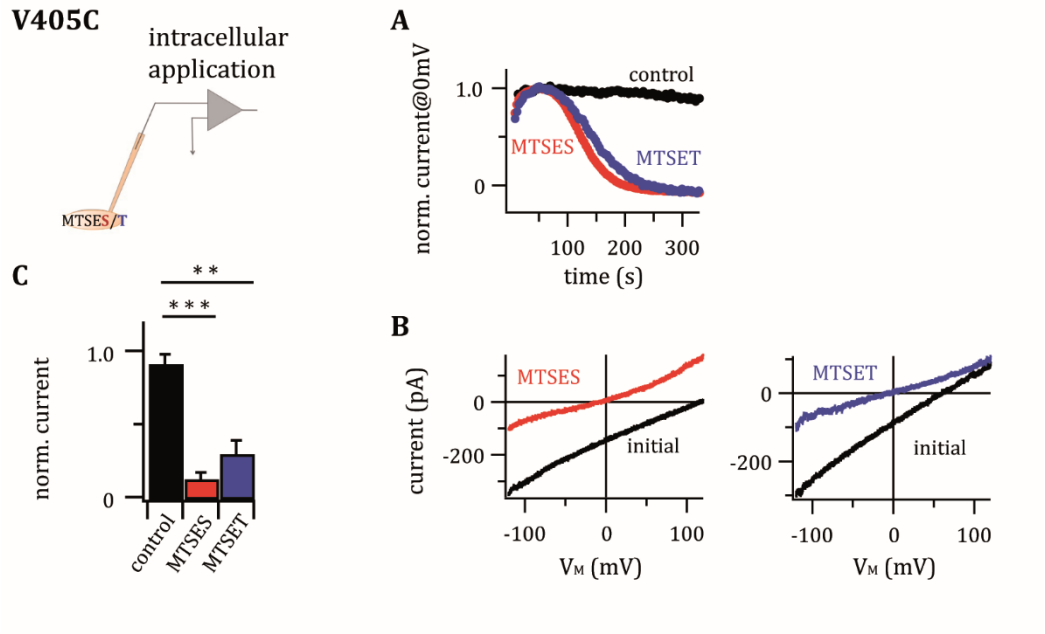

Figure 3.43: The effects of intracellular MTS application on zebrafish prestin V405C. A: The upper graph is taken from Figure 3.37. **B:** The lower two graphs are single traces from the upper graphs: the initial trace (black) is a trace shortly after starting the measurement before a potential effect was distinct and the red (MTSES) and blue (MTSET) traces are single representative traces from a time point towards the end of the measurement with a potentially fully established effect. **C:** The bar diagram shows the average effect based on five measurements (n=5) with SEM for changes in the transport currents as normalised values.

In summary, five positions within transmembrane domain 10 (M400C, S401C, S403C, L404C and V405C) are clearly solute-accessible from the intracellular side.

3.3.8 Summary of cysteine accessibility in TM 10 in zebrafish prestin

Transmembrane domain 10 in zebrafish prestin was investigated from position H392 to V405 except for the positions T393 to V395. The transport currents of two mutants were affected by extracellular application of MTS reagents (cf. Figure 3.34). Upon intracellular application of MTS reagents five mutants showed decreased transport currents (cf. Figure 3.38). Table 3.6 combines all results of positions within transmembrane domain 10. Detailed data obtained for those positions insensitive to MTS reagents, is presented in the supplement (Supplemental figure 7.3).

Table 3.6: Overview of the results of the scanning of zebrafish prestin constructs with mutations within TM 10. Predominant membrane localisation and functionality are marked with + and accordingly cytosolic localisation and lack of functionality with -. Yellow indicates insensitivity (-) to MTS reagents, accessibility from the extracellular side is marked in blue, from the intracellular side in red and additionally with +. Positions with a lack of membrane targeting or functionality were not tested for their accessibility and are therefore not determined (n.d.).

	PM	functional	extracellularly accessible		intracellularly accessible	
			MTSES	MTSET	MTSES	MTSET
H392	+	+	—	—	—	—
			—			
V396	+	+	—	—	—	—
T397	+	+	—	—	—	—
A398	+	+	—	—	—	—
S399	+	—	n.d.	n.d.	n.d.	n.d.
M400	+	+	+	—	+	+
S401	+	+	+	—	+	+
R402	+	—	n.d.	n.d.	n.d.	n.d.
S403	+	+	—	—	+	+
L404	+	+	—	—	+	+
V405	+	+	—	—	+	+

Figure 3.44 depicts the accessibilities of positions within transmembrane domain 10 in zebrafish prestin mapped onto the structural homology model. The two positions (M400 and S401) that turned out to be accessible from the intracellular as well as from the extracellular side are highlighted in purple.

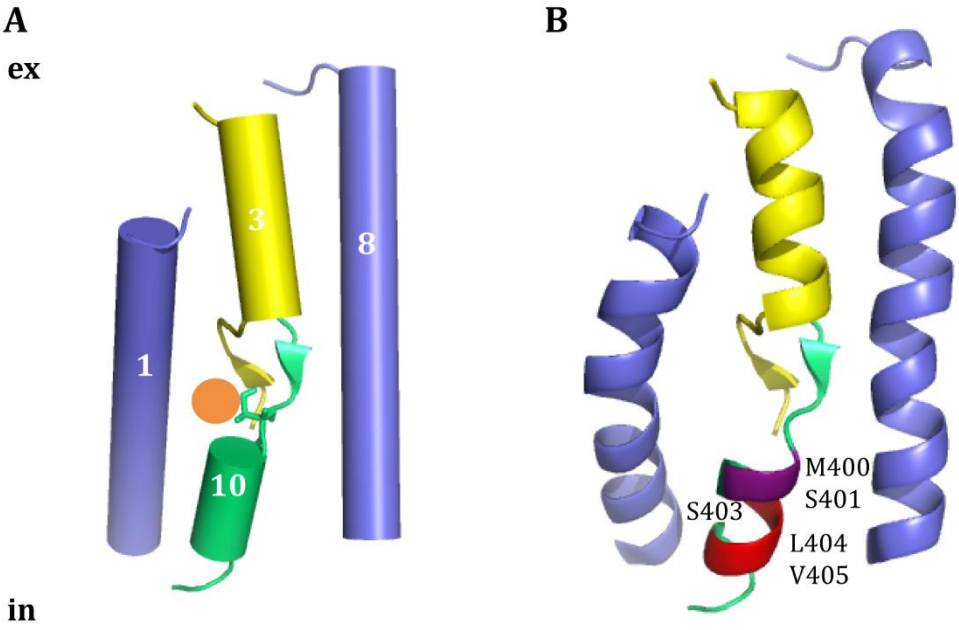

Figure 3.44: Parts of the structural homology model of zebrafish prestin based on UraA with the TMs 1, 3, 8 and 10. TM 3 is shown in yellow, TM 10 in green and the putative anion-binding site (S399 in zebrafish prestin) is shown as sticks. **A:** The orange circle represents a bound anion at the presumptive anion-binding site. **B**: The model is expanded for accessibility results of TM 10. The model shows the presumptive structural localisation of positions that were accessible from the extracellular (blue) side, from the intracellular (red) side or double accessible (purple). The model is based on the results of Gorbunov et al., 2014.

3.4 V139C in rat prestin confers mechanical sensitivity

In the course of the accessibility study of the third transmembrane domain, position V139 in rat prestin turned out to be of special interest. V139 is predicted at the inner end of the transmembrane domain 3 helix. The rat prestin mutant V139C was sensitive to MTS reagents applied from the extra- as well as intracellular side of the cell (Figure 3.12 and Figure 3.20).

The setup for these experiments was the same as for the scanning measurements. An application needle connected with a perfusion system was closely placed to the patched cell. While the measurement was performed, it was possible to start and stop the additional fluid-flow via the application system. The applied fluid was the standard bath solution (unless mentioned otherwise).

Unexpectedly, the rat prestin mutant V139C showed mechanosensitive properties not observed with the wild type protein. Thus, fluid-flow applied to the cell strongly increased NLC amplitude, whereas NLC was minimal in the absence of such mechanical stimulation (Figure 3.45 **A**). In contrast, in wild type prestin presence or absence of fluid-flow had no effect on the NLC other than a minimal shift of the voltage-dependence ($V_{1/2}$).

Since the mutant V139C was originally generated for the cysteine accessibility scanning, it was based on the cysteine-free rat prestin construct with all cysteines mutated to alanines as described before (cf. 2.4 and 7.1.1). In order to characterise and potentially understand the unexpected gain of mechanosensitivity, wild type and the cysteine-free mutant as well as the mutation V139C in both backgrounds (WT and WT_△Cys) were investigated for their flow-dependency of activity (Figure 3.45 **B**).

There was no effect on the NLC peak amplitude upon applied fluid-flow in the two controls of rat prestin (WT and WT_△Cys), neither in the wild type (104.0 ± 2.0 %) nor in the cysteine-free mutant (99.8 ± 1.6 %). Only the wild type protein exhibited mechanical sensitivity in form of a slight shift of the $V_{1/2}$ in the hyperpolarised direction in the absence of fluid-flow. Thus, the mechanosensitivity was not the result of mutation of all native cysteines to alanines. For this reason, only the wild type prestin was investigated as the control construct in the further experiments. Furthermore, the two variants with the V139C mutation also behaved comparably and showed a similar decrease of the NLC peak amplitude in the absence of fluid-flow (V139C (WT): 28.1 ± 9.9 %; V139C (WT_△Cys): 40.0 ± 3.7 %). Because some of the experiments were already performed with the mutant V139C (WT_△Cys), all further experiments were also carried out with this construct (in the following referred to as V139C).

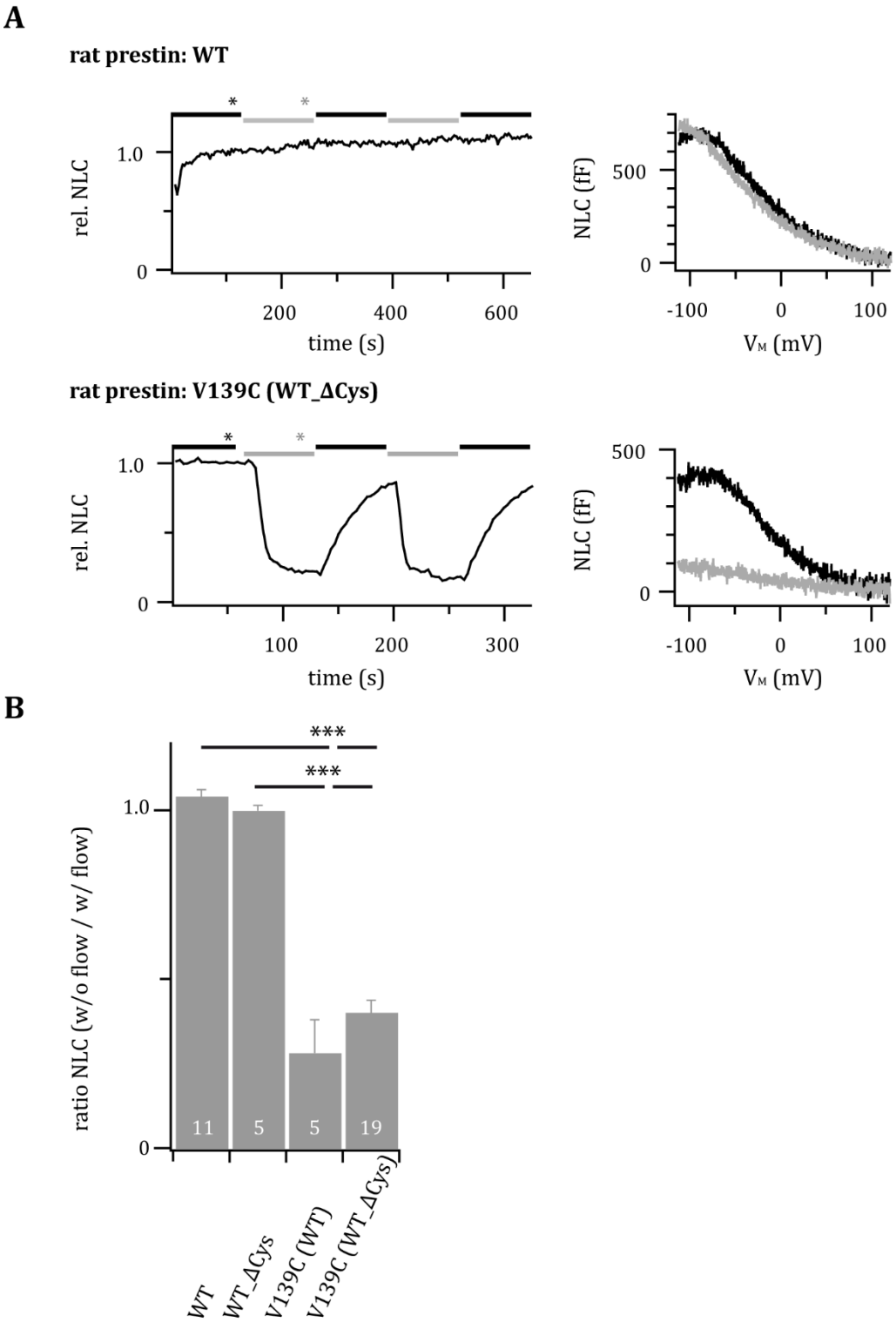

Figure 3.45: Mechanosensitive properties of rat prestin wild type and V139C. A: The upper graphs are representative measurements of rat prestin wild type (WT), the lower graphs of rat prestin V139C (WT_△Cys). Left graphs show the normalised NLC peak amplitude. Black bars and traces indicate periods with fluid-flow while grey bars and traces indicate the absence of fluid-flow. The traces were normalised to a trace under fluid-flow condition around one minute after starting the measurement (additionally marked by the black asterisks). Furthermore, the asterisks mark the positions of the representative traces shown in the right graphs. **C:** Comparison of the flow-dependent effect in different variants of rat prestin. The effect of applied fluid-flow was tested in WT, WT_△Cys and the mutants V139C (WT) and V139C (WT_△Cys). The average effect on the NLC peak amplitude is shown. The number of measurements for each condition is indicated. Mean ±SEM.

To examine the possibility of a cell type-dependent phenomenon to CHO cells, the mutant was further tested for flow-dependency of activity in HEK 293 cells. In both different cell lines, the same effect could be observed (Figure 3.46). The NLC peak amplitude decreased (relative to the amplitude in flow-condition) to 40.0 ± 3.7 % in CHO cells and to 45.5 ± 4.7 % in HEK 293 cells in the absence of fluid-flow.

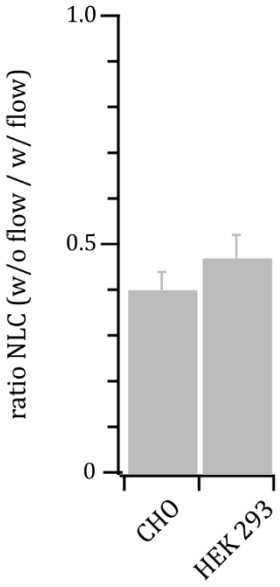

Figure 3.46: Comparison of the mechanosensitive properties in different cell lines. CHO cells: n=19 and HEK 293 cells: n=4. Mean ± SEM.

Next it was tested, whether mechanical sensitivity was also induced by other amino acid substitutions at the position V139. In fact, all SLC26 isoforms have either a valine or isoleucine residue at the structurally homologous position, suggesting an important structural or functional role of such a hydrophobic amino acid at this position. Thus, different substitutions of valine for other amino acids were explored for flow-dependent behaviour. Substituting V139 by isoleucine (or leucine) did not confer mechanical sensitivity (Figure 3.47). Alanine and glycine are also nonpolar and small amino acids, whereas tryptophan and proline are nonpolar but bulky. As found for isoleucine and leucine, all these exchanges did not result in flow-dependency of activity. Interestingly, even the mutation to serine, which is the isosteric replacement of cysteine, did not induce flow-dependent behaviour. Mutations to arginine (basic) and to glutamate (acidic) led to proteins not targeted to the cell membrane, that, therefore, could not be studied. Thus, the flow-dependency of activity was exclusively induced by the exchange of valine to cysteine.

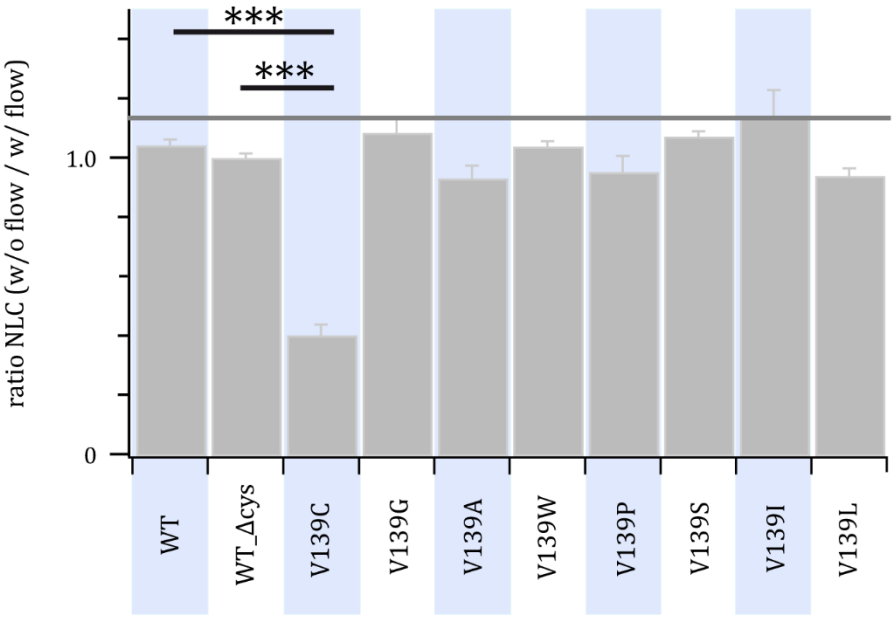

Figure 3.47: Mechanosensitive properties in rat prestin were exclusively mediated by V139C. The cysteine-free (WT_△Cys) variant of rat prestin served as the basic construct for all mutations at V139. A significant decrease of the NLC peak amplitude in the absence of fluid-flow was only observed in the mutant V139C. The differences of this effect were highly significant only between the basic constructs (WT and WT_△Cys) and the mutant V139C but not the other mutants. n≥3. Mean ± SEM.

3.4.1 A common behaviour within the SLC26 transporter family upon applied fluid-flow

To test whether a mechanical sensitivity could also be induced in a transport-capable prestin, the structurally homologous position to rat prestin V139 was mutated to cysteine in zebrafish prestin (V140C). Interestingly, the activity of zebrafish prestin V140C was also dependent on flow-application. In the absence of fluid-flow the transport current drastically decreased, similar to the decrease of the NLC peak amplitude in rat prestin V139C, whereas the transport current of zebrafish prestin wild type was not affected by applied fluid-flow (Figure 3.48 **A**).

As for rat prestin, the mechanosensitivity of the four variants of zebrafish prestin was compared between native and cysteine-free constructs, namely the wild type (WT), the nearly cysteine-free variant (WT_△Cys) (cf. 7.1.2) and V140C in both backgrounds. As shown in Figure 3.48 **B** both zebrafish prestin wild type and the nearly cysteine-free variant were insensitive to fluid-flow as no change of the transport current size was observed when fluid-flow was stalled (WT: 93.4 ± 4.4 %; WT_△Cys: 93.6 ± 9.1 %). In contrast, the mutation of V140 to cysteine caused a decrease of the transport current upon the switch-off of fluid-flow (V140C (WT): 18.3 ± 4.8 %; V140C (WT_△Cys): 29.0 ± 11.1 %).

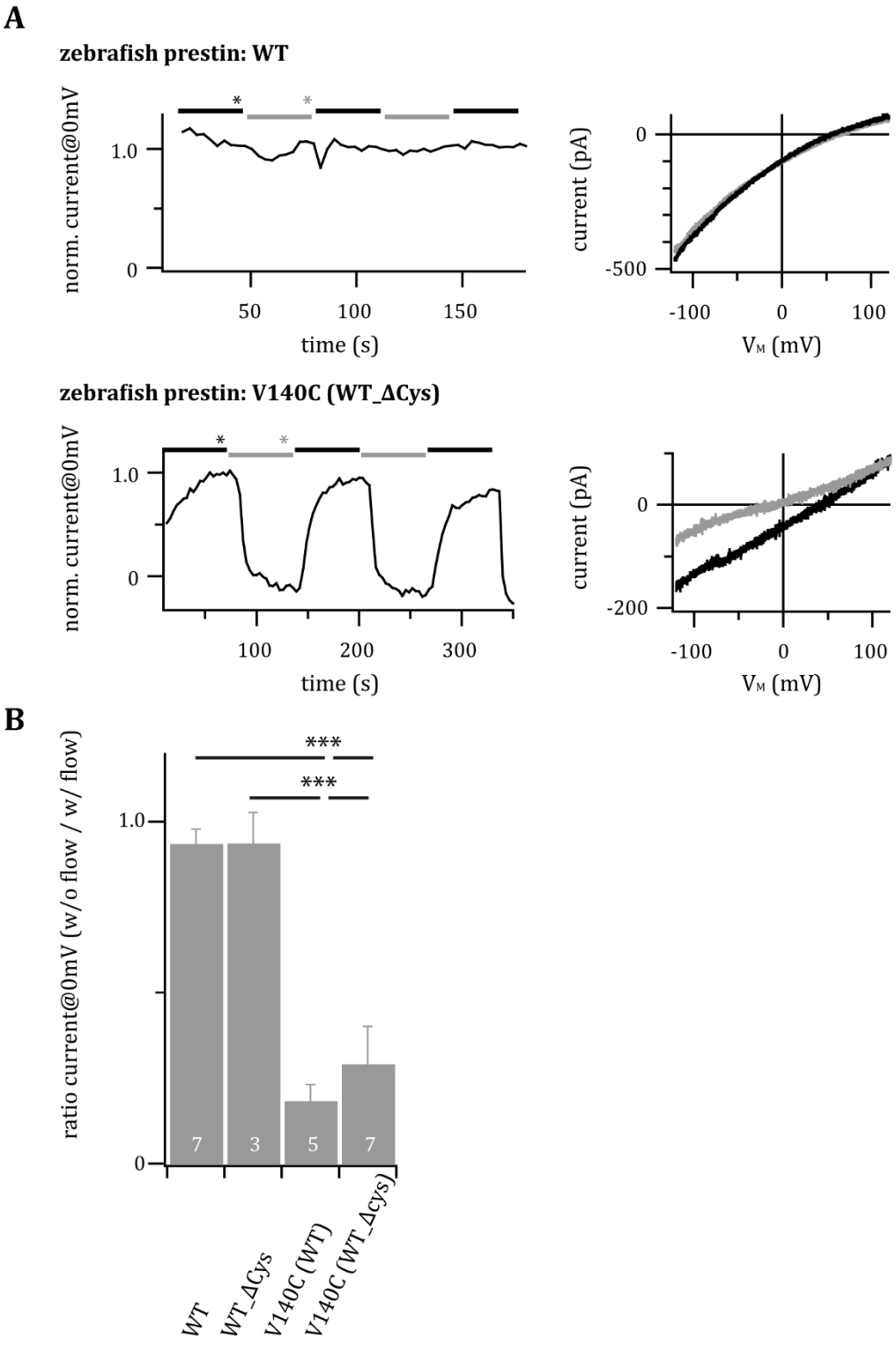

Figure 3.48: Flow-application affected transport currents of zebrafish prestin V140C. A: The left graphs show normalised transport currents at 0 mV of WT and V140C (WT_△Cys), respectively. Individual representative current traces are shown in the right panels. Black bars and traces: with fluid-flow; grey bars and traces: without fluid-flow. The traces were normalised to a trace under fluid-flow condition around one minute after starting the measurement with stable representative values (additionally marked by the black asterisks). The asterisks also mark the positions of the representative traces. The pipette solution contained 10mM or 106 mM sodium oxalate for measurements in wild type or V140C, respectively. **B:** The effect of fluid-flow was tested in two controls, namely the wild type (WT) and the nearly cysteine-free variant (WT_△Cys), and the mutants V140C (WT) and V140C (WT_△Cys). In the bar diagram, the average effects on the transport currents are shown. The number of measurements for each condition is indicated. Mean ±SEM.

Differences between the two controls (WT and WT_△Cys) as well as differences between the two V140C mutants were not statistically significant, whereas flow-dependent current changes were highly significant for each V140C mutant. For all further experiments in zebrafish prestin, the wild type construct and the mutant V140C (WT) were used.

3.4.2 Effects of changes of extracellular osmolarity on rat prestin V139C

The flow-dependency of activity of rat prestin V139C points to increased mechanosensitive properties of mutated prestin. But the nature of the relevant mechanical stimulus was yet to be characterised further. What does the application of fluid-flow cause? Is it membrane tension or something else, e.g. shear stress? Membrane tension appeared to be an attractive explanation, given that the area motor mechanism implies a fundamental dependence of state-occupancy on membrane tension even in native prestin (Dong & Iwasa, 2004).

Adjusting the osmolarity of recording solutions is one of the standard strategies to test for tension sensitivity of transmembrane proteins, as resulting water fluxes alter cell volume and hence membrane stretch. Therefore, the extracellular bath solution was adjusted to different osmolarities, i.e. hypo- and hypertonic solutions.

Application of these solutions stressed cells, which could be observed by swelling and shrinking of the cells, respectively. However, challenging the cell with different osmolarities did not reproduce the effect of fluid-flow described above for rat prestin V139C (Figure 3.49).

Exchange of either hypotonic or hypertonic solution for the iso-osmotic standard bath solution (310 mOsm/kg) had no significant effect on the NLC peak amplitude in either wild type prestin or the V139C mutant, whereas in the same cells, changes in fluid-flow (stalling of flow) yielded the same reduction of the NLC described above for the mutant, but not for wild type prestin (Figure 3.49 **A** and **B**). Voltage dependence was only slightly and inconsistently affected in both wild type and V139C prestin (Figure 3.49 **B**).

These findings thus do not support a role of membrane tension in the flow dependency of activity in the mutant V139C.

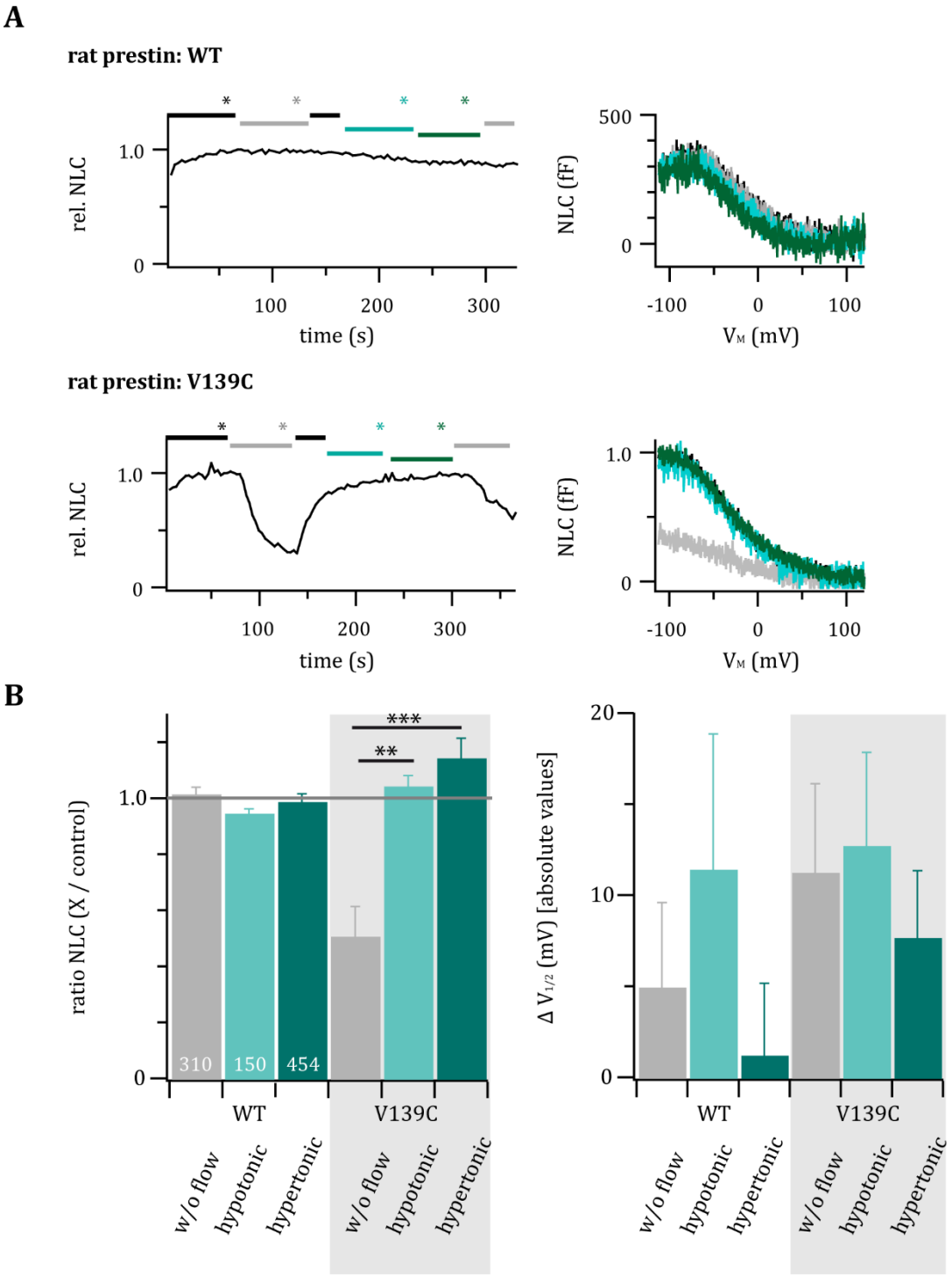

Figure 3.49: Different osmolarities did not reproduce mechanical sensitivity in rat prestin V139C. A: The upper graphs are representative measurements of rat prestin wild type, the lower graphs of rat prestin V139C. Left graphs show the normalised NLC peak amplitude. The right graphs show corresponding representative traces. Black bars and traces: with fluid-flow; grey bars and traces: without fluid-flow; turquoise bars and traces: application of hypotonic solution (150 mOsm/kg); dark green bars and traces: application of hypertonic solution (454 mOsm/kg). The traces were normalised to a trace under fluid-flow condition around one minute after starting the measurement with stable representative values (additionally marked by the black asterisks). Furthermore, the asterisks mark the positions of the representative traces shown in the right graphs. **B:** The bar diagrams sum up the effects on the NLC peak amplitude and on the $V_{1/2}$. The denoted ratios are for a mean of five representative traces under condition X (X=without fluid-flow, under application of hypo- or hypertonic solution) compared with a mean of five representative traces with fluid-flow. The osmolarity of the bath solution is indicated in the first three bars on the left diagram. n≥3. Mean ± SEM.

Prestin is organised in cholesterol-rich membrane microdomains (Rajagopalan et al., 2006; Sturm et al., 2007). It appeared possible that membrane tension changes as induced by osmotic challenge might not transmit into these possibly rigid domains, which could explain the absence of any effect of osmotic stimuli on activity of V139C. It was reported that extraction of cholesterol from the membrane by methyl-ß-cyclodextrin (MßCD) released prestin from the microdomains. Therefore, the effect of osmotic challenge on the mutant's activity after MßCD treatment was tested.

After preincubation with 10 mM MßCD most cells were roundish and a shift of $V_{1/2}$ of V139C was seen as described for wild type (Rajagopalan et al., 2007). When fluid-flow was abolished, NLC peak amplitude was still significantly decreased as shown in Figure 3.50 **A**.

After depletion of cholesterol by MßCD, NLC amplitudes of both V139C and wild type prestin remained unaffected by osmotic challenge (Figure 3.50 **B**). However, under these conditions a significant shift of the voltage dependence (as quantified by $V_{1/2}$) was obvious for both prestin variants. Although this observation supports an increased exposure of prestin to membrane tension after dissociation of the cholesterol-dependent microdomains, at the same time, it argues against a role of tension in the flow-dependency of activity, since no changes of NLC amplitude (the hallmark of flow-dependency) were found, and the $V_{1/2}$ shifted in a similar way in the mutant and wild type.

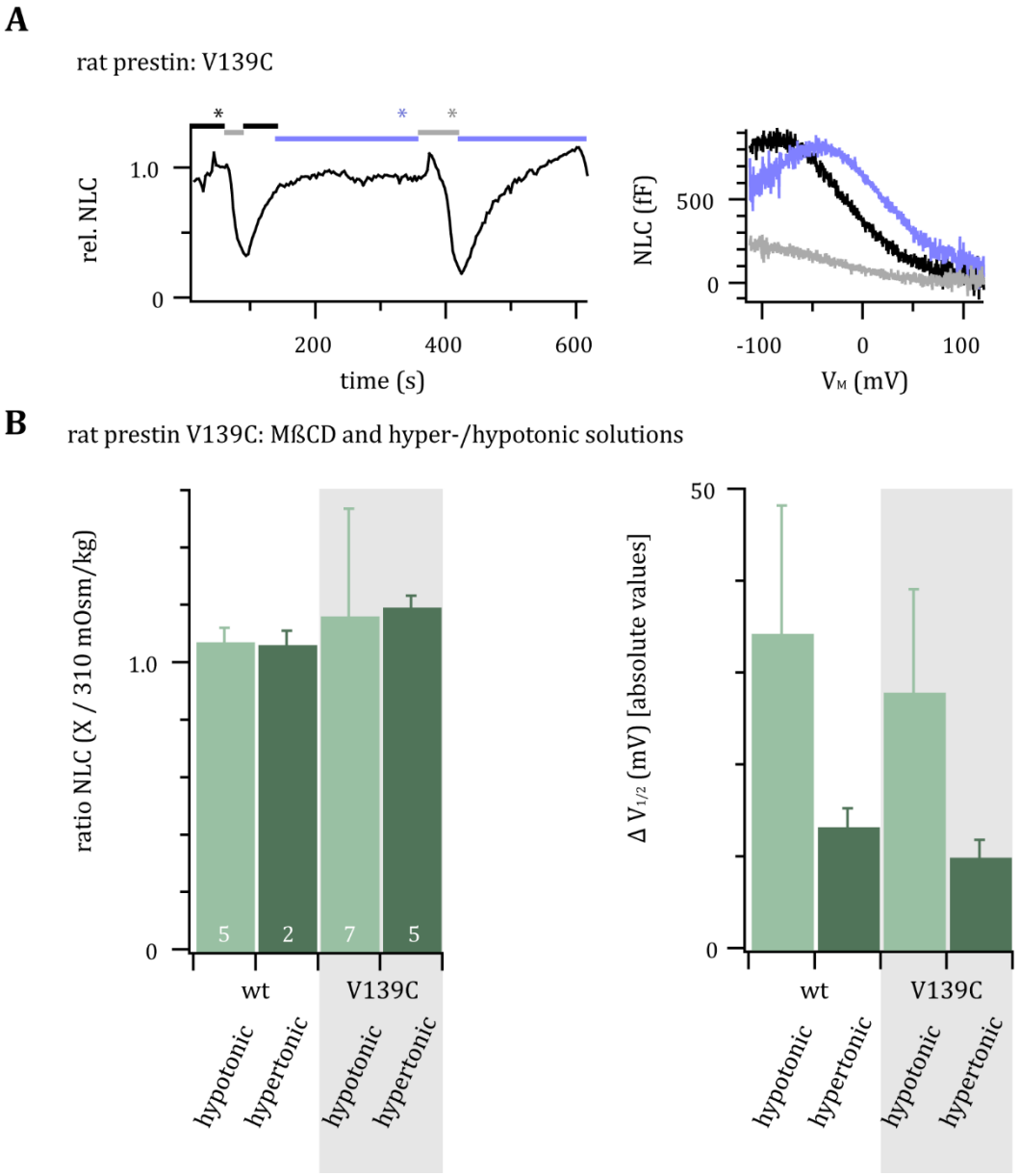

Figure 3.50: Pretreatment with MßCD shifted the $V_{1/2}$ but did not induce mechanical sensitivity provoked by different osmolarities. A: 10 mM MßCD was applied during whole cell recordings. Left graph: NLC peak amplitude was normalised to a representative trace with stable values under flow condition (marked by the black asterisk). Black bars and trace: with fluid-flow; grey bars and trace: without fluid-flow; blue bars and trace: application of MßCD (10 mM). The right graph shows corresponding representative traces. The asterisks mark the positions of the representative traces. The application of MßCD (10 mM) shifted the $V_{1/2}$ to more positive values, but it affected neither the NLC peak amplitude nor its decrease during non-flow conditions. **B:** After incubation with MßCD (10mM) for about 10 minutes the fluid-flow was applied to cells transfected with rat prestin wild type (WT) or V139C. Cells were measured with the standard bath solution (310mOsm/kg) as well as hypotonic (198 mOsm/kg; light green) or hypertonic (398 mOsm/kg; dark green) bath solutions. The left bar diagram shows the average ratio (X=hypotonic or hypertonic solution, respectively) of the NLC peak amplitude, the right diagram the average changes of the $V_{1/2}$ as absolute values. The number of measurements for each condition is indicated. Mean ± SEM.

3.4.3 No interaction of V139C with the cytoskeleton to induce mechanical sensitivity

Since experiments with osmotic challenge did not point to a direct role of membrane tension in the flow-dependency of activity of V139C, alternative mechanisms had to be considered.

By its tight association with the plasma membrane, the cytoskeleton is involved in cellular mechanosensing as well as in exerting force onto the membrane (Ohashi et al., 2017). Therefore, it was next analysed whether the cytoskeleton could play a role in mediating mechanosensitivity of the V139C mutant.

Latrunculin A inhibits actin polymerisation by binding to actin monomers and thereby effectively dissociates cellular F-actin structures (Coué et al., 1987). Pretreatment for 30 minutes with 5 µM Latrunculin A induced cell rounding, confirming its activity. However, the mechanosensitivity of V139C was not affected (Figure 3.51). The NLC peak amplitude decreased to 41.1 ± 1.3 % (n=2) upon stalling of fluid-flow, quantitatively not different from the control conditions described above. In consequence, the involvement of the cytoskeleton in mechanosensitivity of the mutant V139C could be excluded.

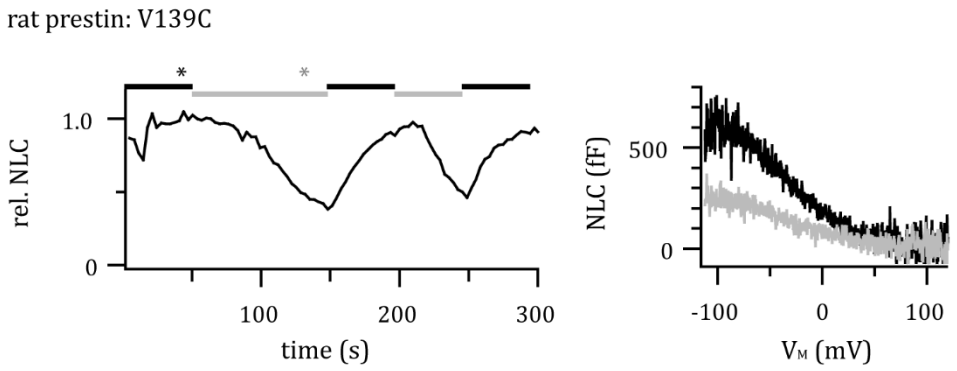

Figure 3.51: The actin modulator Latrunculin A did not affect the mechanosensitive activity of rat prestin V139C. Cells were treated with 5 µM Latrunculin A for 30 min before recording. The left graph shows the normalised NLC peak amplitude. The measurement was normalised to a representative trace with stable values under flow condition (marked by the black asterisk). Black bars and trace: with fluid-flow; grey bars and trace: without fluid-flow. The right graph shows corresponding representative traces. The asterisks mark the positions of the representative traces.

To further probe for a potential role of other intracellular factors or signalling cascades, the flow-dependency of activity of V139C was studied in excised outside-out patches (Figure 3.52). Measurements were first performed in whole cell mode and subsequently outside-out patches were pulled, allowing determination of mechanosensitivity in both recording conditions from the same cell.

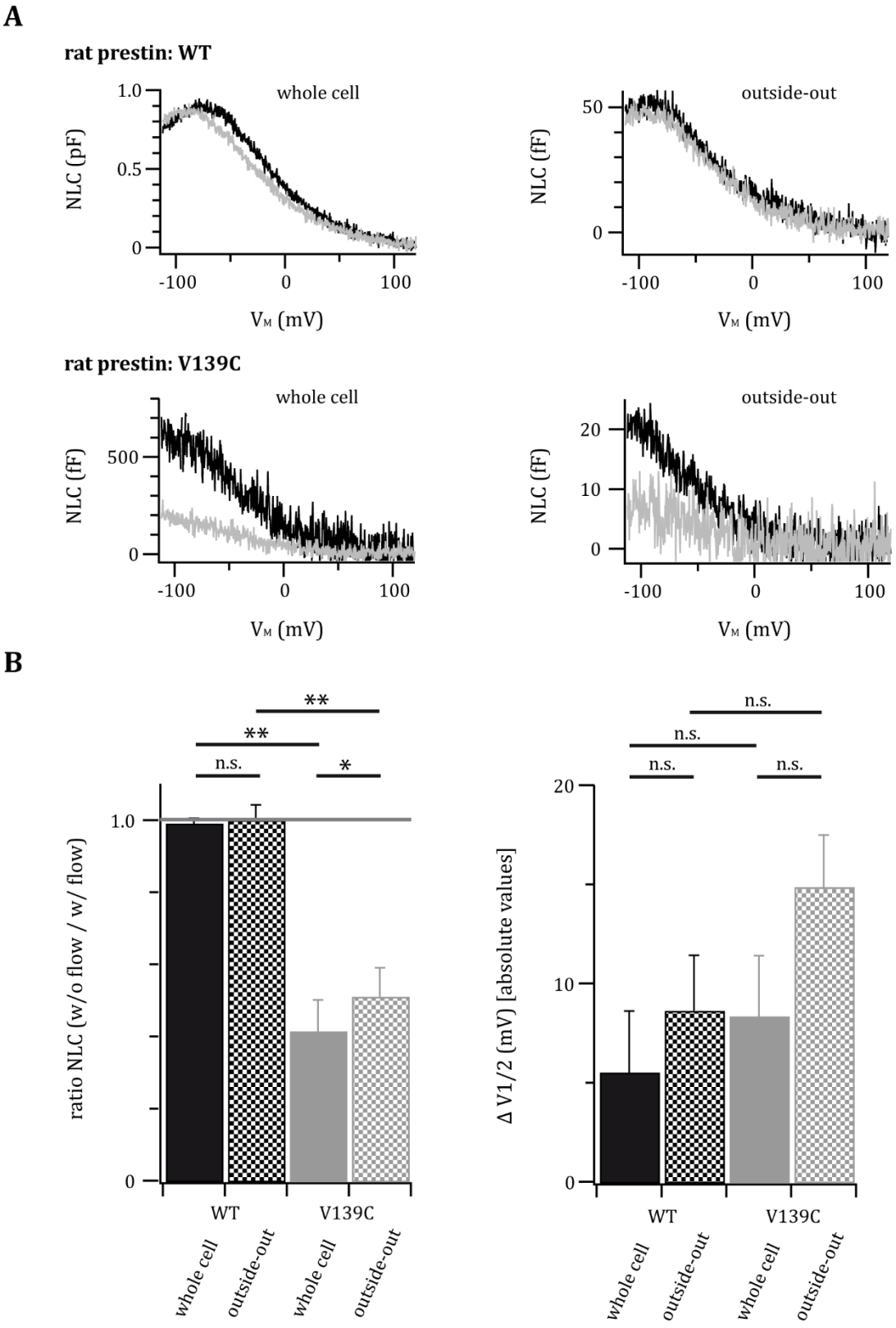

Figure 3.52: Flow-dependency of activity was observed in whole cell and outside-out patches in rat prestin V139C. A: Representative traces of measurements in whole cell (left) and outside-out mode (right) of the same cell transiently transfected with rat prestin wild type (upper graphs) and V139C (lower graphs), respectively. Black traces: w/ fluid-flow; grey traces: w/o fluid-flow. **B:** The left bar diagram shows the average effect on NLC, the right bar diagram changes in $V_{1/2}$. The denoted ratios are for a mean of five representative traces w/o fluid-flow when the effect was fully distinct compared with a mean of five representative traces w/ fluid-flow directly before the effect was initiated by turning off the application of fluid-flow. n≥4. Mean ± SEM.

As shown in Figure 3.52 fluid-flow affected the NLC to the same degree under whole cell and outside-out conditions. Thus, NLC amplitude of rat prestin wild type was not affected by the absence of fluid-flow, neither in the whole cell mode (99.0 ± 1.5 %) nor in outside-out patches (100.0 ± 4.2 %). Importantly, for rat prestin V139C NLC in outside-out mode decreased to 51.0 ± 8.1 %, when the flow was switched off, very similar to the effect in whole cell mode (41.4 ± 8.7 %). Changes in voltage dependence ($V_{1/2}$) were minimal and statistically not significantly different between any of the tested conditions.

In conclusion, the excised-patch experiments suggest that the mechanosensitivity of V139C does not require intracellular factors.

3.4.4 Influence of the redox-state on the flow-dependency

Since the thiol-group of cysteine is known to be sensitive to redox modifications, it was further studied whether the flow-dependency of activity of rat prestin V139C was affected by the application of redox-active substances.

DTT acts on thiol-groups and maintains them in a reduced state. Strikingly, the application of DTT (5 mM) abolished the flow-dependency of activity of rat prestin V139C. Thus, there was no longer a decrease in the NLC peak amplitude in response to turning off the fluid-flow after application of DTT (WT: 102.0 ± 1.8 %; V139C: 96.6 ± 7.0 %). Furthermore, DTT also reduced the flow-dependent shift of the $V_{1/2}$ in rat prestin wild type as shown in Figure 3.53 **A** (WT: -1.35 ± 1.57 mV; V139C: +0.37 ± 1.39 mV). In contrast, application of the oxidising reagent H_2O_2 (150 mM) to convert the thiol-groups into their oxidised form preserved the flow-dependency of activity of V139C (Figure 3.53 **B**). The difference between the case with and without applied fluid-flow was still significant with a decrease to 45.6 ± 2.6 %.

Moreover, the flow-dependent $V_{1/2}$-shift in wild type and in V139C was not affected by application of H_2O_2 (-20.49 ± 4.05 mV and -17.57 ± 5.71 mV, respectively), and comparable with the shifts observed without the preapplication of H_2O_2 (WT: -18.11 ± 4.19 mV; V139C: -13.82 ± 2.08 mV; Figure 3.53 **C**).

A: DTT+ flow

rat prestin: WT

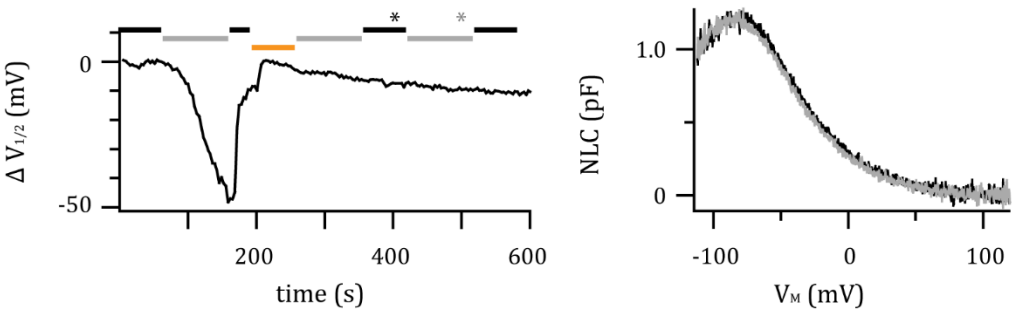

rat prestin: V139C

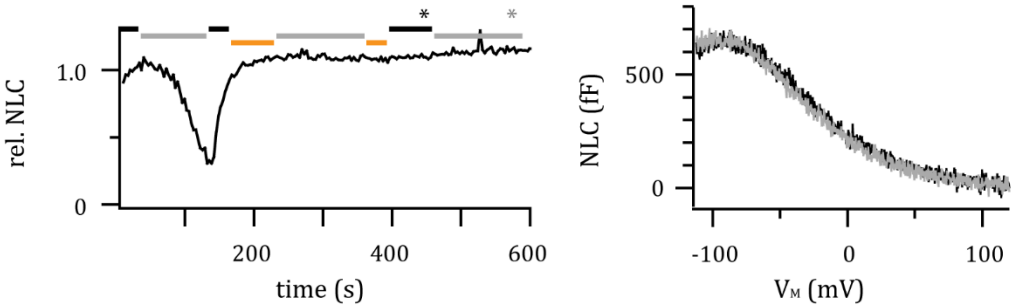

B: H_2O_2 + flow

rat prestin: WT

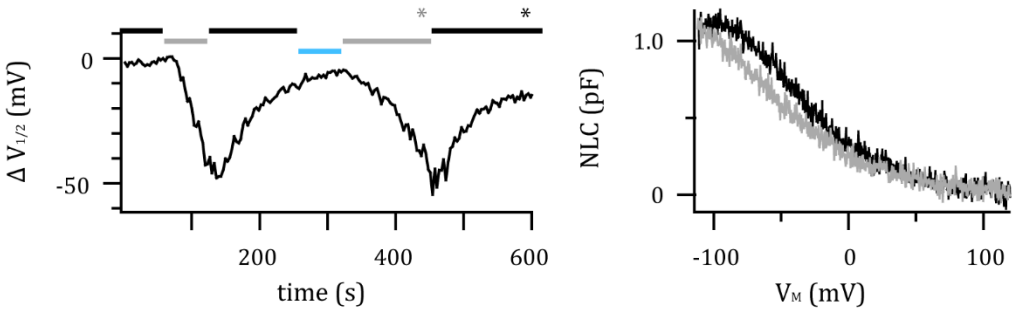

rat prestin: V139C

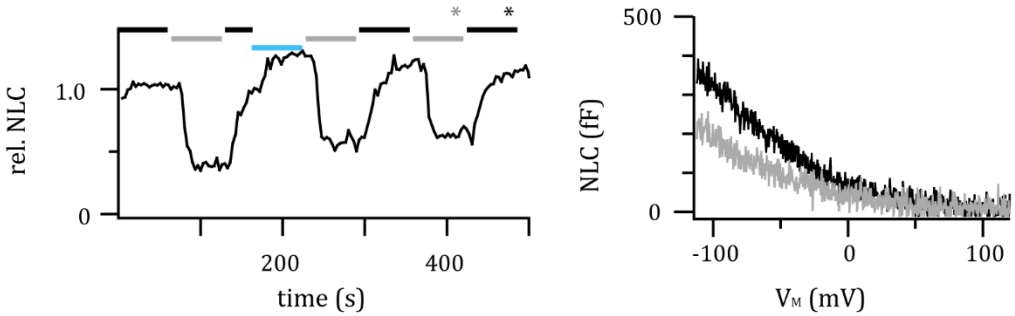

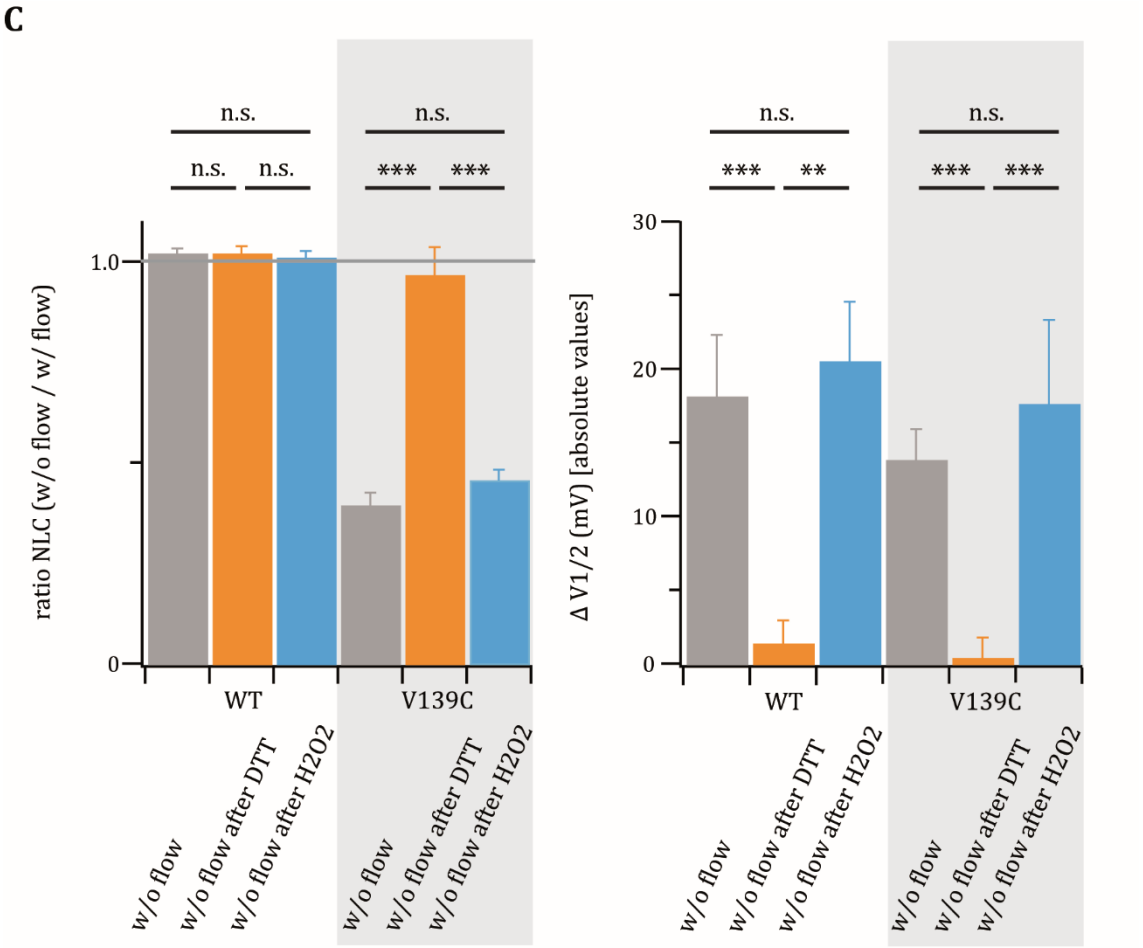

Figure 3.53: Effect of the application of DTT and H_2O_2 on the flow-dependency of activity of rat prestin V139C. A+B: Left graphs show normalised changes of the $V_{1/2}$ (WT) or the normalised NLC (V139C), respectively. The measurements were normalised to a representative trace with stable values under flow condition. Black bars and traces show a condition with fluid-flow, grey bars and traces without fluid-flow, orange bars the application of DTT (5 mM), blue bars the application of H_2O_2 (150 mM). The upper graphs show a representative measurement of WT, the lower graphs of V139C. Asterisks mark the position of the corresponding traces. The right graphs picture corresponding representative traces. **A:** Effect of DTT on the flow-dependency of rat prestin. **B:** Effect of H_2O_2 on the flow-dependency of rat prestin. **C:** The bar diagrams sum up effects of DTT and H_2O_2 on the NLC peak amplitude and $V_{1/2}$. The denoted ratios are for a mean of five representative traces without fluid-flow when the effect was fully distinct compared with a mean of five representative traces with fluid-flow directly before the effect was initiated by turning off the fluid-flow. n≥5. Mean ± SEM.

Equivalent experiments were also performed in zebrafish prestin (Figure 3.54). The effects of the redox agents (DTT and H_2O_2) on flow-sensitivity of anion transport were qualitatively similar to those in rat prestin. However, application of DTT and H_2O_2 immediately and strongly affected the size of transport currents in the zebrafish prestin V140C mutant (DTT: 1026.9 ± 322.8 %; H_2O_2: 30.8 ± 4.5 %) but not in the wild type (DTT: 99.1 ± 1.1 %; H_2O_2: 95.3 ± 1.3 %). This means that the currents were strongly increased by DTT application, but inhibited by H_2O_2 application in V140C in zebrafish prestin. Thus, flow-sensitivity of transport was abolished by DTT application (w/o flow after DTT: 97.7 ± 1.0 % of the current under flow condition), whereas the application of H_2O_2 preserved the decrease of the transport current upon stalling of the flow (w/o flow after H_2O_2: 46.1 ± 18.5 %). In wild type

zebrafish prestin neither DTT nor H_2O_2 affected the insensitivity to fluid-flow on transport currents (w/o flow after DTT: 96.2 ± 1.0 %; w/o flow after H_2O_2: 98.4 ± 2.4 %).

A: DTT+ flow

zebrafish prestin: WT

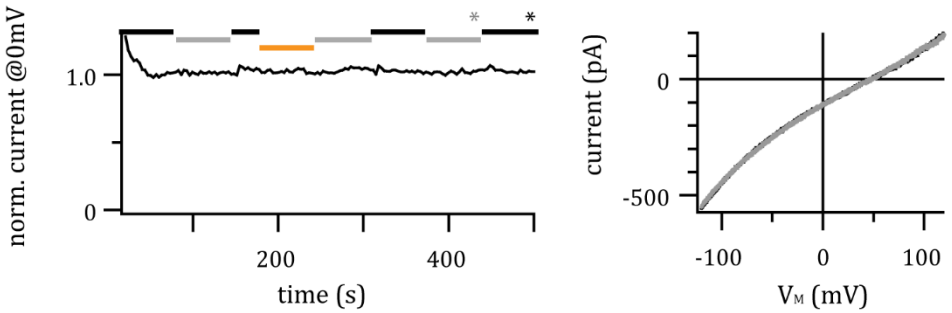

zebrafish prestin: V140C

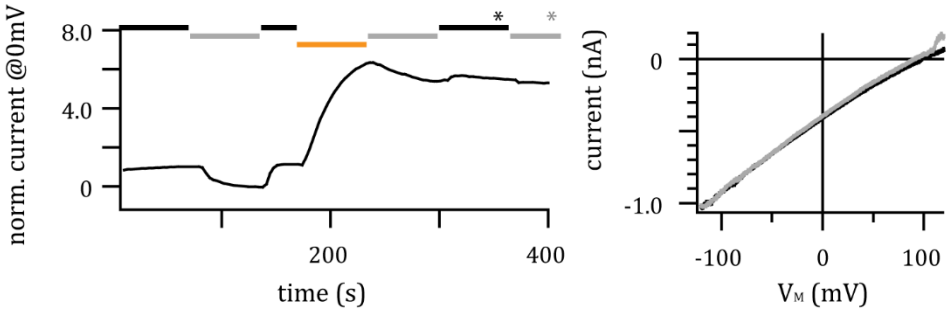

B: H_2O_2 + flow

zebrafish prestin: WT

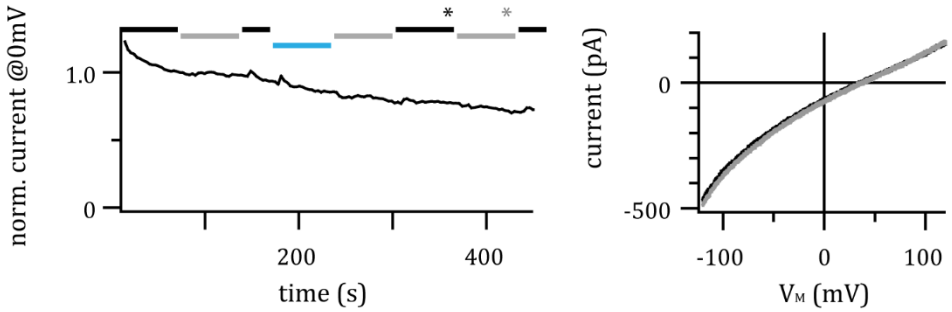

zebrafish prestin: V140C

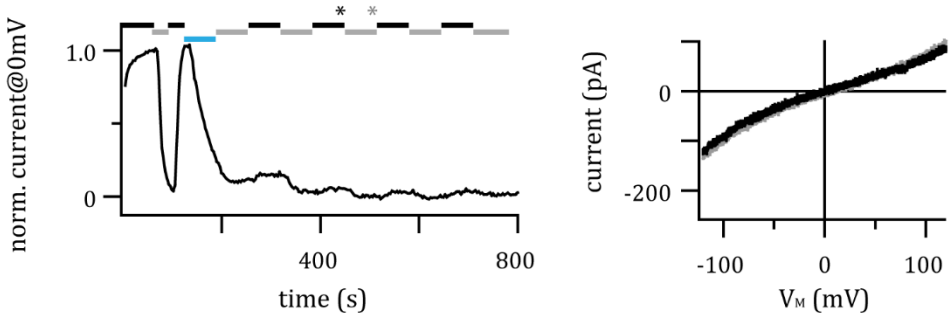

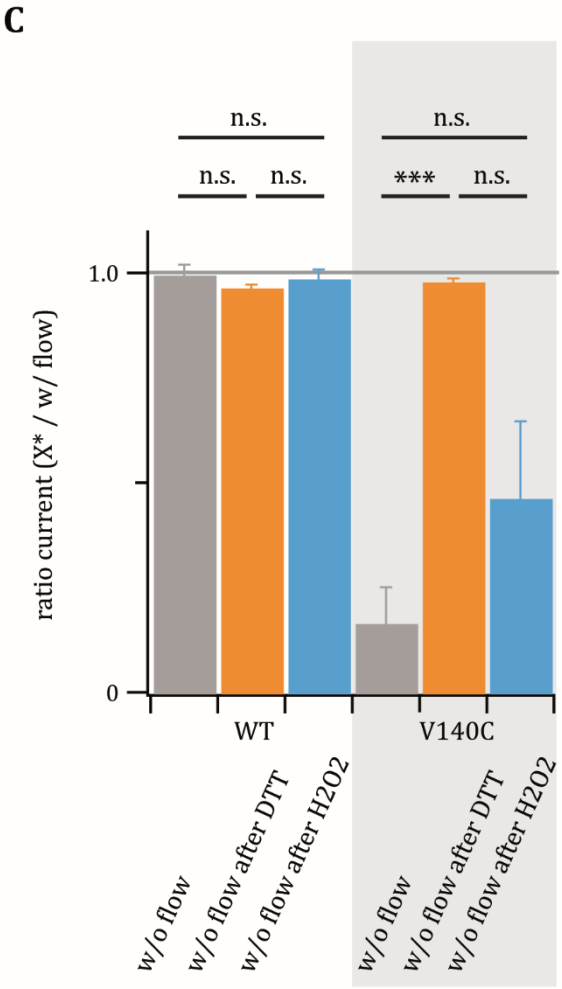

Figure 3.54: Effect of the application of DTT and H_2O_2 on the flow-dependency of activity of zebrafish prestin V140C. Left graphs show the normalised change in the transport currents. The measurements were normalised to a representative trace with stable values under flow condition (marked by the black asterisk). Black bars and traces show a condition with fluid-flow, grey bars and traces without fluid-flow, orange bars the application of DTT (5 mM), blue bars the application of H_2O_2 (150 mM). The upper graphs show a representative measurement of wild type (WT), the lower graphs of V140C. The right graphs show corresponding representative traces. Asterisks mark the position of the corresponding traces. **A:** Effect of DTT on the flow-dependency of zebrafish prestin. **B:** Effect of H_2O_2 on the flow-dependency of zebrafish prestin. **C:** The bar diagram sums up effects of DTT and H_2O_2 on the transport currents. The denoted ratios are for a mean of five representative traces without fluid-flow when the effect was fully distinct compared with a mean of five representative traces with fluid-flow directly before the effect was initiated by turning off the fluid-flow. $n \geq 5$. Mean ± SEM.

Through these experiments it was not possible to determine whether the redox agents were interacting directly with the cysteine introduced at position 139 (or 140, respectively) or whether they were acting by changing the environment of the anion translocation pathway or the protein and thereby affected the flow-dependency of activity of rat prestin V139C and zebrafish prestin V140C, respectively. To address this question, a combined experiment was performed. After application of the redox reagents (DTT or H_2O_2) the MTS compound MTSET was applied, which was previously shown to interact with rat prestin V139C (cf. Figure 3.12).

Figure 3.55 shows the results of this combined experiment. Although slightly different degrees of NLC reduction upon MTSET application were observed, dependent on redox pretreatment, these differences were not statistically significant.

Thus, most likely, MTS-reactivity of cysteine 139 was not altered by the redox manipulations, argueing against a direct effect of the redox state on this cysteine.

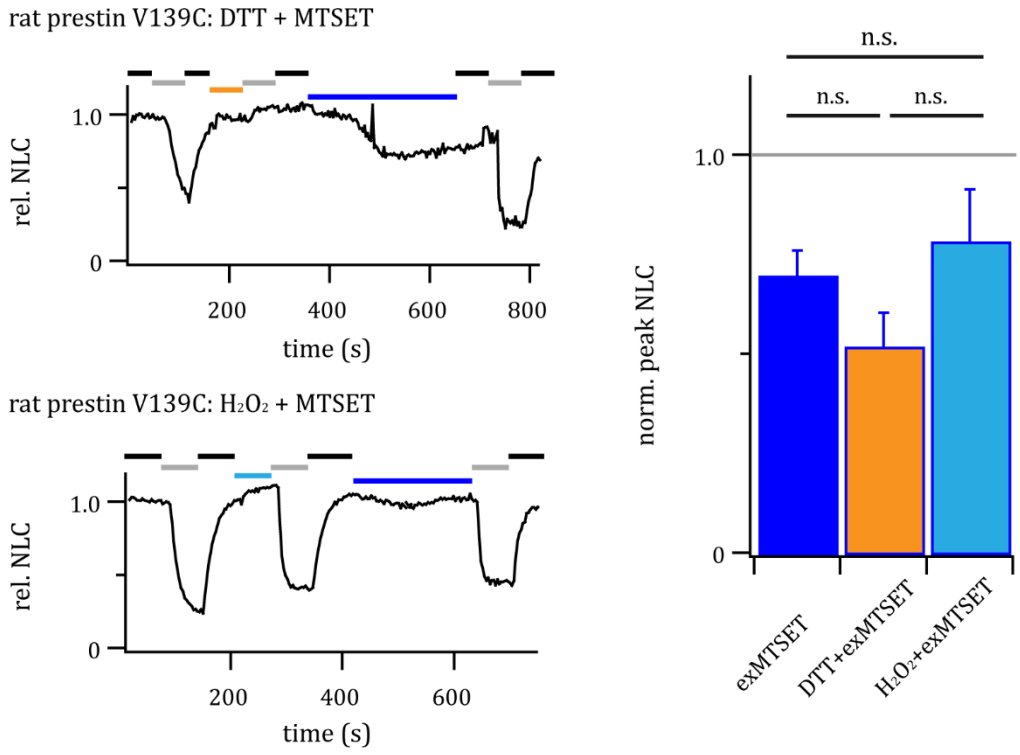

Figure 3.55: Combination of DTT or H_2O_2 and extracellularly applied MTSET in rat prestin V139C. Black bars: with fluid-flow; grey bars: without fluid-flow; orange bars: application of DTT (5 mM); light blue bars: application of H_2O_2 (150 mM); dark blue bars: application of MTSET (1 mM). The left graphs were normalised peak NLC traces. The bar diagram shows the effects of extracellularly applied MTSET (exMTSET) with and without preapplication of DTT or H_2O_2, respectively, on the NLC peak amplitude. n≥3. Mean ± SEM.

3.4.5 Probing the orientation of prestin's anion-binding site with competitive inhibitors

The results of the cysteine modification strategy described above provided the first experimental evidence for an elevator-like conformational behaviour of a transport-active prestin ortholog, and, moreover, suggested that mammalian prestin undergoes a similar, although incomplete molecular reorientation.

Nevertheless, the interpretation of the data was somewhat complicated by the complex behaviour of the important mutant V139C (V140C in zebrafish prestin). Moreover, the cysteine modifications might have altered the behaviour relative to the wild type prestin. Therefore, an alternative approach for probing transport- and electromotility-related reorientations was carried out.

In this respect, it is noteworthy that competitive inhibitors of anion-binding to prestin have been identified. Such inhibitors should act from either side of the membrane, if the anion-binding site is fully translocated through the membrane, as a consequence of an elevator movement, but its action should be restricted to one side, if the protein is only capable of partial reorientation.

The best-characterised blocker of mammalian prestin is salicylate, which competes with chloride for the anion-binding site (Oliver et al., 2001; Santos-Sacchi et al., 2006). However, because of its reversible deprotonation under physiological conditions, salicylate is membrane-permeable and when applied extracellularly passes through the cell membrane. There is strong evidence indicating that salicylate blocks mammalian prestin from the cytosolic side (Kakehata & Santos-Sacchi, 1996; Oliver et al., 2001) – however, given its presence at both sides of the membrane, it is not well suited to probe accessibility of the substrate-binding site to specifically one face of the membrane. Therefore, the use of membrane-impermeable salicylate analogues was considered. Phenolsulphonic acid (PSA) appeared as an ideal compound, as it is structurally highly similar to salicylate but membrane-impermeable. Preliminary experiments performed by Florian Nies in the Oliver lab confirmed this hypothesis. He compared the effects of extracellularly applied salicylate and PSA on the wild type constructs of chicken and rat prestin. Supplemental figure 7.4 shows the results. In summary, transport currents of the transport-capable chicken prestin were blocked by salicylate as well as PSA with a non-significant difference. By contrast, NLC amplitudes of rat prestin wild type were only blocked by extracellularly applied salicylate but not PSA. The $V_{1/2}$ was not affected.

Figure 3.56 shows the results of the experiments with these two blockers in rat prestin wild type and V139C performed by the author. The NLC of rat prestin wild type was blocked by extracellularly applied 10 mM salicylate (37.0 ± 0.7 %), but not by 10 mM PSA (97.5 ± 3.3 %) and the difference between the effects of the two blockers was highly significant. These results were consistent with the preliminary results of Florian Nies. In contrast, the NLC of the mutant V139C was blocked by both reagents (salicylate (10 mM): 52.0 ± 2.0 %; PSA (10 mM): 69.3 ± 9.4 %) with a non-significant difference.

These results suggest that the mutation V139C renders the mutant sensitive to an extracellular blocker, presumably acting by competitively binding to the substrate-binding site. Therefore, this mutant probably alters the conformational landscape of prestin towards an extracellularly accessible conformation.

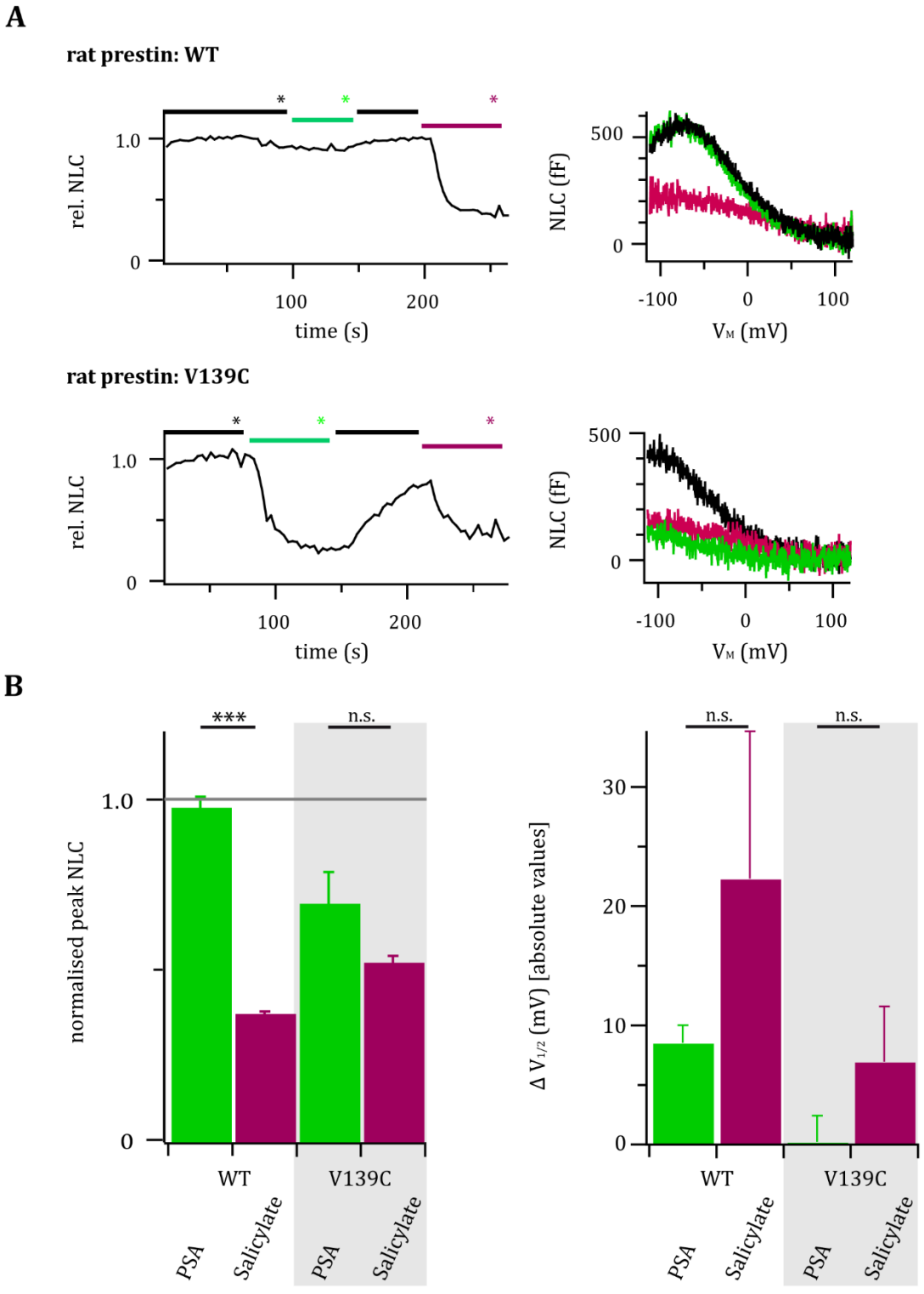

Figure 3.56: Comparison of the two NLC blockers phenolsulphonic acid (PSA) and salicylate. Black bars and traces: with fluid-flow; green bars and traces: extracellularly applied PSA (10mM); purple bars and traces: extracellularly applied salicylate (10 mM). **A:** The upper graph shows a representative measurement of rat prestin wild type (WT), the lower graph of rat prestin V139C. The left graphs were normalised NLC peak traces. The right graphs show corresponding representative traces. Asterisks mark the position of the corresponding traces. **B:** The bar diagrams show the average effects on the NLC amplitude and the $V_{1/2}$ upon PSA or salicylate application. n≥3. Mean ± SEM.

4 Discussion

Two transmembrane domains that are predicted parts of the central cavity of prestin were investigated with an accessibility study (SCAM) with the aim to obtain experimental insights into the structural dynamics in this region which could then be interpreted with respect to the working hypothesis of an elevator transport mechanism. Transmembrane domain 10 was studied because it includes the putative anion-binding site. S399 in zebrafish prestin is part of the putative anion-binding site, which is structurally homologous to position S396 in rat prestin. Transmembrane domain 3 is the 'counterpart' of transmembrane domain 10 with similar structure/motifs but an antiparallel orientation. Furthermore, these two domains were analysed in a comparative manner in both rat and zebrafish prestin as representatives of mammalian and non-mammalian prestin, which differ in their transport-related function. While the mammalian prestin has electromotile properties, the non-mammalian prestin functions as an anion exchanger. Experimental structures of other SLC26 members and structurally related transporters suggest an alternating-access mechanism for the anion exchange (Reithmeier et al., 2016; Thurtle-Schmidt & Stroud, 2016; Walter et al., 2019). In this scenario, the complete core domain moves along the gate domain allowing for alternate access of the anion-binding site in a molecular reorientation also termed 'elevator transport movement'. Such conformational dynamics predict that parts of the core domain should change their exposure to extracellular and intracellular sides, depending on the conformation of the protein during the transport cycle. Our working hypothesis is that mammalian prestin also performs an elevator movement, however an incomplete one, which has evolved from the anion exchange mechanism used by other SLC26 isoforms, including non-mammalian prestin orthologues. A comparison of the accessibilities of both prestin orthologues was expected to provide conclusions regarding the molecular dynamics underlying anion transport and electromotility.

Although the accessibilities of positions in rat and zebrafish prestin are not identical, they are similar. The data suggest that the function of SLC26 transporters follows general principles. The generation of NLC and in consequence the electromotile changes in cell length are realised by conformational changes, which are also underlying anion transport.

Accessibility of positions within transmembrane domain 10 from the intracellular side and of positions within transmembrane domain 3 from the extracellular side are consistent with the structural models derived from experimental structures

Positions within the transmembrane domains 3 and 10 of rat and zebrafish prestin mostly show accessibilities as expected from the structural models. This means that positions within transmembrane domain 3 are accessible from the extracellular side, positions within transmembrane domain 10 are accessible from the intracellular side.

The accessibilities of positions within transmembrane domain 3 and 10 of both rat and zebrafish prestin are shown in Figure 4.1. Note that position numbering is shifted by one (three) amino acid in transmembrane domain 3 (in transmembrane domain 10), e.g. I134 in rat prestin is structurally homologous to position I135 in zebrafish prestin. Within transmembrane domain 3, the extracellularly accessible positions located most towards the extracellular end of transmembrane domain 3 were G145 in rat prestin and G147 in zebrafish prestin. The respective structurally homologous positions were dysfunctional and could therefore not be tested for accessibility. The next positions with accessibility to the extracellular side were L142 in rat and L143 in zebrafish prestin. Furthermore, position S142 in zebrafish prestin was accessible to extracellular solutes, whereas the structurally homologous position in rat prestin (S141) was insensitive to MTS application. Also the position V139 in rat and the corresponding position V140 in zebrafish prestin were extracellularly accessible. Together these extracellularly accessible positions occur every third amino acid position along the primary sequence, which fits the predicted position of these amino acids in an alpha helix because one helix turn is 3.6 amino acids. Consequently, these positions fall directly above each other and are facing the predicted substrate access pathway. Moreover, it has to be noted that the structurally homologous positions in rat and zebrafish prestin were modified by the extracellular application of the same MTS reagent, e.g. rat prestin L142 was accessible to extracellularly applied MTSES and MTSET and this was also correct for zebrafish prestin L143.

Transmembrane domain 10 of rat prestin was already investigated previously (Gorbunov et al., 2014) and those results are also listed in Figure 4.1 B. The putative anion-binding site S396 was only intracellularly accessible. This again suggests an incomplete transport cycle, in which this position is never faced towards the extracellular side. Another four positions within transmembrane domain 10 were affected by intracellular application of MTS compounds via the patch pipette. These positions are all oriented closer to the cytoplasm than S396. The first position within transmembrane domain 10 of rat prestin, which showed extracellular accessibility, was Q389. The structurally homologous position in zebrafish

prestin, H392, was insensitive to applied MTS. Again, this is a non-conserved position. The basic histidine is substituted for a neutral but polar glutamine. The reason for different behaviour can be the different amino acids or a different relocation of the positions during the conformational transition.

The comparison between accessibilities within transmembrane domain 10 of rat and zebrafish prestin show that most of the accessibilities are the same and correspond to structurally homologous positions but there are also differences: S403 was intracellulary accessible in zebrafish prestin but the structurally homologous position S400 in rat prestin was dysfunctional and therefore was not tested for its accessibility.

Interestingly, two positions within transmembrane domain 3 of rat prestin were accessible from the intracellular side. The first position was P136. Accessibility of P136C from the intracellular side is consistent with lining the anion-binding site ('central cavity') as suggested by the inside-open homology model of prestin. This is one of the few amino acids in transmembrane domain 3 that is not conserved between zebrafish and rat prestin. The rat prestin residue proline substitutes for a threonine in zebrafish prestin at the structurally homologous position. These two amino acids are both neutral, but threonine is a polar amino acid and proline is a nonpolar which is known to often introduce a kink into the protein structure. T137 in zebrafish prestin was insensitive to MTS application. The second position was V139 of rat prestin that was even accessible from both sides. The crystal structure of SLC26Dg, a bacterial homolog of prestin, predicts inaccessibility of the positions near the anion-binding site to the extracellular side in the inward-open conformation of the protein (Geertsma et al., 2015). This two-sided accessibility was not expected for a position in rat prestin as it does not function as transporter. But this finding helps to understand the molecular dynamics of prestin. It suggests for a rigid transmembrane movement of the core domain against the gate domain where position V139 does not undergo a rearrangement. This finding supports the idea of an alternating-access mechanism with an elevator-like movement. According to the model of prestin, the position V139 is located within the anion permeation pathway near the putative anion-binding site S396. Depending on the residue on position 139, valine or cysteine, the distance between it and S396 is 6.73 Å to 8.44 Å (in the inward-open conformation) based on the structural homology model (Gorbunov et al., 2014). Position V139 in rat prestin faces to different sides of the cell membrane during the transport cycle depending on the conformational state of the protein, whereas according to the theory of an incomplete transport cycle performed by mammalian prestin the outward-open conformation will probably never be reached, which was supported by the single-sided accessibility of S396C (Gorbunov et al., 2014). The two-sided accessibility of V139C

could most likely be in an elevator-like manner as it has been suggested for the prokaryotic SLC26 member (Geertsma et al., 2015). Furthermore, crystal structures of the related transporter families SLC23 and SLC4 suggest an alternating-access transport via an elevator mechanism (Arakawa et al., 2015; Alguel et al., 2016; Thurtle-Schmidt & Stroud, 2016). A recently published crystal structure of the uracil transporter UraA is in the occluded state (Yu et al., 2017) and thereby allows for comparison of two different conformational states of the same protein. Yu and colleagues observed a downward and leftward sliding of the core domain against the gate domain while changing from the occluded state into the inward-open conformation. Superposition of both states let them conclude that anion transport is realised by a combination of an elevator and rocking bundle mechanism. The elevator transport mechanism is further supported by recently published structures of a eukaryotic SLC26A9 (cryo-EM), which directly compare the protein in the inward-facing and intermediate state (Walter et al., 2019). Although experimental structures are not yet available, the presented accessibility results, in particular the extracellular accessibility of V139, strongly suggests the outward movement of the core domain consistent with an elevator movement in electromotile mammalian prestin.

Additionally, V139C in rat prestin was extracellularly accessible to both MTS compounds, whereas it was only modified by the negatively charged MTSES from inside. It seems that the way to the central cavity and to this position is more selective from the cytoplasmic side.

The accessibility scanning of transmembrane 3 in zebrafish prestin corresponds in many points with the results of transmembrane 3 in rat prestin. These findings indicate that there is a common mechanism used by both prestin variants. This hypothesis could be perfectly underpinned by the two-sided accessibility of the mutant V140C of zebrafish prestin. The cysteine modifications of this mutant leave no doubt about its extracellular accessibility.

However, it was not possible to obtain reliable results regarding the application of MTSES from the cytoplasmic side within this study. The results of intracellularly applied MTSET are in line with the results of the structurally homologous position V139C in rat prestin. Both positions are insensitive to MTSET applied from the inside. Several attempts have been made to measure V140C with intracellular application of MTSES. The transport currents of the mutant V140C (-52.4 ± 8.8 pA at 0 mV, n=5) were smaller than of the control (-67.2 ± 29.3 pA at 0 mV, n=5) under standard conditions without MTS application but good enough to read out. However, the measurements with application of intracellular MTSES showed small or even no signals (-7.18 ± 4.87 pA at 0 mV, n=11). One consideration was that the diffusion of the MTSES reagent was faster than of the oxalate from the patch pipette into the

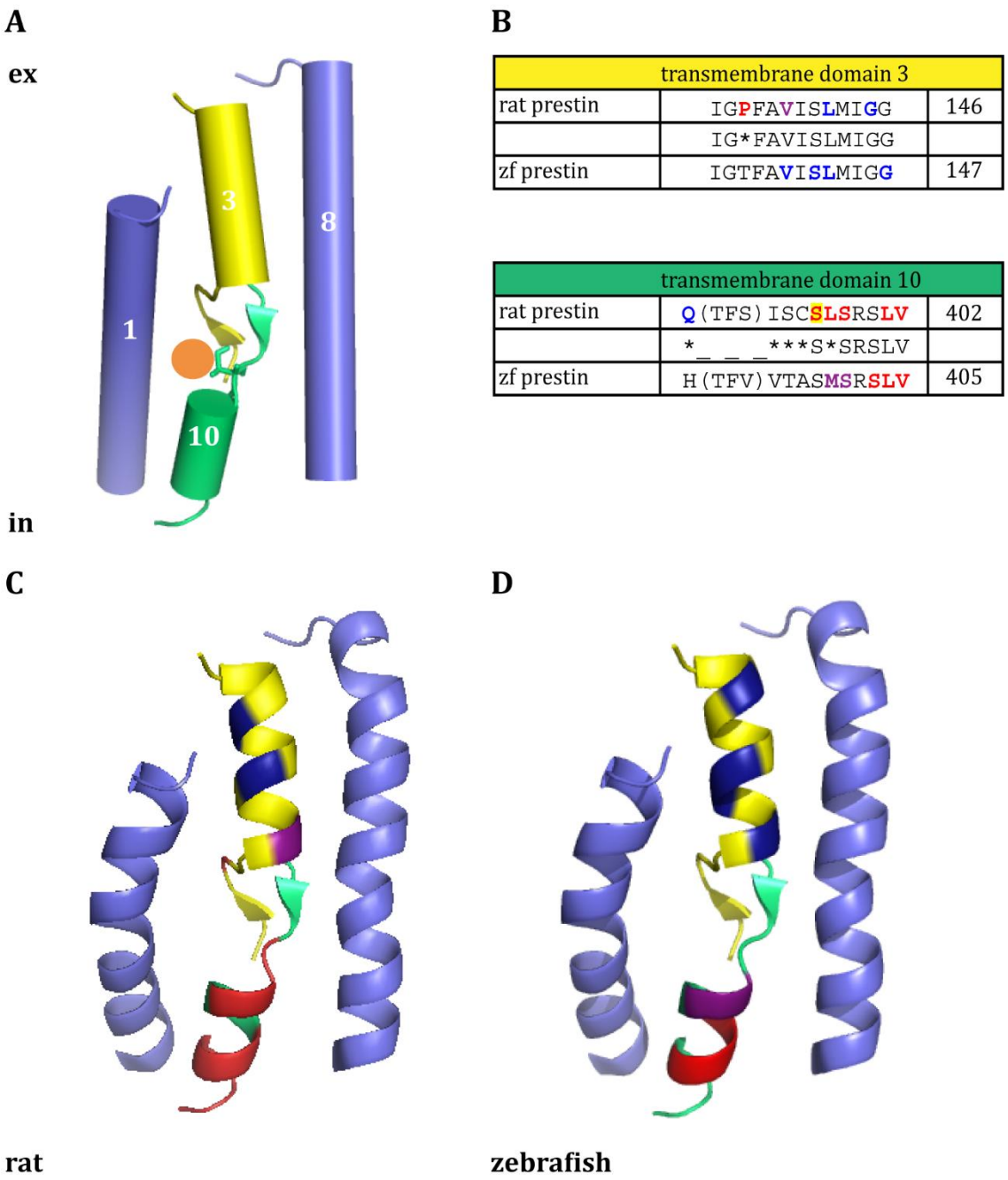

Figure 4.1: Comparison of the SCAM results in rat and zebrafish prestin. A, C and D: The homology model of prestin (Gorbunov et al., 2014) shows the transmembrane domains 1, 3, 8 and 10. **A:** The orange circle symbolises a bound anion. The position S396 is shown as sticks. **B**: Sequence alignment of rat and zebrafish (zf) prestin. Positions with proven accessibilities are highlighted in blue (extracellularly accessible), in red (intracellularly accessible) and purple (from both sides). The presumptive anion-binding site in rat prestin S396 has a yellow background. **C+D**: Model of rat (**C**) and zebrafish (**D**) prestin with focus of the central cavity and accessible positions which are highlighted in the mentioned colours.

patched cell. If the intracellular application of MTSES causes a cysteine modification resulting in the block of transport currents it can be possible that no transport currents will be detectable. The extracellular application of oxalate via the application system accelerates the onset of measurable transport currents. Therefore, experiments were performed with separated reagents, oxalate (10 mM) extracellularly applied via an application capillary and

MTSES intracellularly applied via the patch pipette. The application of the oxalate was started in the cell-attached mode before the membrane was ruptured and the measurement started. This approach was also not successful in generating appropriate good signals. The increase of the oxalate concentration (100 mM) led to larger transport currents, but the measurements were unstable and cells get too leaky very rapidly (21.8 ± 0.9 pA at 0 mV, n=2). Both MTS reagents often delivered small or even no signals when applied via the patch pipette. This observation suggests that a small amount of the MTS reagent could be attached to the outside of the patch pipette, which suppressed the currents. This idea is supported by the extracellular cysteine modifications of the mutant V140C that influenced the signal within a few seconds (Figure 3.25). Therefore, one could consider that the MTS compounds had an effect before the measurement with intracellularly applied MTS was started. DTT is a chemical compound that is used as reducing agent. It can dissolute the bond formed between a cysteine and the sulfhydryl group of the MTS reagents. Furthermore, it increases the transport current of this mutant per se (Figure 3.54). The extracellular application of DTT should increase the signal and suppress any extracellular effect of MTS attached to the patch pipette. The application of DTT delivered better signals and no effect of the intracellularly applied MTSES was observed. But the cells were not of the best quality at that moment and did not survive for an adequate time. The question remains whether there is no intracellular effect of MTSES or whether the cysteine modification takes longer after the previous DTT application. Although it is very attractive to speculate that structurally homologous positions in rat and zebrafish exhibit the same accessibilities, it is not possible to make a certain statement of the intracellular accessibility of the position V140 in zebrafish prestin by the MTSES compound at this time.

The two-sided accessibility of central positions in zebrafish prestin indicate alternating-access transport - consistent with elevator movement of the core domain – and furthermore, the lack of extracellular access of the homologous positions in rat prestin shows that the extracellular-exposed conformation is not obtained in mammalian prestin (previous results)

The two-sided accessibilities of zebrafish prestin M400 and S401 and the single-sided accessibilities of their corresponding positions in rat prestin (L397 and S398) are again in line with expectations. The transporter function of zebrafish prestin requires the facing of the central cavity towards both sides of the cell membrane for the anion exchange. Furthermore, both prestin orthologues show positions in close proximity that are only intracellularly accessible, thus these parts of the anion translocation pathway are never faced towards the outside. These observations further support the theory of the incomplete

transport cycle performed by mammalian prestin (Schaechinger et al., 2011). Of particular interest was the accessibility of position S399 in zebrafish prestin. S399 is structurally homologous to S396 in rat prestin, which is part of the presumptive anion-binding site (Gorbunov et al., 2014). Rat prestin S396 is intracellularly accessible and zebrafish prestin S399 was expected to be accessible from both sides. The mutant S399C in zebrafish prestin is dysfunctional and a potential cysteine modification could therefore not be tested. Another transport-capable orthologue is chicken prestin but the mutation of the corresponding position in chicken prestin (S402C) also resulted in a dysfunctional mutant. But the two-sided accessibilities of M400 and S401 (zebrafish prestin) are sufficient to provide adequate information about the organisation of the anion pathway and the molecular dynamics during anion translocation. The loss of transporter function goes along with the electromechanical activity of mammalian prestin. Thus, it coincides with our expectations to find positions near the anion-binding site with double-sided accessibility in zebrafish prestin but not in rat prestin. This constitutes further evidence that the electromotile transition and the conformational states are connected.

The two-sided accessibility of rat prestin V139C points towards an outward movement of the core domain within an incomplete transport transition

The rigid movement of the core domain against the gate domain indicates an alternating-access in an elevator-like transport. Especially, the rat prestin mutant V139C gives a strong hint for this transport mode. The two-sided accessibility of this mutant shows that V139 faces the translocation pathway in the inward-open as well as in the occluded conformation and thus stays rigid and does not undergo a conformational rearrangement. An alternating-access transport in elevator mode is characterised by a relatively rigid immobile gate domain, a mobile core domain, which contains the anion-binding site, and a vertical displacement of the bound substrate. The results of the scanning support this mode of transport that was also proposed for a prokaryotic SLC26 family member (Geertsma et al., 2015). While crystal structures record a protein in a certain conformation, cysteine labelling provides the opportunity to study the full conformational changes. Figure 4.2 illustrates the model derived from the results of the scanning.

The model shows the movement of the core against the gating domain in rat (upper row) and zebrafish prestin (lower row). There is a schematic model in the inward-open conformation according to the structural homology model (Gorbunov et al., 2014) on the left side. Alternate conformations are shown on the right side which are determined by the extracellular accessibilities of positions of the respective prestin orthologue. To what extent the core domain opens to the extracellular side can be deduced from the accessibilities of

the positions V139 within transmembrane domain 3 in rat prestin and M400 and S400 within transmembrane domain 10 in zebrafish prestin (Figure 4.2: shown in purple). There is an obvious difference between the alternate conformation of rat and zebrafish prestin. The core domain of zebrafish prestin moves along the gate domain as far as positions within transmembrane domain 10 also faces the extracellular side. This demonstrates the different conformational states of rat and zebrafish prestin. Zebrafish prestin undergoes a full transport cycle from an inward-open to an outward-open conformation, whereas rat prestin alternates between the inward-open and the intermediate (occluded) conformation. The results of the scanning show that the elevator mode of transport is mainly realised by zebrafish prestin. Rat prestin fails to reach the outward-open conformation, thus it performs an incomplete transport mechanism in an elevator-like manner.

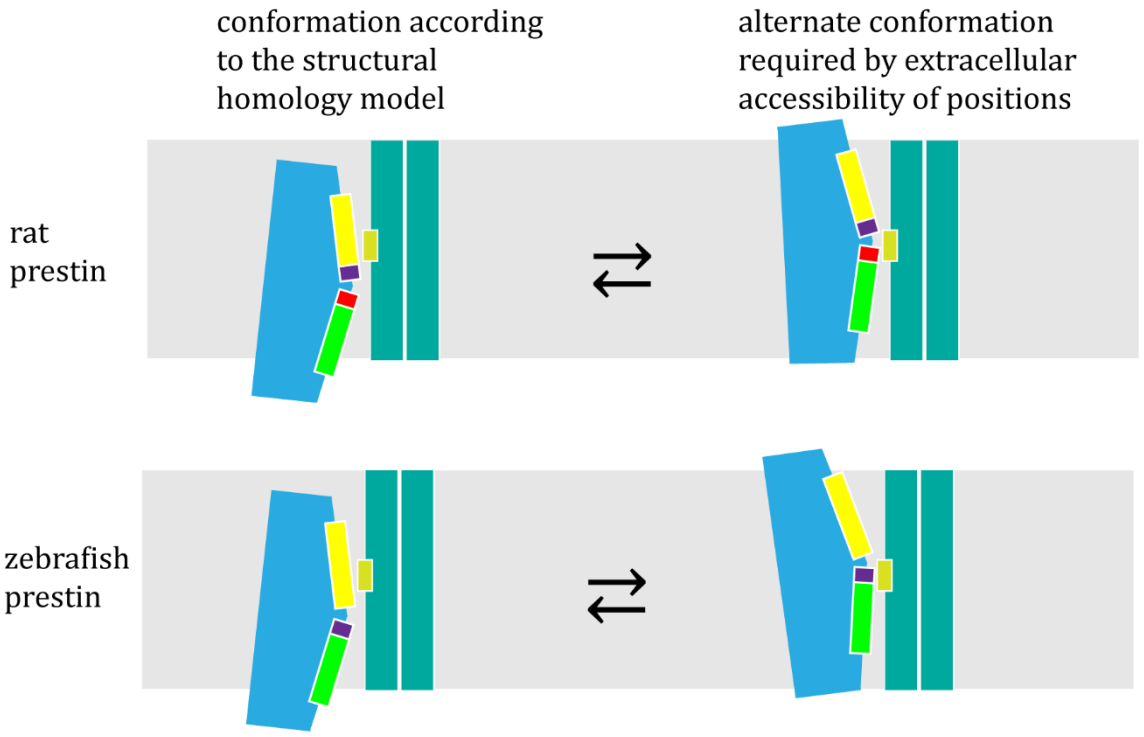

Figure 4.2: Comparison of the conformational states realised in rat and zebrafish prestin. Schematic overview of the conformational states of rat (upper row) and zebrafish prestin (lower row). The figure shows a full monomer of prestin that is connected to a second monomer of which only the gate domain is outlined. On the left: the inward-open conformation. On the right: the occluded state (rat prestin) and the outward-open conformation (zebrafish prestin). Core domains in blue, gating domains in teal, transmembrane domain 3 in yellow and transmembrane domain 10 in green. Accessibilities are highlighted in red (intracellularly accessible) and purple (from both sides). The small olive-green square within the gating domain symbolises the electrostatic barrier, which has to be overcome for conformational changes.

Although the mutant V139C shows some alteration of behaviour (mechanosensitivity) it supports the elevator model

In addition to the two-sided accessibility of rat prestin V139C, the mutation of valine to cysteine induced a special flow-sensitivity (Figure 3.45). In the absence of fluid-flow, the NLC of the mutant rat prestin V139C significantly decreased. This flow-dependency of activity was reversible. A similar behaviour was found in the structurally homologous mutant V140C in zebrafish prestin (Figure 3.48). Without applied flow the transport current decreased significantly and reversibly. Zebrafish prestin wild type showed no flow-sensitivity.

The related behaviour of rat prestin V139C and zebrafish prestin V140C upon flow application indicates common conformational dynamics in SLC26 transporters. It is presumed that core and gating domain tilt against each other to move anions through the protein to produce electromotility or transport currents, respectively. Predicted by the structural model of mammalian prestin (Gorbunov et al., 2014) V139 is located within a region that serves as a pivot point for the tilting process, which is necessary for the conformational changes underlying anion translocation and in consequence NLC generation/electromotility. The results obtained by SCAM demonstrated the accessibility of rat prestin V139C from both sides, intra- and extracellular (Figure 3.11 and Figure 3.18). The data here presented further suggest that this position – if mutated to cysteine – might react to mechanical stress from the extracellular side due to its flow-dependency of activity.

Also, the rat prestin wild type was affected by applied fluid-flow (Figure 3.45). With applied fluid-flow the $V_{1/2}$ shifted in the depolarising direction. In CHO cells transiently transfected with rat prestin the $V_{1/2}$ is around -70mV (Ludwig et al., 2002; Schaechinger et al., 2011), which is comparable with values in mammalian outer hair cells, e.g. from rat and mouse (Ludwig et al., 2002; Zhu et al., 2013), although this hallmark varies in outer hair cells according to conditions like postnatal stage (Oliver & Fakler, 1999). Without fluid-flow the $V_{1/2}$ of wild type rat prestin shifted from -78.33 ± 3.27 mV to more hyperpolarised potentials of -110.66 ± 5.09 mV (n=11). This is a shift of around 32.33 mV, which is a considerable shift compared to other experiments, e.g. Santos-Sacchi and colleagues (Santos-Sacchi et al., 2001) observed a maximum $V_{1/2}$-shift of 7.5 mV in TSA 201 cells transiently transfected with gerbil prestin upon a pipette pressure of 2 kPa. This effect was reversible and they claimed that those transfected cells are sensitive to membrane tension. The shift of the $V_{1/2}$ is small compared to the shift in outer hair cells, where it is about 50 mV upon applied pressure (Kakehata & Santos-Sacchi, 1995), which the authors explain by additional components in outer hair cells interacting with prestin, which are absent in transfected

cells. There are two main physiological mechanisms, which could cause a shift of the $V_{1/2}$: membrane tension and phosphorylation (Frolenkov et al., 2000). In the data here presented, the response of CHO cells transiently transfected with the wild type of rat prestin to applied fluid-flow was similar to that of TSA 201 cells transiently transfected with gerbil prestin and outer hair cells to applied pipette pressure (Kakehata & Santos-Sacchi, 1995; Santos-Sacchi et al., 2001).

Regarding the $V_{1/2}$-values of V139C there was also a shift to hyperpolarised potentials in the absence of fluid-flow beside the decreased NLC (from -105.92 ± 2.08 mV to -118.36 ± 2.99 mV; n=19). The voltage range of the measurements was ± 120 mV. Some of the values of V139C are out of range and furthermore a reliable analysis of the $V_{1/2}$ was limited by drastically decreased NLCs (partially around 100 fF). The more reliable and evident effect of the fluid-flow on V139C is the change in NLC peak amplitude.

Because of the $V_{1/2}$ -shifts of rat prestin wild type upon applied fluid-flow and its similarity with the reported shifts upon applied membrane tension it was the next step to find out if the flow-dependency of activity of the mutant rat prestin V139C was also caused by membrane tension. To answer this question, it was necessary to analyse whether the application of fluid-flow really induces changes in membrane tension, which in turn affects the NLC. Measurements with extracellular solutions of different osmolarities caused a swelling or shrinkage, respectively, of the affected cells, as it was expected. However, it had no influence on the NLC. Furthermore, the role of membrane fluidity was tested for consequences on the flow-dependency of activity of V139C. Cholesterol depletion by MßCD, which decreased membrane stiffness and destroyed cholesterol-rich microdomains, only shifted the $V_{1/2}$ but it did not affect the flow-dependency of activity of V139C (Figure 3.50). After pretreatment with MßCD the influence of solutions with different osmolarities was tested again but still had no effect on the flow-dependency of activity of V139C. But after the pretreatment with MßCD the $V_{1/2}$ shifted upon application of hyper- and hypotonic solutions as expected. Application of hypertonic solution caused $V_{1/2}$-shifts in the hyperpolarised direction in wild type prestin as well as in the mutant V139C and in the depolarised direction upon application of hypotonic solution. Thus, the flow-dependency of activity of V139C cannot be explained by changes in membrane tension.

Furthermore, the role of intracellular signalling cascades can be excluded by the measurement of outside-out patches, which reproduced the flow-dependency of activity of V139C as it was observed in whole cell recordings (Figure 3.52). Additionally, the role of the actin cytoskeleton on protein stability does not seem to be important as after preincubation

with Latrunculin A (an inhibitor of actin polymerisation) the flow-dependency of activity of V139C was still preserved (Figure 3.51).

Mutations to other amino acids than cysteine at position V139 in rat prestin did not introduce a flow-sensitivity of activity. Cysteines are known to form covalent bonds with other cysteines. These disulphide bonds play an important role in forming the tertiary structure of a protein. However, this cannot be the case here because the basic construct of V139C was a cysteine-free variant of rat prestin (WT_△Cys). Furthermore, V139 is positioned deep in the central cavity of prestin. Thus, interactions with other cysteine-containing proteins are unlikely. Cysteines can also react with the protein backbone itself as it was described for the phosphatase PTP1B (van Montfort et al., 2003). PTP1B is a protein tyrosine phosphatase with a catalytic cysteine (C215) within the characteristic signature sequence of PTP1B. The negatively charged side chain of C215 is stabilised by amino acids of the protein backbone to facilitate the binding of the phosphate moiety of the substrate phosphotyrosine. With further oxidation of the cysteine from sulphenic acid to sulphinic and sulphonic acid it loses the stabilising bonds resulting in an inactivate enzyme.

Although the cysteine in rat and zebrafish prestin is not native, it was a further approach to test if the redox state of this cysteine influences the flow-dependency of activity. Redox agents were used here to change the redox state of the cysteine at position V139. After application of H_2O_2, cysteines are suspected to be oxidised. Under this condition the flow-dependency of activity of V139C was preserved. After application of DTT, cysteines are reduced. In this case the flow-dependency of activity was abolished (Figure 3.53). Similar results were obtained for the transport-capable zebrafish prestin carrying the V139C-homologous mutation V140C (Figure 3.54). The effects of the redox agents (DTT and H_2O_2) on the flow-dependency of activity are similar to those observed in rat prestin V139C. In wild type zebrafish prestin neither DTT nor H_2O_2 affected the transport currents. In contrast to the wild type, DTT and H_2O_2 already affected the size of the transport currents of the V140C mutant in zebrafish prestin. The currents strongly increased upon DTT application, whereas application of H_2O_2 nearly blocked the transport currents of the mutant. The response of V140C on flow changes abolished after DTT application, while there still was the flow-sensitivity of activity after application of H_2O_2, even if it was reduced. Though the effect on the flow-dependency of activity was similar to that in rat prestin V139C, it has to be mentioned that the transport current of zebrafish prestin V140C, but not the NLC peak amplitude of rat prestin V139C, was affected by application of redox agents. The reason for this is elusive. By these experiments it was not possible to differentiate whether the redox agents are interacting directly with the cysteine or are acting through changing the

environment of the translocation pathway or the protein and thereby affecting the flow-dependency of activity. A possible explanation is that the cysteine of rat prestin V139C and zebrafish prestin V140C, respectively, was reduced by DTT and therefore the protein became more flexible, which facilitated conformational changes and abrogated the flow-dependency of activity. In contrast, the application of H_2O_2 did not change the mechanosensitive properties of these mutants. Even without an *in vivo* function of the cysteine in rat (V139C) and zebrafish prestin (V140C), respectively, the change of the mechanosensitive properties upon DTT application could be due to the formation of bonds with the protein backbone and thus the stabilisation of the cysteine.

Interestingly, the same reagents influenced the flow-dependent shift of the $V_{1/2}$ in wild type rat prestin as the flow-dependency of activity of V139C (Figure 3.53). The effect was abolished after DTT application, whereas H_2O_2 had no influence on the flow-dependent shift.

In summary, V139C showed a combination of mechano- and redox-sensitivity. As mentioned above, the flow-dependency of activity of rat prestin V139C seems to be correlated with the microenvironment of the mutant - the more inflexible the side chain the more distinct the flow-dependency of activity. On the basis of the presented data the applied fluid-flow does not cause membrane tension in V139C. The flow-dependency of activity of V139C seems to be provoked by pure shear stress. The tension-sensitivity of prestin wild type is an intrinsic property where tension leads to a shift of the voltage-dependent $V_{1/2}$ and thereby reduces the necessary energy to produce NLC and in consequence electromotile changes in outer hair cells. In contrast, applied fluid-flow changes the ability or the number of proteins to be activatable in the mutant V139C. Finally, the phenomenon of the mechano- and redoxsensitivity could not yet be clarified.

In fact, the mutant V139C shows some alteration of behaviour regarding its flow-sensitivity of activity, but given its position at a pivot point it supports the elevator model. Fundamentally, the function of rat prestin V139C and zebrafish prestin V140C, respectively, is preserved. Thus, the conformational landscape cannot be totally different between the mutant and the wild type.

Altered extracellular efficacy of blocker in fact suggests a wider opening to the extracellular face of V139C compared to wild type

Furthermore, rat prestin V139C was tested for its accessibility for the membrane-impermeable phenolsulphonic acid (PSA) which is thought to block prestin's NLC. In contrast to salicylate, PSA did not block the NLC of rat prestin wild type when extracellularly applied (Figure 3.56 and Supplemental figure 7.4). Former work from Florian Nies also

proved the ability of PSA to block transport currents of chicken prestin (Supplemental figure 7.4). But the extracellular application of PSA reduced the NLC of rat prestin V139C similar to salicylate (Figure 3.56). This was unexpected and indicates a different organisation of V139C compared to the wild type. Because the presumptive anion-binding site of rat prestin is never faced towards the extracellular side, it is conceivable that PSA does not bind to the binding site directly but to a position where it hinders the conformational change and thereby blocks the NLC of V139C and transport currents in chicken prestin. Most likely, the mutant is wider open to the extracellular side in the occluded conformation compared to the wild type. That could also be the reason for its mechanosensitivity. Measurements with intracellularly applied PSA in rat prestin have to be performed for a better understanding of these results.

Nevertheless, the unchanged lack of transport and the preserved NLC does not suggest fundamental changes of the conformational landscape of V139C.

5 Outlook

The accessibilities of the cysteine mutants provide information about the molecular dynamics of the wild types. As an initial approach, further MD simulations could be performed like already realised for rat prestin (Gorbunov et al., 2014). MD simulations mimic motions of atoms and provide an opportunity to further explore the dynamics of prestin suggested by the here presented results.

A crystal structure of rat prestin is absolutely necessary to compare with the structural homology model and the findings of this study. The current trend is towards cryo-EM (cryogenic Electron Microscopy) which enables the high-resolution structure determination of frozen ('vitrified') biomolecules in solution. A cryo-EM structure of Slc26a9 was recently published (Walter et al., 2019). In this paper Walter and colleagues used a combination of cryo-EM and patch-clamp experiments to get insights into the three-dimensional structure of SLC26A9. Finally, structures of all conformational states from an electromotile prestin as well as from a transport-capable prestin orthologue will be needed to gain detailed knowledge of the intricate conformational dynamics of electromotility as well as differences and common features with anion transport.

Another option to verify the structural homology model is to examine the interaction between the core and gating domain via a cysteine-based cross-linking study (Caseley et al., 2017; Jiang, 2013). Two positions that are predicted to be juxtaposed at the interface of prestin and in close proximity to each other will be mutated to cysteines (WT_△Cys + two cysteine substitutions). Disulphide bonds between the highly reactive thiol-groups of the cysteines will form under oxidising conditions and break under reducing conditions if the cysteines are in close vicinity. In experiments, crosslinkers are used. If the spacer arms of the crosslinker reach the two cysteines, an artificial bond can be built between the two cysteines. During patch-clamp experiments, disulphide bonds between the core and gating domain impair conformational changes, which could provide further information of prestin's molecular dynamics.

The results of the cysteine accessibility study indicate a rearrangement of core and gating domain in an elevator-like manner during anion transition. But how this is connected with prestin's function as area motor is not immediately answered by this model. Prestin acts as a voltage-dependent motor protein. Voltage-clamp fluorometry combines voltage-clamp experiments and spectroscopy of fluophores tagged to mobile regions of a protein (Horne & Fedida, 2009; Kusch & Zifarelli, 2014). This technique allows to monitor structural rearrangement after voltage stimuli and thus makes the connection between structure and

function. Addressing this and other questions will be the subject of future studies, for which this work provides a profound foundation.

Redox sensitive behaviour was observed in rat prestin wild type as well as in the V139C mutant. There are studies, which investigated the impact of the production of reactive oxygen species (ROS) after noise exposure and the resulting damages to the point of hearing loss (Lorito et al., 2006; Adelman et al., 2008; Loukzadeh et al., 2015). Particularly damaged mitochondria and in consequence oxidative stress has been considered as the major reasons for age-related hearing loss (Fujimoto & Yamasoba, 2014; Kamogashira et al., 2017; Rana et al., 2017). The underlying mechanisms and a potential role of prestin are widely unknown. But the data affirm that prestin could be also affected by oxidative stress. The rat prestin mutant V139C could also provide a model system to investigate the impact of ROS on prestin.

6 References

Adelman, C., Freeman, S., Paz, Z., Sohmer, H. (2008). Salicylic acid injection before noise exposure reduces permanent threshold shift. *Audiology and Neurotology*, *13*(4), 266–272. https://doi.org/10.1159/000115436

Albert, J. T., Winter, H., Schaechinger, T. J., Weber, T., Wang, X., He, D. Z. Z., Hendrich, O., Geisler, H., Zimmermann, U., Oelmann, K., Knipper, M., Oliver, D. (2007). Voltage-sensitive prestin orthologue expressed in zebrafish hair cells. *Journal of Physiology*, *580*(2), 451–461. https://doi.org/10.1113/jphysiol.2007.127993

Alguel, Y., Amillis, S., Leung, J., Lambrinidis, G., Capaldi, S., Scull, N. J., Craven, G., Iwata, S., Armstrong, A., Mikros, E., Diallinas, G., Cameron, A., Byrne, B. (2016). Structure of eukaryotic purine/H(+) symporter UapA suggests a role for homodimerization in transport activity. *Nature Communications*, *7*, 11336. https://doi.org/10.1038/ncomms11336

Arakawa, T., Kobayashi-Yurugi, T., Alguel, Y., Iwanari, H., Hatae, H., Iwata, M., Abe, Y., Hino, T., Ikeda-Suno, C., Kuma, H., Kang, D., Murata, T., Hamakubo, T., Cameron, A., Kobayashi, T., Hamasaki, N., Iwata, S. (2015). Crystal structure of the anion exchanger domain of human erythrocyte band 3. *Science*, *350*(6261), 680 LP – 684. https://doi.org/10.1126/science.aaa4335

Ashmore, J. (2008). Cochlear Outer Hair Cell Motility. *Physiological Reviews*, *88*(1), 173–210. https://doi.org/10.1152/physrev.00044.2006

Bai, J.-P., Surguchev, A., Montoya, S., Aronson, P. S., Santos-Sacchi, J., Navaratnam, D. (2009). Prestin's anion transport and voltage-sensing capabilities are independent. *Biophysical Journal*, *96*(8), 3179–3186. https://doi.org/10.1016/j.bpj.2008.12.3948

Bang, P. I., Sewell, W. F., Malicki, J. J. (2001). Morphology and cell type heterogeneities of the inner ear epithelia in adult and juvenile zebrafish (Danio rerio). *Journal of Comparative Neurology*, *438*(2), 173–190. https://doi.org/10.1002/cne.1308

Beurg, M. & Fettiplace, R. (2017). PIEZO2 as the anomalous mechanotransducer channel in auditory hair cells. *Journal of Physiology*, *595*(23), 7039–7048. https://doi.org/10.1113/JP274996

Beurg, M., Fettiplace, R., Nam, J.-H., Ricci, A. J. (2009). Localization of inner hair cell mechanotransducer channels using high-speed calcium imaging. *Nature Neuroscience*, *12*(5), 553–558. https://doi.org/10.1038/nn.2295

Brownell, W. E., Bader, C. R., Bertrand, D., de Ribaupierre, Y. (1985). Evoked mechanical responses of isolated cochlear outer hair cells. *Science*, *227*(4683), 194 LP – 196. https://doi.org/10.1126/science.3966153

Caseley, E. A., Muench, S. P., Jiang, L.-H. (2017). Conformational changes during human P2X7 receptor activation examined by structural modelling and cysteine-based cross-linking studies. *Purinergic Signalling*, *13*(1), 135–141. https://doi.org/10.1007/s11302-016-9553-0

Chang, Y.-N., Jaumann, E. A., Reichel, K., Hartmann, J., Oliver, D., Hummer, G., Joseph, B., Geertsma, E. (2019). Structural basis for functional interactions in dimers of SLC26 transporters. *Nat Commun* 10**,** 2032 (2019). https://doi.org/10.1038/s41467-019-10001-w

Chen, G.-D., Tanaka, C., Henderson, D. (2008). Relation between outer hair cell loss and hearing loss in rats exposed to styrene. *Hearing Research*, *243*(1–2), 28–34. https://doi.org/10.1016/j.heares.2008.05.008

Coué, M., Brenner, S. L., Spector, I., Korn, E. D. (1987). Inhibition of actin polymerization by latrunculin A. *FEBS Letters*, *213*(2), 316–318. https://doi.org/10.1016/0014-5793(87)81513-2

Dallos, P., Hallworth, R., Evans, B. N. (1993). Theory of electrically driven shape changes of cochlear outer hair cells. *Journal of Neurophysiology*, *70*(1), 299–323. https://doi.org/10.1152/jn.1993.70.1.299

Dallos, P., Evans, B. N., Hallworth, R. (1991). Nature of the motor element in electrokinetic shape changes of cochlear outer hair cells. *Nature*, *350*(6314), 155–157. https://doi.org/10.1038/350155a0

Dallos, P., Wu, X., Cheatham, M. A., Gao, J., Zheng, J., Anderson, C. T., Jia, S., Wang, X., Cheng, W., Sengupta, S., He, D., Zuo, J. (2008). Prestin-based outer hair cell motility is necessary for mammalian cochlear amplification. *Neuron*, *58*(3), 333–339. https://doi.org/10.1016/j.neuron.2008.02.028

Detro-Dassen, S., Schänzler, M., Lauks, H., Martin, I., Berstenhorst, S. M. zu, Nothmann, D., Torres-Salazar, D., Hidalgo, P., Schmalzing, G., Fahlke, C. (2008). Conserved Dimeric Subunit Stoichiometry of SLC26 Multifunctional Anion Exchangers. *Journal of Biological Chemistry*, *283*(7), 4177–4188. https://doi.org/10.1074/jbc.M704924200

Dong, W. & Olson, E. S. (2013). Detection of cochlear amplification and its activation. *Biophysical Journal*, *105*(4), 1067–1078. https://doi.org/10.1016/j.bpj.2013.06.049

Dong, X.-X. & Iwasa, K. H. (2004). Tension sensitivity of prestin: comparison with the membrane motor in outer hair cells. *Biophysical Journal*, *86*(2), 1201–1208. https://doi.org/10.1016/S0006-3495(04)74194-6

Dorwart, M. R., Shcheynikov, N., Yang, D., Muallem, S. (2008). The Solute Carrier 26 Family of Proteins in Epithelial Ion Transport. *Physiology*, *23*(2), 104–114. https://doi.org/10.1152/physiol.00037.2007

Drew, D. & Boudker, O. (2016). Shared Molecular Mechanisms of Membrane Transporters. *Annual Review of Biochemistry*, *85*(1), 543–572. https://doi.org/10.1146/annurev-biochem-060815-014520

Du, Y., Ping, J., Li, N., Wu, X., Li, L., Galbraith, G. (2007). Ultrasonic evoked responses in rat cochlear nucleus. *Brain Research*, *1172*, 40–47. https://doi.org/10.1016/j.brainres.2007.07.049

Dudel, J., Menzel, R., Schmidt, R. F. (2001). *Neurowissenschaften: Vom Molekül zur Kognition* (2. überarb). Springer.

Frank, G., Hemmert, W., Gummer, A. W. (1999). Limiting dynamics of high-frequency electromechanical transduction of outer hair cells. *Proceedings of the National Academy of Sciences*, *96*(8), 4420 LP – 4425. https://doi.org/10.1073/pnas.96.8.4420

Frolenkov, G. I., Mammano, F., Belyantseva, I. A., Coling, D., Kachar, B. (2000). Two Distinct Ca2+-Dependent Signaling Pathways Regulate the Motor Output of Cochlear Outer Hair Cells. *The Journal of Neuroscience*, *20*(16), 5940 LP – 5948. https://doi.org/10.1523/JNEUROSCI.20-16-05940.2000

Fujimoto, C. & Yamasoba, T. (2014). Oxidative stresses and mitochondrial dysfunction in age-related hearing loss. *Oxidative Medicine and Cellular Longevity*, *2014*, 582849. https://doi.org/10.1155/2014/582849

Gale, J. & Ashmore, J. (1994). Charge displacement induced by rapid stretch in the basolateral membrane of the guinea-pig outer hair cell. *Proceedings of the Royal Society of London. Series B: Biological Sciences*, *255*(1344), 243–249. https://doi.org/10.1098/rspb.1994.0035

Geertsma, E. R., Chang, Y. N., Shaik, F. R., Neldner, Y., Pardon, E., Steyaert, J., Dutzler, R. (2015). Structure of a prokaryotic fumarate transporter reveals the architecture of the SLC26 family. *Nature Structural and Molecular Biology*, *22*(10), 803–808. https://doi.org/10.1038/nsmb.3091

Gorbunov, D., Sturlese, M., Nies, F., Kluge, M., Bellanda, M., Battistutta, R., Oliver, D. (2014). Molecular architecture and the structural basis for anion interaction in prestin and SLC26 transporters. *Nature Communications*, *5*(Vimm). https://doi.org/10.1038/ncomms4622

Grande, T. & Young, B. (2004). The ontogeny and homology of the Weberian apparatus in the zebrafish Danio rerio (Ostariophysi : Cypriniformes) supraneurals claustrum scaphium intercalarium parapophysis tripus parapophysis + rib 4 neural arch 3-5 parapophysis rib 5 os suspensorium. *Zoological Journal of the Linnean Society*, *140*(August), 241–254.

Gundersen, T., Skarstein, Ø., Sikkeland, T. (1978). A Study of the Vibration of the Basilar Membrane in Human Temporal Bone Preparations by the Use of the Mossbauer Effect. *Acta Oto-Laryngologica*, *86*(1–6), 225–232. https://doi.org/10.3109/00016487809124740

Hall, J. E. (2010). *Guyton and Hall Textbook of Medical Physiology, 12th Ed* (12th ed.).

Hallworth, R. & Nichols, M. G. (2012). Prestin in HEK cells is an obligate tetramer. *Journal of Neurophysiology*, *107*(1), 5–11. https://doi.org/10.1152/jn.00728.2011

Higgs, D. M., Rollo, A. K., Souza, M. J., Popper, A. N. (2003). Development of form and function in peripheral auditory structures of the zebrafish (Danio rerio). *The Journal of the Acoustical Society of America*, *113*(2), 1145–1154. https://doi.org/10.1121/1.1536185

Hodgkin, A. L. & Huxley, A. F. (1952). Currents carried by sodium and potassium ions through the membrane of the giant axon of Loligo. The Journal of Physiology, 116(4), 449–472. https://doi.org/10.1113/jphysiol.1952.sp004717

Hodgkin, A. L. & Huxley, A. F. (1952a). A quantitative description of membrane current and its application to conduction and excitation in nerve. *The Journal of Physiology*, *117*(4), 500–544. Retrieved from https://www.ncbi.nlm.nih.gov/pubmed/12991237

Hodgkin, A. L. & Huxley, A. F. (1952b). The components of membrane conductance in the giant axon of Loligo. *The Journal of Physiology*, *116*(4), 473–496. Retrieved from http://www.ncbi.nlm.nih.gov/pubmed/14946714%0Ahttp://www.pubmedcentral.nih.gov/articlerender.fcgi?artid=PMC1392209

Hodgkin, A. L. & Huxley, A. F. (1952c). The dual effect of membrane potential on sodium conductance in the giant axon of Loligo. *The Journal of Physiology*, *116*(4), 497–506. Retrieved from https://www.ncbi.nlm.nih.gov/pubmed/14946715

Höglund, P. J., Nordström, K. J. V, Schiöth, H. B., Fredriksson, R. (2011). The solute carrier families have a remarkably long evolutionary history with the majority of the human families present before divergence of Bilaterian species. *Molecular Biology and Evolution*, *28*(4), 1531–1541. https://doi.org/10.1093/molbev/msq350

Horne, A. & Fedida, D. (2009). Use of voltage clamp fluorimetry in understanding potassium channel gating: A review of Shaker fluorescence data. *Canadian Journal of Physiology and Pharmacology*, *87*, 411–418. https://doi.org/10.1139/y09-024

Hudspeth, A. (1997). Mechanical amplification of stimuli by hair cells. *Current Opinion in Neurobiology*, *7*(4), 480–486. https://doi.org/10.1016/S0959-4388(97)80026-8

Hudspeth, A. J. (2005). How the ear's works work: mechanoelectrical transduction and amplification by hair cells. *Comptes Rendus Biologies*, *328*(2), 155–162.

Iwasa, K. H. (1994). A membrane motor model for the fast motility of the outer hair cell. *The Journal of the Acoustical Society of America*, *96*(4), 2216–2224. https://doi.org/10.1121/1.410094

Jiang, L. H. (2013). Cysteine-based cross-linking approach to study inter-domain interactions in ion channels. *Methods in Molecular Biology*. https://doi.org/10.1007/978-1-62703-351-0_21

Kakehata, S. & Santos-Sacchi, J. (1995). Membrane tension directly shifts voltage dependence of outer hair cell motility and associated gating charge. *Biophysical Journal*, *68*(5), 2190–2197. https://doi.org/10.1016/S0006-3495(95)80401-7

Kakehata, S. & Santos-Sacchi, J. (1996). Effects of Salicylate and Lanthanides on Outer Hair Cell Motility and Associated Gating Charge. *The Journal of Neuroscience*, *16*(16), 4881 LP – 4889. https://doi.org/10.1523/JNEUROSCI.16-16-04881.1996

Kalinec, F., Holley, M. C., Iwasa, K. H., Lim, D. J., Kachar, B. (1992). A membrane-based force generation mechanism in auditory sensory cells. *Proceedings of the National Academy of Sciences of the United States of America*, *89*(18), 8671–8675. https://doi.org/10.1073/pnas.89.18.8671

Kamogashira, T., Hayashi, K., Fujimoto, C., Iwasaki, S., Yamasoba, T. (2017). Functionally and morphologically damaged mitochondria observed in auditory cells under senescence-inducing stress. *Npj Aging and Mechanisms of Disease*, *3*(1), 1–11. https://doi.org/10.1038/s41514-017-0002-2

Kusch, J. & Zifarelli, G. (2014). Patch-clamp fluorometry: electrophysiology meets fluorescence. *Biophysical Journal*, *106*(6), 1250–1257. https://doi.org/10.1016/j.bpj.2014.02.006

Liberman, M. C., Gao, J., He, D. Z. Z., Wu, X., Jia, S., Zuo, J. (2002). Prestin is required for electromotility of the outer hair cell and for the cochlear amplifier. *Nature*, *419*(6904), 300–304. https://doi.org/10.1038/nature01059

Liu, X. Z., Ouyang, X. M., Xia, X. J., Zheng, J., Pandya, A., Li, F., Du, L., Welch, K., Petit, C., Smith, R., Webb, B., Yan, D., Arnos, K., Corey, D., Dallos, P., Nance, W., Chen, Z. Y. (2003). Prestin, a cochlear motor protein, is defective in non-syndromic hearing loss. *Human Molecular Genetics*, *12*(10), 1155–1162. https://doi.org/10.1093/hmg/ddg127

Lorito, G., Giordano, P., Prosser, S., Martini, A., Hatzopoulos, S. (2006). Noise-induced hearing loss: a study on the pharmacological protection in the Sprague Dawley rat with N-acetyl-cysteine. *Acta Otorhinolaryngologica Italica : Organo Ufficiale Della Società Italiana Di Otorinolaringologia e Chirurgia Cervico-Facciale*, *26*(3), 133–139.

Loukzadeh, Z., Hakimi, A., Esmailidehaj, M., Mehrparvar, A. H. (2015). Effect of Ascorbic Acid on Noise Induced Hearing Loss in Rats. *Iranian Journal of Otorhinolaryngology*, *27*(81), 267–272.

Lu, F., Li, S., Jiang, Y., Jiang, J., Fan, H., Lu, G., Deng, D., Dang, S., Zhang, X., Wang, J., Yan, N. (2011). Structure and mechanism of the uracil transporter UraA. *Nature*, *472*(7342), 243–246. https://doi.org/10.1038/nature09885

Ludwig, J., Oliver, D., Frank, G., Klocker, N., Gummer, A. W., Fakler, B. (2002). Reciprocal electromechanical properties of rat prestin: The motor molecule from rat outer hair cells. *Proceedings of the National Academy of Sciences*, *98*(7), 4178–4183. https://doi.org/10.1073/pnas.071613498

Mitchell, P. (1990). Osmochemistry of solute translocation. *Research in Microbiology*, *141*(3), 286–289. https://doi.org/10.1016/0923-2508(90)90002-8

Mitchell, P. (1957). A general theory of membrane transport from studies of bacteria. *Nature*, *180*(4577), 134–136. https://doi.org/10.1038/180134a0

Mount, D. B. & Romero, M. F. (2004). The SLC26 gene family of multifunctional anion exchangers. *Pflugers Archiv : European Journal of Physiology*, *447*(5), 710–721. https://doi.org/10.1007/s00424-003-1090-3

Nicolson, T. (2005). The Genetics of Hearing and Balance in Zebrafish. *Annual Review of Genetics*, *39*(1), 9–22. https://doi.org/10.1146/annurev.genet.39.073003.105049

Ohashi, K., Fujiwara, S., Mizuno, K. (2017). Roles of the cytoskeleton, cell adhesion and rho signalling in mechanosensing and mechanotransduction. *The Journal of Biochemistry*, *161*(3), 245–254. https://doi.org/10.1093/jb/mvw082

Oliver, D. & Fakler, B. (1999). Expression density and functional characteristics of the outer hair cell motor protein are regulated during postnatal development in rat. *The Journal of Physiology*, *519*(3), 791–800. https://doi.org/10.1111/j.1469-7793.1999.0791n.x

Oliver, D., He, D. Z. Z., Klöcker, N., Ludwig, J. (2001). Intracellular Anions as the Voltage Sensor of Prestin , the Outer Hair Cell Motor Protein. *Science*, *2340*(2001), 2340–2344. https://doi.org/10.1126/science.1060939

Olson, E. S., Duifhuis, H., Steele, C. R. (2012). Von Békésy and cochlear mechanics. *Hearing Research*, *293*(1–2), 31–43. https://doi.org/10.1016/j.heares.2012.04.017

Popper, A. N. & Fay, R. R. (1993). Sound detection and processing by fish: critical review and major research questions. *Brain, Behavior and Evolution*, *41*(1), 14–38. https://doi.org/10.1159/000113821

Rajagopalan, L., Patel, N., Madabushi, S., Goddard, J. A., Anjan, V., Lin, F., Shope, C., Farrell, B., Lichtarge, O., Davidson, A., Brownell, W., Pereira, F. A. (2006). Essential Helix Interactions in the Anion Transporter Domain of Prestin Revealed by Evolutionary Trace Analysis. *Journal of Neuroscience*, *26*(49), 12727–12734. https://doi.org/10.1523/jneurosci.2734-06.2006

Rajagopalan, L., Greeson, J. N., Xia, A., Liu, H., Sturm, A., Raphael, R. M., Davidson, A., Oghalia, J., Pereira, F., Brownell, W. E. (2007). Tuning of the outer hair cell motor by membrane cholesterol. *Journal of Biological Chemistry*, *282*(50), 36659–36670. https://doi.org/10.1074/jbc.M705078200

Rajagopalan, L., Organ-Darling, L. E., Liu, H., Davidson, A. L., Raphael, R. M., Brownell, W. E., Pereira, F. A. (2010). Glycosylation regulates prestin cellular activity. *JARO - Journal of the Association for Research in Otolaryngology*, *11*(1), 39–51. https://doi.org/10.1007/s10162-009-0196-5

Uzhachenko, R., Boyd, K., Olivares-Villagomez, D., Zhu, Y., Shawn, J., Goodwin, J. S., Rana, T., Shanker, A., Tan, W. J. T., Bondar, T., Medzhitov, R., Ivanova, A. V. (2017). Mitochondrial protein Fus1/Tusc2 in premature aging and age-related pathologies: critical roles of calcium and energy homeostasis. *Aging*, *9*(3), 627–649. https://doi.org/10.18632/aging.101213

Reithmeier, R. A. F., Casey, J. R., Kalli, A. C., Sansom, M. S. P., Alguel, Y., Iwata, S. (2016). Band 3, the human red cell chloride/bicarbonate anion exchanger (AE1, SLC4A1), in a structural context. *Biochimica et Biophysica Acta - Biomembranes*, *1858*(7), 1507–1532. https://doi.org/10.1016/j.bbamem.2016.03.030

Rhode, W. S. (2007). Basilar membrane mechanics in the 6–9kHz region of sensitive chinchilla cochleae. *The Journal of the Acoustical Society of America*, *121*(5), 2792–2804. https://doi.org/10.1121/1.2718397

Riley, B. B., Zhu, C., Janetopoulos, C., Aufderheide, K. J. (1997). A critical period of ear development controlled by distinct populations of ciliated cells in the zebrafish. *Developmental Biology*, *191*(2), 191–201. https://doi.org/10.1006/dbio.1997.8736

Robles, L. & Ruggero, M. A. (2001). Mechanics of the mammalian cochlea. *Physiological Reviews*, *81*(3), 1305–1352. https://doi.org/10.1152/physrev.2001.81.3.1305

Rybalchenko, V. & Santos-Sacchi, J. (2003). Cl- flux through a non-selective, stretch-sensitive conductance influences the outer hair cell motor of the guinea-pig. *The Journal of Physiology*, *547*(Pt 3), 873–891. https://doi.org/10.1113/jphysiol.2002.036434

Rybalchenko, V. & Santos-Sacchi, J. (2008). Anion control of voltage sensing by the motor protein prestin in outer hair cells. *Biophysical Journal*, *95*(9), 4439–4447. https://doi.org/10.1529/biophysj.108.134197

Sakmann, B. & Neher, E. (1976). Single-channel currents recorded from membrane of denervated frog muscle fibres. *Nature*, *260*(5554), 799–802. https://doi.org/10.1038/260799a0

Santos-Sacchi, J. (1991). Reversible inhibition of voltage-dependent outer hair cell motility and capacitance. *The Journal of Neuroscience : The Official Journal of the Society for Neuroscience*, *11*(10), 3096–3110. Retrieved from http://www.ncbi.nlm.nih.gov/pubmed/1941076

Santos-Sacchi, J., Shen, W., Zheng, J., Dallos, P. (2001). Effects of membrane potential and tension on prestin, the outer hair cell lateral membrane motor protein. *The Journal of Physiology*, *531*(Pt 3), 661–666. https://doi.org/10.1111/j.1469-7793.2001.0661h.x

Santos-Sacchi, J. & Song, L. (2014a). Chloride-driven electromechanical phase lags at acoustic frequencies are generated by SLC26a5, the outer hair cell motor protein. *Biophysical Journal*, *107*(1), 126–133. https://doi.org/10.1016/j.bpj.2014.05.018

Santos-Sacchi, J. & Song, L. (2014b). Chloride and salicylate influence prestin-dependent specific membrane capacitance: support for the area motor model. *The Journal of Biological Chemistry*, *289*(15), 10823–10830. https://doi.org/10.1074/jbc.M114.549329

Santos-Sacchi, J. & Song, L. (2016). Chloride Anions Regulate Kinetics but Not Voltage-Sensor Qmax of the Solute Carrier SLC26a5. *Biophysical Journal*, *110*(11), 2551–2561. https://doi.org/10.1016/j.bpj.2016.05.002

Santos-Sacchi, J., Song, L., Zheng, J., Nuttall, A. L. (2006). Control of mammalian cochlear amplification by chloride anions. *The Journal of Neuroscience : The Official Journal of the Society for Neuroscience*, *26*(15), 3992–3998. https://doi.org/10.1523/JNEUROSCI.4548-05.2006

Schaechinger, T. J., Gorbunov, D., Halaszovich, C. R., Moser, T., Kügler, S., Fakler, B., Oliver, D. (2011). A synthetic prestin reveals protein domains and molecular operation of outer hair cell piezoelectricity. *EMBO Journal*, *30*(14), 2793–2804. https://doi.org/10.1038/emboj.2011.202

Schaechinger, T. J. & Oliver, D. (2007a). Nonmammalian orthologs of prestin (SLC26A5) are electrogenic divalent/chloride anion exchangers. *Proceedings of the National Academy of Sciences of the United States of America*, *104*(18), 7693–7698. https://doi.org/10.1073/pnas.0608583104

Schlessinger, A., Matsson, P., Shima, J. E., Pieper, U., Yee, S. W., Kelly, L., Apeltsin, L., Stroud, R., Ferrin, T., Giacomini, K., Sali, A. (2010). Comparison of human solute carriers. *Protein Science : A Publication of the Protein Society*, *19*(3), 412–428. https://doi.org/10.1002/pro.320

Silverthorn, D. U. (2009). *Physiologie* (4. aktuali). Pearson Education.

Sturm, A. K., Rajagopalan, L., Yoo, D., Brownell, W. E., Pereira, F. A. (2007). Functional expression and microdomain localization of prestin in cultured cells. *Otolaryngology--Head and Neck Surgery : Official Journal of American Academy of Otolaryngology-Head and Neck Surgery*, *136*(3), 434–439. https://doi.org/10.1016/j.otohns.2006.10.030

Tan, X., Pecka, J. L., Tang, J., Okoruwa, O. E., Zhang, Q., Beisel, K. W., He, D. Z. Z. (2011). From Zebrafish to Mammal: Functional Evolution of Prestin, the Motor Protein of Cochlear Outer Hair Cells. *Journal of Neurophysiology*, *105*(1), 36–44. https://doi.org/10.1152/jn.00234.2010

Thurtle-Schmidt, B. H. & Stroud, R. M. (2016). Structure of Bor1 supports an elevator transport mechanism for SLC4 anion exchangers. *Proceedings of the National Academy of Sciences*, *113*(38), 10542–10546. https://doi.org/10.1073/pnas.1612603113

van Montfort, R. L. M., Congreve, M., Tisi, D., Carr, R., Jhoti, H. (2003). Oxidation state of the active-site cysteine in protein tyrosine phosphatase 1B. *Nature*, *423*(6941), 773–777. https://doi.org/10.1038/nature01681

Walter, J. D., Sawicka, M., Dutzler, R. (2019). Cryo-EM structures and functional characterization of murine Slc26a9 reveal mechanism of uncoupled chloride transport. *ELife*, *8*, e46986. https://doi.org/10.7554/eLife.46986

Wang, J., Song, Q., Yu, D., Yang, G., Xia, L., Su, K., Shi, H., Wang, J., Yin, S. (2015). Ontogenetic development of the auditory sensory organ in zebrafish (Danio rerio): changes in hearing sensitivity and related morphology. *Scientific Reports*, *5*, 15943. https://doi.org/10.1038/srep15943

Weber, T., Göpfert, M. C., Winter, H., Zimmermann, U., Kohler, H., Meier, A., Hendrich, O., Rohbock, K., Robert, D., Knipper, M. (2003). Expression of prestin-homologous solute carrier (SLC26) in auditory organs of nonmammalian vertebrates and insects. *Proceedings of the National Academy of Sciences*, *100*(13), 7690 LP – 7695. https://doi.org/10.1073/pnas.1330557100

Weiss, S. A., Preuss, T., Faber, D. S. (2009). Phase encoding in the Mauthner system: implications in left-right sound source discrimination. *The Journal of Neuroscience : The Official Journal of the Society for Neuroscience*, *29*(11), 3431–3441. https://doi.org/10.1523/JNEUROSCI.3383-08.2009

Yu, X., Yang, G., Yan, C., Baylon, J. L., Jiang, J., Fan, H., Lu, G., Hasegawa, K., Okumura, H., Wang, T., Tajkhorshid, E., Li, S., Yan, N. (2017). Dimeric structure of the uracil:proton symporter UraA provides mechanistic insights into the SLC4/23/26 transporters. *Cell Research*, *27*(8), 1020–1033. https://doi.org/10.1038/cr.2017.83

Zheng, J., Du, G. G., Anderson, C. T., Keller, J. P., Orem, A., Dallos, P., Cheatham, M. A. (2006). Analysis of the oligomeric structure of the motor protein prestin. *Journal of Biological Chemistry*, *281*(29), 19916–19924. https://doi.org/10.1074/jbc.M513854200

Zheng, J., Shen, W., He, D. Z. Z., Long, K. B., Madison, L. D., Dallos, P. (2000a). Prestin is the motor protein of cochlear outer hair cells. *Nature*, *405*(6783), 149–155. https://doi.org/10.1038/35012009

Zhu, Y., Chun, L., Zong, L., Chen, G.-D., Zhao, H.-B. (2013). Active cochlear amplification is dependent on supporting cell gap junctions. *Nature Communications*, *4*, 1–18. https://doi.org/10.1038/ncomms2806.Active

7 Supplements

7.1 Protein sequences

All prestin constructs were cloned in the standard vector pEGFP-N1 that has a gene for kanamycin resistance for selection. Furthermore, it has the gene for enhanced GFP, which allows for expression control of prestin and traceability of its localisation.

7.1.1 Sequences of rat prestin

Below the protein sequence of rat prestin wild type is listed. The DNA sequence consists of 2.235 base pairs and the transcribed protein has 745 amino acids. In the protein sequence the cysteines, which were mutated to alanines for the SCAM experiments, were marked in red. All nine cysteines could be mutated without loss of functionality. Thirteen amino acids within transmembrane domain 3 were investigated for their accessibility. These amino acids are additionally highlighted in yellow.

>rat prestin wild type: protein sequence (>NP_110467.1)

```
MDHAEENEIPAETQKYLVERPIFSHPVLQERLHVKDKVTDSIGDKLKQAF 50
TCTPKKVRNIIYMFLPITKWLPAYKFKEYVLGDLVSGISTGVLQLPQGLA 100
FAMLAAVPPVFGLYSSFYPVIMYCFFGTSRHISIGPFAVISLMIGGVAVR 150
LVPDDIVIPGGVNATNGTEARDALRVKVAMSVTLLSGIIQFCLGVCRFGF 200
VAIYLTEPLVRGFTTAAAVHVFTSMLKYLFGVKTKRYSGIFSVVYSTVAV 250
LQNVKNLNVCSLGVGLMVFGLLLGGKEFNERFKEKLPAPIPLEFFAVVMG 300
TGISAGFNLHESYSVDVVGTLPLGLLPPANPDTSLFHLVYVDAIAIAIVG 350
FSVTISMAKTLANKHGYQVDGNQELIALGICNSIGSLFQTFSISCSLSRS 400
LVQEGTGGKTQLAGCLASLMILLVILATGFLFESLPQAVLSAIVIVNLKG 450
MFMQFSDLPFFWRTSKIELTIWLTTFVSSLFLGLDYGLITAVIIALLTVI 500
YRTQSPSYTVLGQLPDTDVYIDIDAYEEVKEIPGIKIFQINAPIYYANSD 550
LYSSALKRKTGVNPAIIMGARRKAMRKYAKEVGNANIANATVVKVDAEVD 600
GENATKPEEEDDEVKFPPIVIKTTFPEELQRFLPQGENIHTVILDFTQVN 650
FMDSVGVKTLAGIVKEYGDVGIYVYLAGCSAQVVNDLTSNRFFENPALKE 700
LLFHSIHDAVLGSQVREAMAEQETTVLPPQEDMEPNATPTTPEAT
```

Total length= 745 amino acids

7.1.2 Sequences of zebrafish prestin

The following sequence is the protein sequence of zebrafish prestin wild type. The DNA sequence has a length of 2.217 base pairs and the protein consists of 739 amino acids. There are seven native cysteines in zebrafish prestin wild type. The first six cysteines (marked in red) were mutated to alanines for the SCAM experiments. However, the mutation of C726A leads to a dysfunctional protein. Therefore, the experiments were performed in a nearly cysteine-free basic construct. The cysteine at position 726 (marked in blue) is located within the STAS domain of prestin and consequently far away from the investigated transmembrane sections. Furthermore, the basic construct ("nearly cysteine-free") of the SCAM study was functional and produced wild type-like transport currents. Additionally, this construct was insensitive to MTS reagents despite the remaining cysteine. The investigated positions within transmembrane domain 3 are highlighted in yellow and the positions within transmembrane domain 10 are highlighted in green.

>zebrafish prestin wild type: protein sequence (>NP_958881.1)

```
MEHVTVSEEPSATLMYHVERPIFSEAYIDSELLHKRKKTPKPYKLRVAEH 50
LCCSSEKVKSVVFGFLPILTWLPSYPLKEYLFGDIVSGISTGVMQLPQGL 100
AYAMLAAVPPVFGLYSSFYPVLLYTFFGTSKHISIGTFAVISLMIGGVAV 150
REAPDSMFMVNGTNSSLVVNIEARDSRRVEVVVALTTLVGIIQFVLGLLR 200
FGFLAIYLTEPLVRGFTTAAAVHVSVSQLKYLLGVKTARFNGPLSVVYSL 250
DAVLRNIADTNIVTLIIGLGCTVFLYIIKQLNERFKKKLLIPIPGEIIVV 300
IVSTGISYGMLMSENYGVDVVGKIPTGLLPPKVPDFSVFPNLFADAVPIA 350
VVGFSITISLAKTFALKYGYSVDGNQELIALGLCNFVSSFFHTFVVTASM 400
SRSLVQESTGGHTEIAGLLASLLVLLVVVAIGFVFQPLPTTVLAAIIMVN 450
LLGMFKQTRDIPVLWRKSKIELAIWLVSFFASVLLGLDYGLAVAMAFAIL 500
TVIYKTQRPKNVVLGQIPDTGLYFDVDEYEEAEECSGIKIFQSNSSIYFA 550
NSELYVKALKAKTGIDPEKLLDAKKLQLKYAKRDTEGTKTVNQGSLLKKN 600
AVVLLDMELGVTHEVLNGPQKPKHVHTNGQMTEKHIESESEDEFFLQRLT 650
PIHSVILDFTPVNFIDSVGAKTIKSVIKEYATVDVKVVLAGCSRTLLSEL 700
RTLQFFSEPVTPDLIFPTIHDAVLQCKRWRDLPVHPNIH
```

Total length= 739 amino acids

7.2 Supplemental figures: SCAM

The following figures show representative NLC traces of the mutants which were insensitive to applied MTS reagents. Supplemental figure 7.1 shows the insensitive mutants of transmembrane domain 3 in rat prestin.

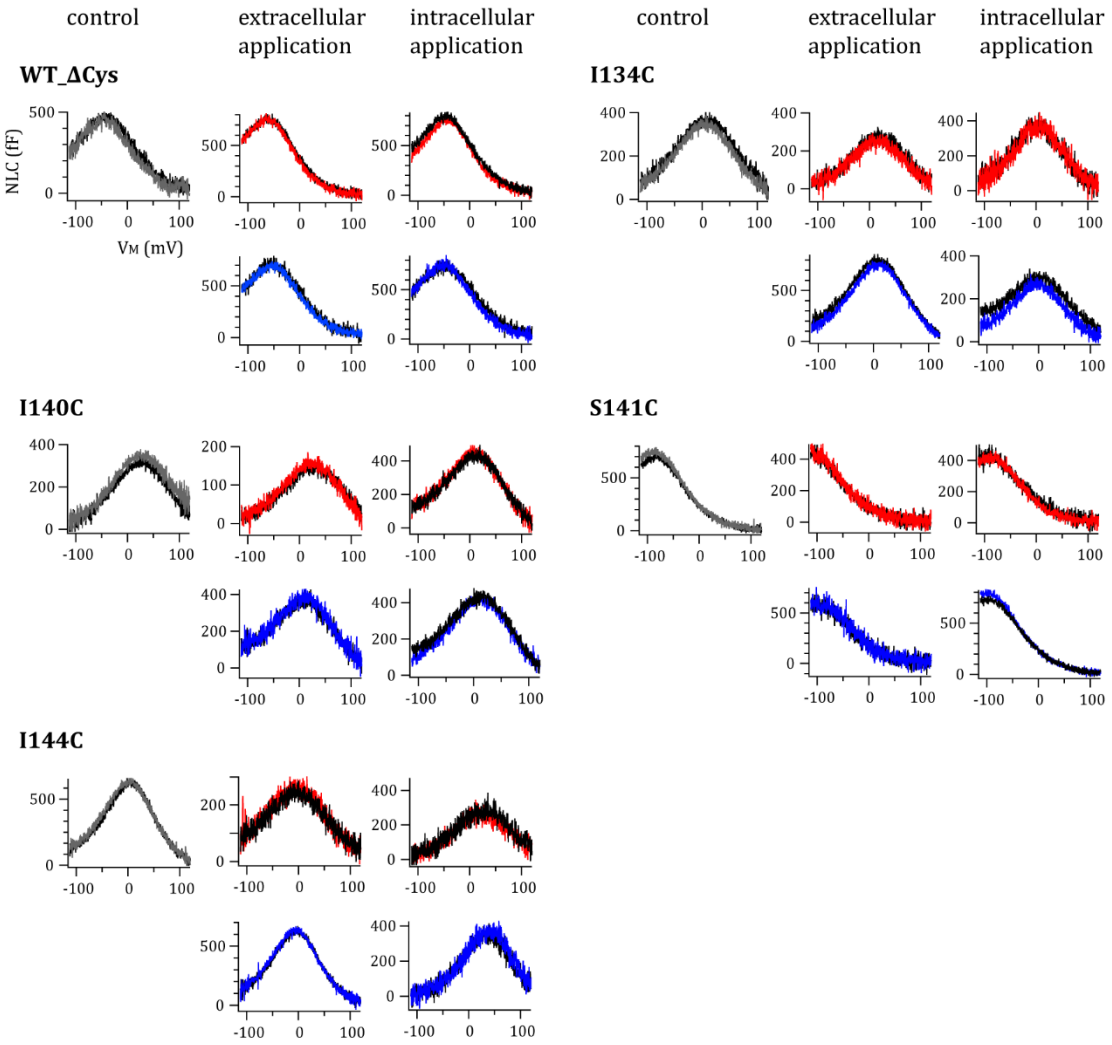

Supplemental figure 7.1: The effects of applied MTS reagents on the NLC of the rat prestin constructs with mutations within TM 3. WT_△Cys is the basic construct with all cysteines mutated to alanines (cf. 2.4). Each mutant is represented by five graphs with two representative traces of each condition. All traces show the NLC of a representative measurement. Black traces are the initial traces before MTS was applied and the potential effect would be distinct. Grey traces are traces from the control measurements without MTS application, red traces are from a measurement with applied MTSES and blue traces from a measurement with applied MTSET. These traces (grey, red and blue) were taken from a timepoint towards the end of the measurement.

Representative transport currents of the mutants of transmembrane domain 3 and 10 in zebrafish prestin, which are insensitive to MTS compounds, are depicted in the Supplemental figure 7.2 and the Supplemental figure 7.3.

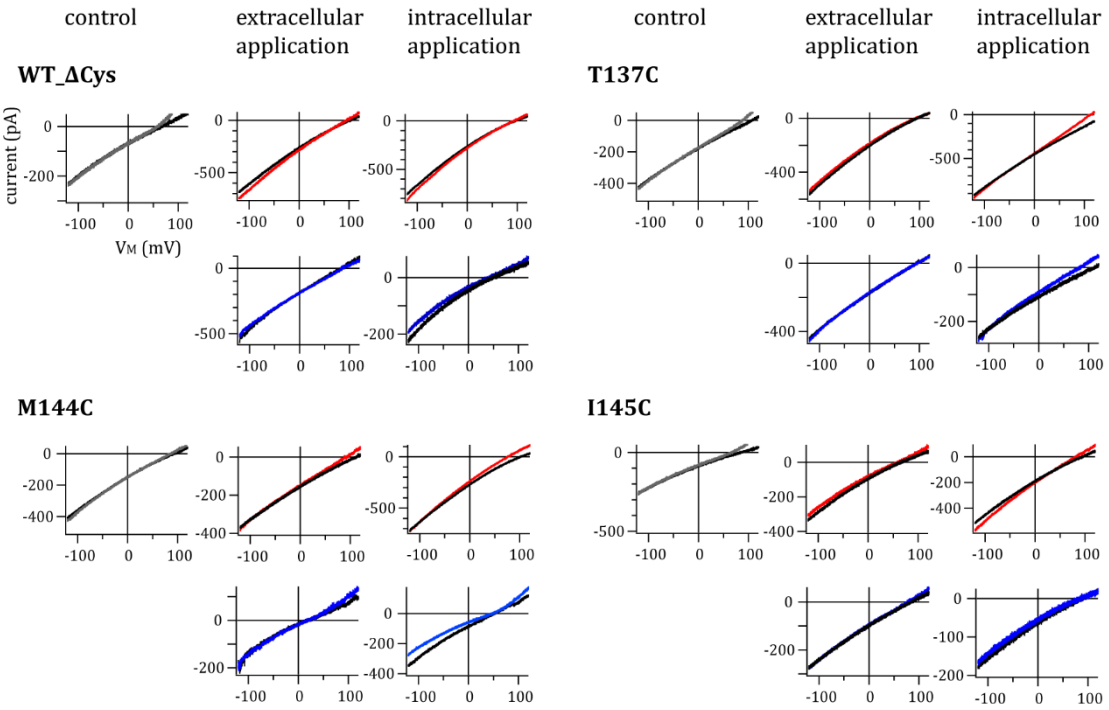

Supplemental figure 7.2: The effects of applied MTS reagents on the transport currents of the zebrafish prestin constructs with mutations within TM 3. WT_△Cys is the basic construct with nearly all cysteines mutated to alanines (cf. 2.4). Each mutant is represented by five graphs with two representative traces of each condition. All traces show transport currents of a representative measurement. Black traces are the initial traces before MTS was applied and the potential effect would be distinct. Grey traces are traces from the control measurements without MTS application, red traces are from a measurement with applied MTSES and blue traces from a measurement with applied MTSET. These traces (grey, red and blue) were taken from a timepoint towards the end of the measurement.

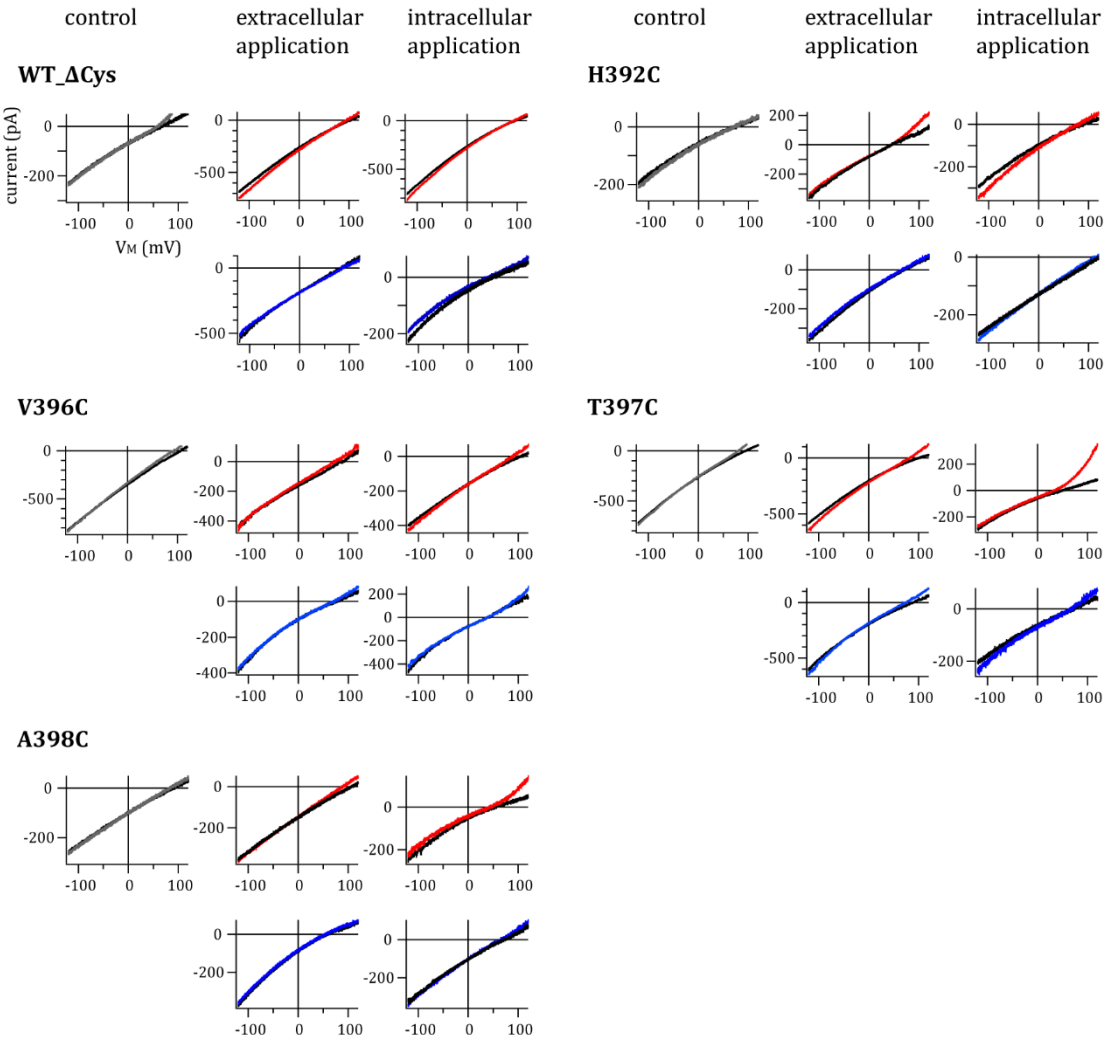

Supplemental figure 7.3: The effects of applied MTS reagents on the transport currents of the zebrafish prestin constructs with mutations within TM 10. WT_△Cys is the basic construct with nearly all cysteines mutated to alanines (cf. 2.4). Each mutant is represented by five graphs with two representative traces of each condition. All traces show transport currents of a representative measurement. Black traces are the initial traces before MTS was applied and the potential effect would be distinct. Grey traces are traces from the control measurements without MTS application, red traces are from a measurement with applied MTSES and blue traces from a measurement with applied MTSET. These traces (grey, red and blue) were taken from a timepoint towards the end of the measurement.

7.3 Supplemental figures: Competitive inhibitors

Supplemental figure 7.4 shows the measurements with the two different blockers that were performed by Florian Nies. The measurements compared the blocking abilities of membrane-permeable salicylate (10 mM) and membrane-impermeable phenolsulphonic acid (PSA; 30 mM). Transport currents of the wild type of chicken prestin decreased upon extracellular application of salicylate (28.9 ± 10.3 %) as well as of PSA (43.3 ± 11.3 %). In contrast, the NLC peak amplitude of rat prestin wild type was only blocked by salicylate (43.0 ± 1.4 %) but not by PSA (100.9 ± 5.3 %).

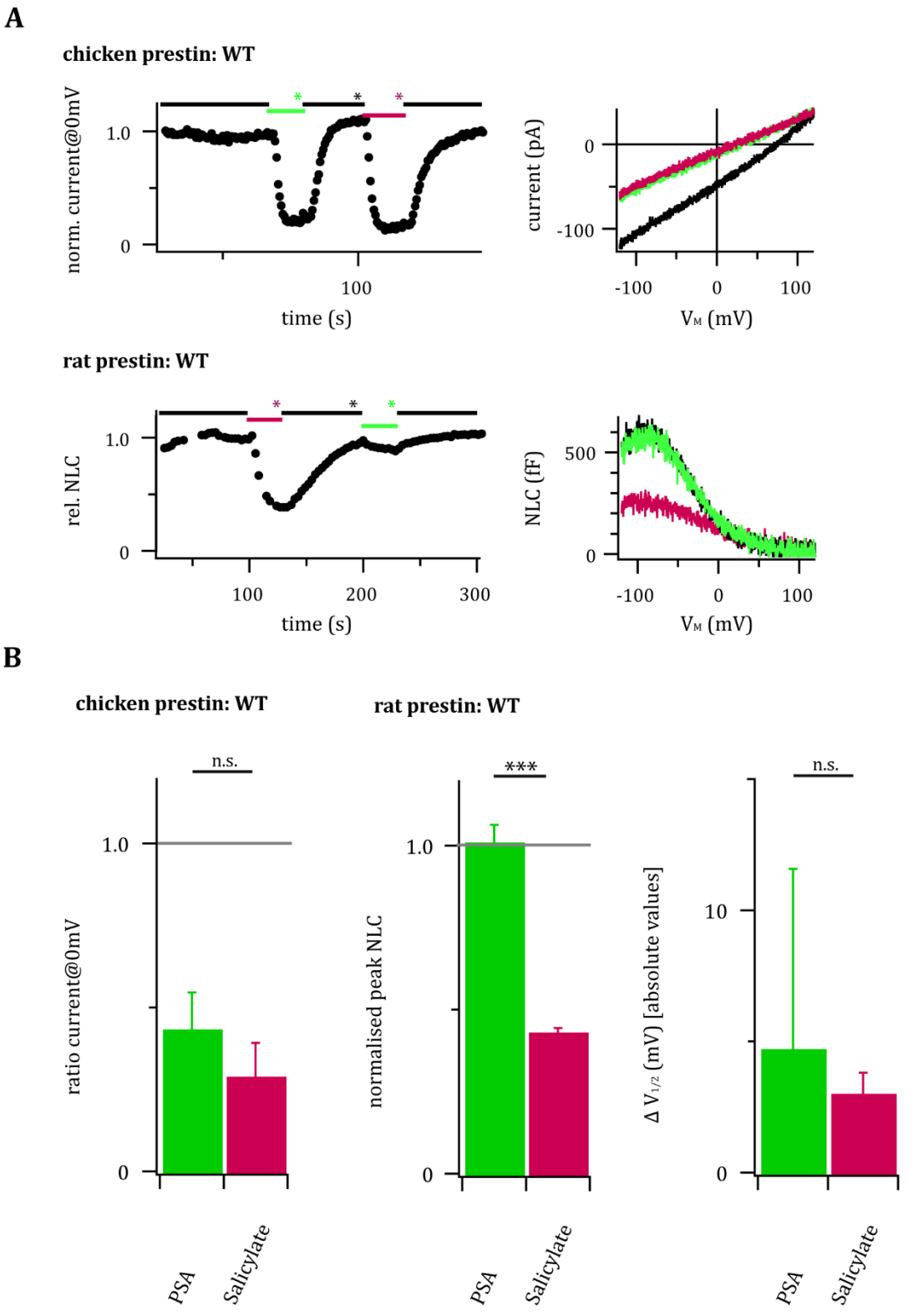

Supplemental figure 7.4: Comparison of the effect of the two NLC blockers phenolsulphonic acid (PSA) and salicylate on chicken and rat prestin. Black bars and traces: with fluid-flow; green bars and traces: extracellularly applied PSA (30 mM); purple bars and traces: extracellularly applied salicylate (10 mM). **A:** The upper graph shows a representative measurement of chicken prestin wild type (WT), the lower graph of rat prestin wild type (WT). The left graphs were normalised traces of the transport current and the NLC, respectively. The right graphs show corresponding representative traces. Asterisks mark the position of the corresponding traces. **B:** The bar diagrams show the effects on the transport current, the NLC peak amplitude and the $V_{1/2}$ upon PSA or salicylate application. Measurements were performed by Florian Nies. n≥3. Mean ± SEM.

vi Curriculum Vitae

vii List of academic teachers

My academic teachers were the following ladies and gentlemen in:

Marburg

Prof. Dr. Dominik Oliver

Dr. Dmitry Gorbunov

Mainz

Alt K.W., Baiersdörfer M., Bramanti, B., Böhning-Gaesse, K., Burger J., Claßen-Bockhoff R., Efferth, T., Hankeln T., Kadereit J.W., Kilbinger, A., Koch-Brandt C., Kraemer C., Markl J., Sachsse W., Schmidt E.R., Schuh, H.-J., Seitz, A., Technau G., Unden G., Urban J., Pochodzalla, J., Postina R., Zentel, R., Zischler H.

viii Acknowledgements

I thank Prof. Dr. Dominik Oliver for providing my research topic and giving me the opportunity to work in his group. In addition, I thank him for the given feedback and support.

Furthermore, I want to thank Dr. Dmitry Gorbunov who was my direct supervisor and introduced me to the project. Unfortunately, that was not through my whole PhD time but during that time he was the perfect mentor: whenever I had a problem he helped immediately and he was always polite and patient.

Of course, I would also like to extend my thanks to all the members of the institute that includes the professors, the postdocs, other PhD students, technical staff, our secretary, the members of the mechanical facility as well as all the students who passed through the lab. Particularly, I want to emphasise Tina, Gisela, Olga, Nesli and the mechanical staff who silently work in the background but whose contribution is essential. Last but not least I want to separately thank Kirstin, Franzi and Ray for welcome diversion during our common lunch breaks, our regularly movie and GoT sessions and round of discussions. Furthermore, I would like to sincerely thank Kirstin for scientific discussions and support.

My family was always very sympathetic when I found no time to join family events because I was working, cultured cells over Christmas or was deeply lost in writing my thesis – thanks for your support and understanding. My special thanks go to Duncan who constantly supported me and always found the right words to motivate me again. His unwavering trust in me prevented me several times from just giving up.

This project was supported by the DFG grant spp 1608 (“Ultrafast and temporally precise information processing: normal and dysfunctional hearing”) to Dominik Oliver.

ix Ehrenwörtliche Erklärung